

© 2025

Kai Gao

ALL RIGHTS RESERVED

TABLETOP OBJECT REARRANGEMENT: STRUCTURE, COMPLEXITY, AND
EFFICIENT COMBINATORIAL SEARCH-BASED SOLUTIONS

By

KAI GAO

A dissertation submitted to the

School of Graduate Studies

Rutgers, The State University of New Jersey

In partial fulfillment of the requirements

For the degree of

Doctor of Philosophy

Graduate Program in Computer Science

Written under the direction of

Jingjin Yu

And approved by

New Brunswick, New Jersey

January 2025

ABSTRACT OF THE DISSERTATION

Tabletop Object Rearrangement: Structure, Complexity, and Efficient Combinatorial Search-Based Solutions

by KAI GAO

Dissertation Director: Jingjin Yu

This thesis aims to provide a complete structural analysis and efficient algorithmic solutions to tabletop object rearrangement with overhand grasps (TORO). This problem captures a common task that we solve on a daily basis and is essential in enabling truly intelligent robotic manipulation. When rearranging many objects in a confined workspace, on the one hand, action sequencing with the least pick-n-places in TORO is NP-hard[1]; on the other hand, temporarily relocating objects to some free space (“buffer poses”) may be necessary but highly challenging in a cluttered environment.

Focusing on these two challenges, the thesis covers TORO in four different setups, including varied workspace assumptions (with/without external buffers) and manipulator settings (single/dual-arms or a mobile manipulator).

The thesis first explores TORO with external buffers (TORE), addressing the size of needed space for temporary object relocation (“running buffers”). This study shows that finding the maximum running buffers (MRB) is NP-hard and that MRB can grow unbounded with an increasing number of objects, even with uniform shapes. Exact algorithms developed for both labeled and unlabeled settings can scale to over 100 objects.

The thesis further extends the TORE algorithms to tabletop rearrangement with internal buffers (TORI), where all temporary object placements need to be inside the workspace. A

two-step baseline planner is developed, generating a primitive plan based on object-object collisions and selecting buffer locations. Using a “lazy” planner within a bi-directional tree search framework, the method efficiently produces robust, high-quality solutions in simulations, outperforming existing approaches for large-scale problems.

The thesis later explores lazy buffer verification for dual-arm task planning in non-monotone rearrangement tasks. Handling complex dependencies often requires moving objects multiple times and coordinating hand-offs between two arms in a shared workspace. Our task planning algorithms effectively sequence and distribute pick-and-place tasks, yielding significant time savings over greedy or single-robot approaches. For motion planning, we introduce a tightly integrated pipeline that combines novel sampling methods with advanced trajectory optimization. The proposed planner achieves superior execution times and trajectory compliance with acceleration and jerk constraints, advancing coordination in dual-arm systems.

Finally, the thesis incorporates lazy buffer verification into an A* framework (ORLA*) for time-optimal multi-object rearrangement in mobile robot tabletop setups. The proposed method applies delayed evaluation to optimize object pick-and-place sequences, factoring in both end-effector and robot base movements. With learning-based stability predictions, ORLA* can handle complex, multi-layered rearrangement tasks. Extensive simulations and ablation studies validate ORLA*’s effectiveness, providing high-quality solutions for challenging rearrangement scenarios.

ACKNOWLEDGMENTS

First and foremost, I would like to express my sincere gratitude to my PhD advisor, Prof. Jingjin Yu. JJ's insightful guidance and dedication have been invaluable throughout my PhD journey. He has set an inspiring example of how to approach research and excel as a scientist in robotics, and I am deeply grateful for the trust and freedom he provided to pursue my ideas.

I am also thankful to my co-authors and collaborators, especially Kostas, Baichuan, and Rui, whose insights and guidance have been true milestones in my research journey. Working together has been a deeply rewarding experience, and I greatly appreciate their expertise, constructive feedback, and the depth they brought to our work.

Additionally, I would like to thank my labmates, Siwei, Zihe, Duo, Haonan, Tzvika, and Teng, for the discussions and exchange of ideas. The collaborative environment and support within the lab have enriched my research experience and have been an essential part of my PhD.

To my parents and my girlfriend, who have been a constant source of support and encouragement, thank you for being there through the highs and lows of this journey. Your belief in me has kept me moving forward.

Thank you all for your support. This accomplishment would not have been possible without each of you.

TABLE OF CONTENTS

Abstract	ii
Acknowledgments	iv
List of Tables	xi
List of Figures	xii
List of Acronyms	xx
Chapter 1: Introduction and Background	1
Chapter 2: Running Buffer Minimization (RBM) for TORO with External Buffers (TORE)	6
2.1 Motivation	6
2.2 Related Work	7
2.3 TORO with External Buffer Space (TORE)	9
2.3.1 Labeled TORO with External Buffers	9
2.3.2 Unlabeled TORO with External Buffers	12
2.4 Structural Analysis and NP-Hardness	13
2.4.1 Running Buffer versus Total Buffer	13
2.4.2 Running Buffers and Linear Vertex Ordering	15

2.4.3	Intractability of Computing MRB	17
2.5	Lower and Upper Bounds on MRB	20
2.5.1	Intrinsic MRB Lower Bounds	21
2.5.2	Upper Bounds on MRB for URBM	24
2.6	Algorithms for TORE	26
2.6.1	Dynamic Programming (DP) for LRBM	26
2.6.2	A Priority Queue-Based Method for URBM	29
2.6.3	Depth-First Dynamic Programming	30
2.6.4	Minimizing Total Buffers Subject to MRB Constraints	31
2.7	Experimental Results	33
2.7.1	LRBM over Random Instances	35
2.7.2	URBM over Random Instances	36
2.7.3	Manually Constructed Difficult Cases of TORE	37
2.8	Physical Experiments	39
2.8.1	Hardware Setup	39
2.8.2	Experimental Validation	40
2.9	Summary	41
Chapter 3: TRLB: Tabletop Rearrangement with Lazy Buffer Pose Verification		43
3.1	Motivations	43
3.2	Related Work	44
3.3	Tabletop Rearrangement with Internal Buffer Space (TORI)	45
3.3.1	Problem Statement	45

3.4	Algorithmic Solutions	46
3.4.1	Lazy Buffer Pose Verification	46
3.4.1.1	Primitive Plan	47
3.4.1.2	Buffer Allocation	47
3.4.2	Failure Recovery with Bi-Directional Search	50
3.4.3	Preprocessing for Rearrangement in Confined Workspace	52
3.5	Heterogeneous TORI	52
3.5.1	Motivation	52
3.5.2	Problem Formulation	54
3.5.3	Weighting Heuristics for HeTORI	55
3.5.3.1	Collision Probability (HeCP) for PP	55
3.5.3.2	Task Impedance (HeTI) for TI	57
3.5.4	Extended TRLB (ETRLB) for HeTORI	58
3.5.5	Extended MCTS (EMCTS) for HeTORI	59
3.5.5.1	Reducing action space	59
3.5.5.2	Efficient collision checker for HeTORI	59
3.6	Experimental Results for TORI	60
3.6.1	Ablation Study for Cylindrical Objects	61
3.6.2	Comparison with Alternatives for Cylindrical Objects	64
3.6.3	Cuboid Objects	65
3.6.4	Hardware Demonstration	66
3.7	Experimental Results for HeTORI	67
3.7.1	Numerical Results in Simulation	67

3.7.2	Demonstrations in Simulation and Real-World	71
3.8	Summary	73
Chapter 4: TRLB for Dual Arm Coordination		75
4.1	Motivation	75
4.2	Related Work	76
4.3	Cooperative Dual-Arm Rearrangement (CDR)	78
4.3.1	Problem Statement	78
4.4	Task Scheduling for CDR	80
4.4.1	Arrangement Space Heuristic Search for CDR in MC Makespan (MCHS)	81
4.5	Buffer Allocation	85
4.6	GPU based Task and Motion Planning in High Dimensional C-Space	86
4.6.1	MCHS Task Planning	86
4.6.2	Motion Planning Phase	87
4.6.3	Enhancing Inverse Kinematic (IK) Solutions	88
4.6.4	Improving Path Planning to Avoid Detours	89
4.6.5	Strategies to Resolve Dual-Arm Trajectory Conflicts	89
4.6.5.1	Dual-arm goal sampling	90
4.6.5.2	Priority based planning	90
4.6.6	Real2Sim2Real	92
4.6.7	Real Robot Control	93
4.7	Experimental Results	93
4.7.1	Task Planning Evaluation	93

4.7.2	Motion Planning Evaluation	98
4.7.3	Sim2Real Gap: Trajectory Tracking Accuracy	99
4.7.4	Performance on Rearrangement Plans Execution	100
Chapter 5: Distance-Optimal TRLB: Object Rearrangement with Lazy A* . . .		105
5.1	Motivation	105
5.2	Related Work	106
5.3	Mobile Robot Tabletop Rearrangement	107
5.4	ORLA*: A* with Lazy Buffer Allocation	108
5.4.1	Deterministic and Nondeterministic States	109
5.4.2	Cost Estimation	110
5.4.3	Buffer Allocation	112
5.4.3.1	Feasibility of a Buffer Pose	113
5.4.3.2	Optimality of a Buffer Pose	113
5.4.3.3	Buffer Sampling	114
5.4.4	Optimality of ORLA*	115
5.5	Evaluation	116
5.5.1	Disc Rearrangement in Simulation	117
5.5.2	Qualitative Analysis of StabilNet	120
5.5.3	General-Shaped Object Rearrangement in Simulation	121
5.6	Summary	122
Chapter 6: Conclusions		123

Appendices 124

 Appendix A: Structural Properties and Proofs for TORE 125

 Appendix B: Interval State Space Heuristic Search for CDR in FC Makespan
 (FCHS) 132

Acknowledgment of Previous Publications 136

References 137

LIST OF TABLES

2.1	$T[S].MRB$ for different last objects ($[p] = [parent]$)	28
2.2	Evaluated methods for TORE.	35
2.3	Comparison between RBM plans and TBM plans in execution time and the number of actions.	41

LIST OF FIGURES

1.1	A TORO instance where the three soda cans are to be rearranged from the left configuration to the right configuration.	1
1.2	[Left] PyBullet setup for the Cooperative Multi-Robot Rearrangement problem, where only a portion of the environment (the region between two white lines) is reachable by both arms. [Right] Handoff operation at a pre-computed pose above the environment.	4
1.3	An example of the Mobile Robot Tabletop Rearrangement (MoTaR) setup.	5
2.1	A 7-object labeled instance with uniform cylinders; we will use this instance as a running example. (a) The unshaded discs (as projections of cylinders) represent the start arrangement \mathcal{A}_s and the shaded discs represent the goal arrangement \mathcal{A}_g . (b) The corresponding labeled dependency graph. (c) The corresponding unlabeled dependency graph, which is bipartite and planar.	10
2.2	Two configurations of the setup given in Figure 1.1 and the corresponding dependency graphs.	12
2.3	An instance with the labeled dependency graph formed by 3 copies of 2-cycles. The MFVS is 3. On the other hand, the MRB is just 1 for the problem. The example scales to have arbitrarily large MFVS with MRB remaining at 1.	15
2.4	An LRBM instance with uniform thin cuboids (left) and its labeled dependency graph, where the total number of buffers needed is more than the size of the MFVS when the number of running buffers is minimized.	16
2.5	Two linear orderings of vertices of the labeled dependency graph from Figure 2.1(b) (i.e., these are different representations of the same graph). The right one minimizes MRB.	17

2.6	(a) An undirected graph and a linear ordering of its vertices. (b) A corresponding labeled dependency graph with the same vertex ordering.	18
2.7	(a) An undirected planar graph with five vertices (b) “Object gadgets” for two of the vertices. (c) The corresponding TORE instance.	20
2.8	An instance with 6 cuboids where horizontal and vertical sets represent start and goal poses, respectively. An arbitrary labeling of the objects may be given in the labeled setting.	21
2.9	A URBM instance (left) and its unlabeled dependency graph (right), a 4×3 dependency grid. Unshaded (resp., shaded) discs/vertices indicate start poses (resp., goal poses).	22
2.10	An example of a 9-object LRBM yielding $\Omega(\sqrt{n})$ MRB (left) and the corresponding dependency graph (right).	23
2.11	The recursive solver SEPPLAN for URBM. (a) A $O(\sqrt{ V })$ vertex separator for the planar dependency graph. (b) By removing the start vertices in C and the neighbors of the goal vertices in C , the remaining graph consists of two independent subgraphs and isolated goal poses in C . (c) The problem can be solved by recursively calling SEPPLAN.	25
2.12	Generating dense instances using a physics-engine-based simulator through compression of the left scene to the right scene.	34
2.13	Unlabeled arrangements with $\rho = 0.2, 0.4, 0.6$ respectively.	34
2.14	Performance of DFDP and DP over LRBM. The top row shows the average computation time (s) and the bottom row the success rate, for density levels $\rho = 0.2, 0.3, 0.4$, from left to right. The x -axis denotes the number of objects involved in a test case.	35
2.15	For LRBM instances with $\rho = 0.2-0.4$ and $n = 20-100$, the left figure shows average MRB size and range. The right figure shows the size of the largest connected component of the dependency graph.	36
2.16	(a) Comparison between size of MRB and MFVS. (b) Computation time comparison between TB_{FVS} and TB_{MRB}	37
2.17	Performance of DFDP and PQS over URBM. The top row shows the average computation time and the bottom row shows the success rate, for density levels $\rho = 0.4, 0.5, 0.6$, from left to right.	38

2.18	Average MRB size for URBM instances with $\rho = 0.4 - 0.6$ and $n = 20 - 100$. For $\rho = 0.4$ and 0.5 , the MRB sizes are near zero as the number of objects goes beyond 20.	38
2.19	For handcrafted cases and different numbers of objects, the left figure shows the computation time by DFDP and the right figure the resulting MRB size.	39
2.20	Our hardware setup for executing rearrangement plans computed by proposed algorithms.	40
2.21	An example instance of our experiment. The right side of the pad works as an external space for buffer placements.	41
3.1	A robot arm rearranges word patterns with overhand grasps, minimizing the number of pick-n-place actions. The letters cannot go out of the bounding box and cannot overlap on the tabletop.	46
3.2	A working example with three objects defined in (a). The primitive plan is $[(o_1, s \rightarrow b), (o_3, s \rightarrow b), (o_2, s \rightarrow g), (o_1, b \rightarrow g), (o_3, b \rightarrow g)]$. Figures (b)-(f) show the steps of Alg. 1 after each action. The transparent discs with dashed line boundaries (B_i) represent the buffers satisfying constraints up to each step. For each object o_i , the green (O_i) and cyan (G_i) discs represent the current and goal poses respectively.	50
3.3	A four-object example of preprocessing. The green and cyan discs represent current and goal arrangements respectively. Before preprocessing (left), two buffers need to be allocated synchronously. After preprocessing (right), the problem becomes monotone.	52
3.4	[Left] Our hardware setup for evaluating tabletop rearrangement of multiple heterogeneous objects. One of the test cases is also shown. [Right] The illustration of an example instance where many objects of drastically different sizes and weights are to be rearrangements.	53
3.5	An illustration of the Minkowski difference $P \ominus D(0, 0)$ (red dashed region) of a rectangle P and a disc D	56
3.6	[left] 10 cylinders with $\rho = 0.5$, [right] 10 cuboids with $\rho = 0.4$	60
3.7	Comparison of primitive planners with 10-40 cylinders and density levels $\rho = 0.3$ (top), 0.5 (bottom) (left: computation time in seconds; middle: success rate; right: number of actions as multiples of $ \mathcal{O} $).	62

3.8	Comparison of buffer allocation methods with 10-40 cylinders at density levels $\rho = 0.3$ (top), 0.5 (bottom) (left: computation time in seconds; middle: success rate; right: number of actions as multiples of $ \mathcal{O} $).	62
3.9	Comparison among high-level frameworks and OS with preprocessing. There are 10-40 cylinders in the workspace at density levels $\rho = 0.3$ (top), 0.5 (bottom) (left: computation time in seconds; middle: success rate; right: number of actions as multiples of $ \mathcal{O} $).	63
3.10	Comparison between ST and BST frameworks with “dense-small” instances where 5-8 cylinders packed in the environment and density level $\rho = 0.5$. [left] An example with 5 cylinders, [right] success rate of methods.	64
3.11	Comparison of algorithms with 20-100 cylinders at density level $\rho = 0.3$ (left: computation time in seconds; middle: number of collision checks; right: number of actions as multiples of $ \mathcal{O} $).	65
3.12	Comparison of methods on “dense-small” instances where 5-8 objects are packed in an environment with $\rho = 0.5$ (left: computation time in seconds; middle: number of collisions; right: success rate).	65
3.13	Comparison among methods in lattice instances with 3-35 objects. [left] lattice example; [right] success rate	66
3.14	Comparison between methods in cuboid instances with 10-30 cuboids and $\rho = 0.3$ (left: computation time in seconds; middle: success rate; right: number of actions as multiples of $ \mathcal{O} $).	66
3.15	Experimental settings in addition to that of Figure 3.1.	66
3.16	Illustrations of some simulation test cases at different densities. [top] RAND instances under different density levels. [bottom] SQ instances under different density levels.	68
3.17	Algorithm performance in RAND instances with $\rho = 0.4$ and 20-40 objects. [Left] Plan length as multiplies of $ \mathcal{O} $. [Middle] Computation time (secs). [Right] Success rate.	69
3.18	Algorithm performance in SQ instances with $\rho = 0.4$ and 20-40 objects. [Left] Plan length as multiplies of $ \mathcal{O} $. [Middle] Computation time (secs). [Right] Success rate.	69
3.19	Algorithm performance in RAND instances under different density levels and $ \mathcal{O} = 20$. [Left] Plan length as multiplies of $ \mathcal{O} $. [Middle] Computation time (secs). [Right] Success rate.	70

3.20	Algorithm performance in SQ instances under different density levels and $ \mathcal{O} = 20$. [Left] Plan length as multiplies of $ \mathcal{O} $. [Middle] Computation time (secs). [Right] Success rate.	71
3.21	Algorithm performance in RAND instances with TI objective. $\rho = 0.3$, $20 \leq \mathcal{O} \leq 40$. [Left] Total task impedance. [Middle] Computation time (secs). [Right] Success rate.	72
3.22	Algorithm performance in SQ instances with TI objective. $\rho = 0.3$, $20 \leq \mathcal{O} \leq 40$. [Left] Total task impedance. [Middle] Computation time (secs). [Right] Success rate.	72
3.23	Physical experiment/demo setups. [left] Dense SQ instance with 10 square wooden planks. [middle] Rearranging densely-packed thick wooden blocks of different shapes and sizes. [right] Rearranging 3d-printed Tetris pieces into a heart shape.	73
4.1	[Left] A working example of CDR instance with $\rho = 0.3$. For each object o_i , the start and goal poses are represented by green disc O_i and orange disc G_i respectively. [Right] A CDRF instance and its corresponding dependency graph.	78
4.2	Decision process of generating possible primitive actions. [Upper] The decision process for r_1 to manipulate $o \in \mathcal{O}$ without cooperation with the other arm. That for r_2 is equivalent. [Middle] The decision process for r_1 to manipulate an object $o \in \mathcal{O}$ when only one object o' is blocking the goal pose of o . That for r_2 is equivalent. [Bottom] The decision process when an object $o \in \mathcal{O}$ needs handoff.	82
4.3	[Left] A path on the arrangement state space for the instance in Figure 4.1[Left] under MC metric. [Right] The corresponding schedule of the example instance in Figure 4.1[Left].	83
4.4	[Top] A CDR instance that needs a buffer. [Bottom] An rearrangement plan for the example.	85
4.5	[left] A configuration of our dual-arm setup, also showing that the camera is mounted at the side to detect objects' poses. [right] The corresponding Dual-Arm setup in pyBullet simulation.	93
4.6	A 20-cylinder example of rearrangement instance with $D = 0.4$ and $\rho = 0.5$, moving object from a randomly sampled start arrangement [Left], to an organized goal arrangement [Right].	94

4.7	Performance of FCHS and MCHS in instances with $\rho = 0.5$, $D = 0.3$. The x-axis represents the number of objects.	95
4.8	Algorithm comparison in environments with different density levels D . The x-axis represents the number of objects.	96
4.9	Evaluation of instances with different ρ . The x-axis represents the number of objects.	97
4.10	An instance of CDR with full overlap (CDRF), where each arm can reach every corner of the workspace but its manipulation is likely to be blocked by the other arm.	98
4.11	Algorithm performance in CDR instances with $\rho = 1.0$. The x-axis represents the number of objects.	98
4.12	[top] RMSD of configuration and end-effector position on a sampled trajectory executed with a maximum speed of 1.57rad/s on real robots. [bottom] The average Q value of 5 sampled trajectories executed at different maximum speeds (sim denotes execution in simulation; otherwise, the execution is on a real robot). Note that the lines of BL and BL-TP overlap with each other.	102
4.13	Trajectories of BL, BL-TP, and MODAP for the a typical rearrangement task. Each row, from top to bottom, corresponds to a robot joint in radians from one to six. Each column shows the trajectory of the six joint angles of a robot.	103
4.14	Average execution time (left) and trajectory total length (right) computed by compared methods under different overlap ratios ρ and the number of workspace objects.	104
4.15	Two examples of start and goal configurations with 15 objects at overlap rates $\rho = 1$ (a, b) and $\rho = 0.5$ (c, d). (a) and (c) (resp., (b) and (d)) are starting (resp., goal) configurations.	104
5.1	[Left] An example of the EE scenario, where the table is small and the robot can reach all poses from a fixed position. We count the traveling cost of the end-effector (EE) in the cost function. [Right] An example of the MB scenario, where the table is large and the robot can only reach a portion of tabletop poses from a fixed position. We count the traveling cost of the mobile base (MB) in the cost function.	109

5.2	[Left] An example of MB scenario, where the robot (gray disc) travels along the green table following the black track along the table boundaries. To pick/place an object on the table, the robot moves to the nearest position before the manipulation. [Right] A working example where o_1 and o_2 block each other's goal pose. One must move to a buffer pose to finish the rearrangement.	110
5.3	An example input of StabilNet when attempting to place a cup right on top of an apple in the environment. The ground truth label given by the simulation is a failure.	114
5.4	Examples of disc instances. [Left] EE scenario with $\rho = 0.2$; [Middle] MB scenario with $\rho = 0.2$; [Right] EE scenario with $\rho = 0.5$. Colored and transparent discs represent the initial and goal arrangements respectively.	117
5.5	Examples of instances with general-shaped objects in [Left] EE and [Right] MB scenarios.	117
5.6	Algorithm performance in EE disc instances with $\rho = 0.2$ and 5-11 objects. (a) # pick-n-places in solutions as multiplies of $ \mathcal{O} $. (b) Traveling cost (m). (c) Computation time (secs). (d) Success rate.	118
5.7	Algorithm performance in EE disc instances with $\rho = 0.5$ and 5-11 objects. (a) # pick-n-places in solutions as multiplies of $ \mathcal{O} $. (b) Traveling cost (m). (c) Computation time (secs). (d) Success rate.	119
5.8	Algorithm performance in MB disc instances with $\rho = 0.2$ and 5-11 objects. (a) # pick-n-places in solutions as multiplies of $ \mathcal{O} $. (b) Traveling cost (m). (c) Computation time (secs). (d) Success rate.	119
5.9	(a) A synthesized environment height map and the depth image of the placed object from the bottom. All objects are from the training set. (b) The corresponding stability prediction distribution of (a). (c) A synthesized environment height map and the depth image of the placed object from the bottom. All objects are outside the training set. (d) The corresponding stability prediction distribution of (c).	120
5.10	Algorithm performance in [Top] EE scenario and [Bottom] MB scenario with general-shaped objects. $\rho = 0.25$ and 5-11 objects. (a) # pick-n-places in solutions as multiplies of $ \mathcal{O} $. (b) Traveling cost (m). (c) Computation time (secs). (d) Success rate.	121

A.1	(a) The number of disjoint d -sided regular polygons that overlap with one d -sided regular polygon is upper bounded by that whose centers are inside a 2-circle. (b) The number of disjoint d -sided regular polygons whose centers are inside a 2-circle is upper bounded by the number of disjoint $\cos(\frac{\pi}{d})$ -circles whose centers are inside a 2-circle. (c) The number of disjoint $\cos(\frac{\pi}{d})$ -circles whose centers are inside a 2-circle is equal to the number of $\cos(\frac{\pi}{d})$ -circles packed inside a $(2 + \cos(\frac{\pi}{d}))$ -circle.	126
A.2	[Left] A case discussed in Prop.Proposition 2.3.3 [Right] A counterexample of the proof of Prop.Proposition 2.3.3 when the base of workspace objects is square.	127
A.3	Some cases discussed in the Lemma A.0.1. The unshaded and shaded nodes represent the start and goal vertices in the dependency graph. Specifically, the shaded nodes with a dot inside represent the filled vertices and the unshaded nodes with a cross inside represent the cleared vertices. (a) When only one goal vertex in $p_{i,j}$ and $p_{i+1,j}$ is filled up, the start vertex in the other vertex pair is a cleared vertex. (b) When both goal vertices in $p_{i,j}$ and $p_{i+1,j}$ are filled but neither of those in $p_{i,j+1}$ and $p_{i+1,j+1}$ is filled, one of the start vertices $p_{i,j+1}$ and $p_{i+1,j+1}$ is a cleared vertex. (c) The opposite case of (b).	128
B.1	[Top] A path on the interval state space for the example instance in Figure 4.1[Left]. [Bottom] The corresponding task schedule for the instance.	133

CHAPTER 1

INTRODUCTION AND BACKGROUND

This thesis provides a brief overview of my works on tabletop rearrangement planning. Rearrangement planning is required in nearly all aspects of our daily lives. Be it work-related, at home, or for play, objects are to be grasped and rearranged, e.g., tidying up a messy desk, cleaning the table after dinner, or solving a jigsaw puzzle. Similarly, many industrial and logistics applications require repetitive rearrangements of many objects, e.g., the sorting and packaging of products on conveyors with robots, and doing so efficiently is of critical importance to boost the competitiveness of the stakeholders.

However, even without the challenge of grasping, deciding the object manipulation order for optimizing a rearrangement task is non-trivial. To that end, [1] examined the problem of *tabletop object rearrangement with overhand grasps* (TORO), where objects may be picked up, moved around, and then placed at poses that are not in collision with other objects. An object that is picked up but cannot be directly placed at its goal is temporarily stored at a *buffer*. For example, for the setup given in Figure 1.1, using a single manipulator, either the Coke or the Pepsi must be moved to a buffer before the task can be completed.

The thesis introduces efforts to solve the two main challenges in TORO : (1) the inherent



Figure 1.1: A TORO instance where the three soda cans are to be rearranged from the left configuration to the right configuration.

combinatorial challenge in action sequencing, and (2) buffer pose allocation when objects need temporary placements. Chapter 2 and Chapter 3 investigate single-arm TORO with external and internal buffers. Chapter 4 extends the single-arm planners to dual-arm setups, where two robot arms cooperate to rearrange objects in a confined shared workspace. Chapter 5 proposes time-optimal rearrangement planners and examines the idea in a mobile robot setup.

Chapter 2 investigates TORO with external buffers (TORE), where external free space is assumed for buffer allocation. Details can be found in publications P4 and P7. This setup raises the natural question of how many simultaneous storage spaces, or “running buffers”, are required to make certain tabletop rearrangement problems feasible. This work examines the problem for both labeled and unlabeled settings. On the structural side, we observe that finding the minimum number of running buffers (MRB) can be carried out on a dependency graph abstracted from a problem instance and show that computing MRB is NP-hard. We then prove that under both labeled and unlabeled settings, even for uniform cylindrical objects, the number of required running buffers may grow unbounded as the number of objects to be rearranged increases. We further show that the bound for the unlabeled case is tight. On the algorithmic side, we develop effective exact algorithms for finding MRB for both labeled and unlabeled tabletop rearrangement problems, scalable to over a hundred objects under very high object density. More importantly, our algorithms also compute a sequence witnessing the computed MRB that can be used for solving object rearrangement tasks. Employing these algorithms, empirical evaluations reveal that random labeled and unlabeled instances, which more closely mimic real-world setups generally have fairly small MRBs. Using real robot experiments, we demonstrate that the running buffer abstraction leads to state-of-the-art solutions for the in-place rearrangement of many objects in a tight, bounded workspace.

In contrast to TORE, there are many practical rearrangement scenarios where objects have to be displaced inside the workspace. Chapter 3 applies the proposed TORE algorithms

to TORO with internal buffers (TORI). Details of this study can be found in publications P3 and P6. In a given TORI instance, objects may need to be placed at temporary positions (“buffers”) to complete the rearrangement. However, allocating these buffer locations can be highly challenging in a cluttered environment. To tackle the challenge, a two-step baseline planner is first developed, which generates a primitive plan based on inherent combinatorial constraints induced by start and goal poses of the objects and then selects buffer locations assisted by the primitive plan. We then employ the “lazy” planner in a tree search framework which is further sped up by adapting a novel preprocessing routine. Simulation experiments show our methods can quickly generate high-quality solutions and are more robust in solving large-scale instances than existing state-of-the-art approaches.

Chapter 4 employs the idea of lazy buffer verification for dual-arm task planning and coordination. Details of this work can be found in publications P1 and P5. In a non-monotone rearrangement task, complex object-object dependencies require moving some objects multiple times to solve an instance. In working with two arms in a large workspace, some objects must be handed off between the robots, which further complicates the planning process.

For task planning in the challenging dual-arm tabletop rearrangement problem, we develop effective algorithms for scheduling the pick-n-place sequence that can be properly distributed between the two arms. We show that, even without using a sophisticated motion planner, our method achieves significant time savings in comparison to greedy approaches and naive parallelization of single-robot plans.

For motion planning, we aim at optimizing motion plans for a real dual-arm system in which the two arms operate in close vicinity to solve highly constrained tabletop multi-object rearrangement problems. Toward that, we construct a tightly integrated planning and control optimization pipeline, **Makespan-Optimized Dual-Arm Planner** (MODAP) that combines novel sampling techniques for task planning with state-of-the-art trajectory optimization techniques. Compared to previous state-of-the-art, MODAP produces task and motion

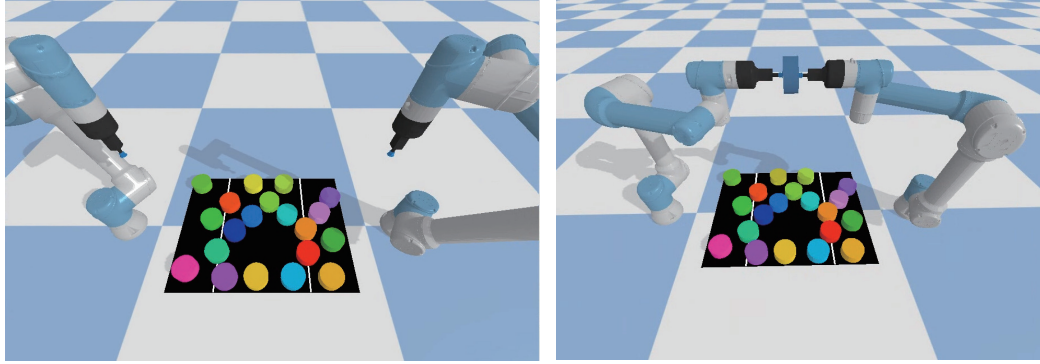


Figure 1.2: [Left] PyBullet setup for the Cooperative Multi-Robot Rearrangement problem, where only a portion of the environment (the region between two white lines) is reachable by both arms. [Right] Handoff operation at a pre-computed pose above the environment.

plans that better coordinate a dual-arm system, delivering significantly improved execution time improvements while simultaneously ensuring that the resulting time-parameterized trajectory conforms to specified acceleration and jerk limits.

Chapter 5 further integrates the idea of lazy buffer verification into the A* framework, enabling time-optimal multi-object rearrangement planning. The idea is examined in the scenario of mobile robot tabletop rearrangement (Figure 1.3). Details of this work can be found in publications P2.

In this work, we propose ORLA*, which leverages delayed/lazy evaluation in searching for a high-quality object pick-n-place sequence that considers both end-effector and mobile robot base travel. ORLA* readily handles multi-layered rearrangement tasks powered by learning-based stability predictions. Employing an optimal solver for finding temporary locations for displacing objects, ORLA* can achieve global optimality. Through extensive simulation and ablation study, we confirm the effectiveness of ORLA* in delivering high quality solutions for challenging rearrangement instances.



Figure 1.3: An example of the Mobile Robot Tabletop Rearrangement (MoTaR) setup.

CHAPTER 2

RUNNING BUFFER MINIMIZATION (RBM) FOR TORO WITH EXTERNAL BUFFERS (TORE)

2.1 Motivation

This chapter investigates TORO with external buffers (TORE), where we assume an external free space to temporarily place objects during the rearrangement process. In TORE, the study focuses on a practical rearrangement objective of minimizing the number of *running buffers* (RB) in solving a TORE instance, which is the number of objects stored at buffers simultaneously. The maximum running buffer during rearrangement is denoted as MRB. Whereas the total number of buffers used has more bearing on global solution optimality, MRB sheds more light on *feasibility*. Knowing the MRB tells us whether a certain number of external buffers will be sufficient for solving a class of rearrangement problems. This is critical for practical applications where the number of external buffers is generally limited to a small constant. For example, in solving everyday rearrangement tasks, e.g., sorting or retrieving items in the fridge, a human may attempt to temporarily hold multiple items, sometimes awkwardly. There is clearly a limit to the number of items that can be held simultaneously this way.

This chapter brings forth several novel technical contributions. First, we show that computing MRB on arbitrary *dependency graphs*, which encode the combinatorial information of TORE instances, is NP-hard. Second, this study establishes that for an n -object TORE instance, MRB can be lower bounded by $\Omega(\sqrt{n})$ for uniform cylinders, even when all objects are *unlabeled*. This implies that the same is true for the *labeled* setting. Third, we provide a matching algorithmic upper bound $O(\sqrt{n})$ for the unlabeled setting. Fourth, we develop multiple highly effective and optimal algorithms for computing rearrangement

plans with MRB for TORO . In particular, we present a dynamic programming method for the labeled setting, a priority queue-based algorithm for the unlabeled setting, and a much more efficient *depth-first-search dynamic programming* routine that readily scales to instances with over a hundred objects for both settings. Furthermore, methods for computing plans with the minimum number of *total buffers* subject to the MRB constraints are provided. These algorithms not only provide the optimal number of buffers but also provide a rearrangement plan that witnesses the optimal solution.

2.2 Related Work

As a high utility capability, manipulation of objects in a bounded workspace has been extensively studied, with works devoted to perception/scene understanding [2, 3, 4, 5], task/rearrangement planning [6, 7, 8, 9, 10, 1, 11], manipulation [12, 13, 14, 15, 16, 17, 18, 19], as well as integrated, holistic approaches [20, 21, 22, 23, 24]. As object rearrangement problems often embed within them multi-robot motion planning problems, rearrangement inherits the PSPACE-hard complexity [25]. These problems remain NP-hard even without complex geometric constraints [26]. Considering rearrangement plan quality, e.g., minimizing the number of pick-n-places or the end-effector travel, is also computationally intractable [1].

For rearrangement tasks using mainly prehensile actions, the algorithmic studies of Navigation Among Movable Obstacles [6, 27] result in backtracking search methods that can effectively deal with monotone instances which restrict the robot to move each obstacle at most once. Via carefully calling monotone solvers, difficult non-monotone cases can be solved as well [9, 28]. [1] relates tabletop rearrangement problems to the Traveling Salesperson Problem [29] and the Feedback Vertex Set problem [30], both of which are NP-hard. Nevertheless, integer programming models could quickly compute high-quality solutions for practical sized (~ 20 objects) problems. Focusing mainly on the unlabeled setting, bounds on the number of pick-n-places are provided for disk objects in [31]. In [11],

a complete algorithm is developed that reasons about object retrieval, rearranging other objects as needed, with later work [32] considering plan optimality and sensor occlusion. While objectives in most problems focus on the number of motions, [33] seeks to minimize the space needed to carry out a rearrangement task for discs moving inside the workspace.

Non-prehensile rearrangement has also been extensively studied [34, 35], with object singulation as an early focus [36, 37, 38]. In this problem, a robot is tasked to separate a target object from surrounding obstacles with non-prehensile actions, e.g., pushing and poking, in order to provide room for performing grasping actions. An iterative search was employed in [35] for accomplishing a multitude of rearrangement tasks spanning singulating, separation, and sorting of identically shaped cubes. [39] combines Monte Carlo Tree Search with a deep policy network for separating many objects into coherent clusters within a bounded workspace, supporting non-convex objects. More recently, a bi-level planner is proposed [40], engaging both (non-prehensile) pushing and (prehensile) overhand grasping for sorting a large number of objects. Synergies between non-prehensile and prehensile actions have been explored for solving clutter removal tasks [41, 42] and more challenging object retrieval tasks [43, 44] using a minimum number of pushing and grasping actions.

On the structural side, a central object that we study is the *dependency graph* structure. Similar dependency structures were first introduced to multi-robot path planning problems to deal with path conflicts between agents [45, 46]. Subsequently, the structure was employed for reasoning about and solving challenging rearrangement problems [9, 47, 48, 49]. The full labeled dependency graph, as induced by a rearrangement instance, is first introduced and studied in [1]. This current work introduces the unlabeled dependency graph. We observe that, in the labeled setting, through the dependency graph, the running buffer problems naturally connect to *graph layout* problems [50, 51, 52, 53, 54, 55], where an optimal linear ordering of graph vertices is sought. Graph layout problems find a vast number of important applications, including VLSI design, scheduling [56], and so on. For the unlabeled setting, the dependency graph becomes a planar one for uniform objects with a

round base. Rearrangement can be tackled through partitioning of the dependency graph using a *vertex separator* [57, 58, 59, 60]. For a survey on these topics, see [50].

2.3 TORO with External Buffer Space (TORE)

For TORE tasks where objects assume similar geometry, there are two natural practical settings depending on whether the objects are distinguishable, i.e., whether they are *labeled* or *unlabeled*. We describe external buffer formulations under these two distinct settings, and discuss the important *dependency graph* structure for both.

2.3.1 Labeled TORO with External Buffers

Consider a bounded workspace $\mathcal{W} \subset \mathbb{R}^2$ with a set of n objects $\mathcal{O} = \{o_1, \dots, o_n\}$ placed inside it. All objects are assumed to be *generalized cylinders* with the same height. A *feasible arrangement* of these objects is a set of poses $\mathcal{A} = \{x_1, \dots, x_n\}, x_i \in SE(2)$ in which no two objects collide. Let $\mathcal{A}_s = \{x_1^s, \dots, x_n^s\}$ and $\mathcal{A}_g = \{x_1^g, \dots, x_n^g\}$ be two feasible arrangements, a tabletop object rearrangement problem [1] seeks a plan using *pick-n-place* operations that move the objects from \mathcal{A}_s to \mathcal{A}_g (see Figure 2.1(a) for an example with 7 uniform cylinders). In each pick-n-place operation, an object is grasped by a robot arm, lifted above all other objects, transferred to and lowered at a new pose $p \in SE(2)$ where the object will not be in collision with other objects, and then released. A pick-n-place operation can be formally represented as a 3-tuple $a = (i, x', x'')$, denoting that object o_i is moved from pose x' to pose x'' . A full rearrangement plan $P = (a_1, a_2, \dots)$ is then an ordered sequence of pick-n-place operations.

Depending on \mathcal{A}_s and \mathcal{A}_g , it may not always be possible to directly transfer an object o_i from x_i^s to x_i^g in a single pick-n-place operation, because x_i^g may be occupied by other objects. This creates *dependencies* between objects. If object o_i at pose x_i^g intersects objects o_j at pose x_j^s , we say o_i *depends* on o_j . This suggests that object o_j must be moved first before o_i can be placed at its goal pose x_i^g .

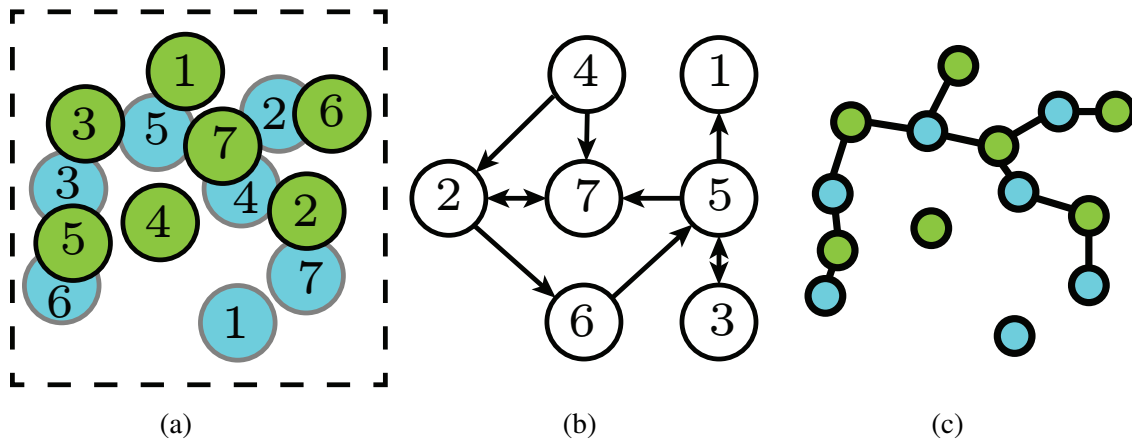


Figure 2.1: A 7-object labeled instance with uniform cylinders; we will use this instance as a running example. (a) The unshaded discs (as projections of cylinders) represent the start arrangement \mathcal{A}_s and the shaded discs represent the goal arrangement \mathcal{A}_g . (b) The corresponding labeled dependency graph. (c) The corresponding unlabeled dependency graph, which is bipartite and planar.

It is possible to have circular dependencies. As an example, for the instance given in Figure 2.1(a), objects 3 and 5 have dependencies on each other. In such cases, some object(s) must be temporarily moved to an intermediate pose to solve the rearrangement problem. Similar to [1], for this chapter, we assume that *external buffers* outside the workspace are used for intermediate poses, which avoids time-consuming geometric computations if the intermediate poses are to be placed within \mathcal{W} . During the execution of a rearrangement plan, multiple objects can be stored at buffer locations. We call the buffers that are currently in use *running buffers* (RB). With the introduction of buffers, there are three types of pick-n-place operations: 1) pick an object at its start pose and place it at a buffer, 2) pick an object at its start pose and place it at its goal pose, and 3) pick an object from a buffer and place it at its goal pose. Naturally, it is desirable to be able to solve a rearrangement problem with the least number of running buffers, giving rise to the *labeled running buffer minimization* problem.

Problem 1 (Labeled Running Buffer Minimization (LRBM)). *Given feasible arrangements \mathcal{A}_s and \mathcal{A}_g , find a rearrangement plan P that minimizes the maximum number of running buffers in use at any given time as the plan is executed.*

In an LRBM instance, the set of all dependencies induced by \mathcal{A}_s and \mathcal{A}_g can be represented using a directed graph $G^\ell = (V, A)$, where each $v_i \in V$ corresponds to object o_i and there is an arc $v_i \rightarrow v_j$ for $1 \leq i, j \leq n, i \neq j$ if object o_i depends on object o_j . We call G^ℓ a *labeled dependency graph*. The labeled dependency graph for Figure 2.1(a) is given in Figure 2.1(b). Based on the dependency graph G^ℓ , we can immediately identify multiple circular dependencies in the graph, e.g., between objects 3 and 5, or among objects 7, 2, 6 and 5. The cycles form strongly connected components of G^ℓ , which can be effectively computed [61]. Since moving objects to external buffers does not create additional dependencies, we have

Proposition 2.3.1. *G^ℓ fully captures the information needed to solve the tabletop rearrangement problem with external buffers moving objects from \mathcal{A}_s to \mathcal{A}_g .*

We use two examples to illustrate the relationships between TORE, its dependency graph, and external buffer-based solutions. First, for the example given in Figure 1.1, the corresponding start/goal configurations are given in Figure 2.2[top left]. The labeled dependency graph is given in Figure 2.2[top right]. Because of the existence of cyclic dependencies between Coke and Pepsi, one of these two must be temporarily moved to a buffer. Suppose that Pepsi is moved to buffer. This changes the configuration and dependency graph as shown in the second row of Figure 2.2. The TORE instance can then be readily solved. The complete solution sequence is $\langle \text{Pepsi} \rightarrow b, \text{Coke} \rightarrow g, \text{Pepsi} \rightarrow g, \text{Fanta} \rightarrow g \rangle$, where b refers to a buffer and g refers to the goal of the corresponding object.

For the example given in Figure 2.1[a], its labeled dependency graph Figure 2.1[b] shows two cycles ($2 \leftrightarrow 7$ and $3 \leftrightarrow 5$). One planning sequence for solving this can be derived that moves 2 and 3 to buffer: $\langle 1 \rightarrow g, 2 \rightarrow b, 3 \rightarrow b, 7 \rightarrow g, 4 \rightarrow g, 5 \rightarrow g, 6 \rightarrow g, 2 \rightarrow g, 3 \rightarrow g \rangle$.

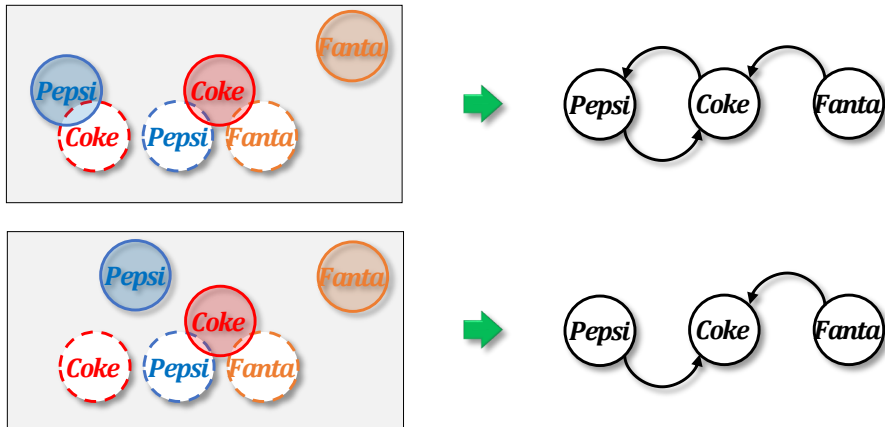


Figure 2.2: Two configurations of the setup given in Figure 1.1 and the corresponding dependency graphs.

2.3.2 Unlabeled TORO with External Buffers

In the unlabeled setting, objects are interchangeable. That is, it does not matter which object goes to which goal. For example, in Figure 2.1, object 5 can move to the goal for object 6. We call this version the *unlabeled running buffer minimization* (URBM) problem, which is intuitively easier. The plan for the unlabeled problem can be represented similarly as the labeled setting; we continue to use labels so that plans can be clearly represented but do not require matching labels for start and goal poses.

For the unlabeled setting, the dependency structure remains but appears in a different form. It is now an *undirected bipartite* graph. That is, $G^u = (V_s \cup V_g, E)$ where each $v \in V_s$ (resp., $v \in V_g$) corresponds to a start (resp., goal) pose $p \in \mathcal{A}_s$ (resp., $p \in \mathcal{A}_g$). We denote the vertices representing the start and goal poses as *start vertices* and *goal vertices*, respectively. There is an edge between $v_s \in V_s$ and $v_g \in V_g$ if the objects at the corresponding poses overlap. The unlabeled dependency graph for Figure 2.1(a) is illustrated in Figure 2.1(c).

In practice, many TORE instances have objects with footprints that are uniform regular polygons (e.g., squares) or discs. In such settings, we can say something additional about the resulting unlabeled dependency graphs (the proofs of the two propositions below can

be found in the appendix (Appendix A)).

Proposition 2.3.2. *For unlabeled TORE where footprints of objects are uniform regular polygons, the maximum degree of the unlabeled dependency graph is upper bounded by 19.*

Proposition 2.3.3. *For unlabeled TORE where footprints of objects are uniform discs, the dependency graph is a planar bipartite graph with a maximum degree of 5.*

For either LRBM or URBM, the minimum required number of running buffers is denoted as MRB, which can be computed based on the corresponding dependency graph.

2.4 Structural Analysis and NP-Hardness

The introduction of running buffers to tabletop rearrangement problems induces unique and interesting structures. We highlight some important structural properties of LRBM, including the comparison to minimizing the total number of buffers [1], the solutions of LRBM and *linear arrangement* [62] or *linear ordering* [63] of its dependency graph, and the hardness of computing MRB for TORE.

As will be established in this section, computing MRB solutions for TORE is intimately connected to finding a certain optimal linear ordering of vertices in the associated dependency graph. Since finding an optimal linear ordering is hard, it renders computing MRB solutions hard as well. This in turn limits the algorithmic solutions that one can secure for computing MRB solutions for TORE tasks.

2.4.1 Running Buffer versus Total Buffer

In solving TORE, running buffers are related to but different from the total number of buffers, as studied in [1]. It is shown that the minimum number of total buffers for solving TORE is the same as the size of the minimum *feedback vertex set* (FVS) of the underlying dependency graph. An FVS is a set of vertices the removal of which leaves a graph acyclic.

A TORE with an acyclic dependency graph can be solved without using any buffer because there are no cyclic dependencies between any pairs of objects. We denote the size of the minimum FVS as MFVS.

As a labeled TORE problem, the example from Figure 1.1 has $\text{MFVS} = \text{MRB} = 1$. For the example from Figure 2.1(a)(b), $\text{MFVS} = 2$ (an FVS set is $\{2, 3\}$) and $\text{MRB} = 2$.

As an extreme example illustrating the difference between MRB and MFVS, consider a labeled dependency graph that is formed by n copies of 2-cycles, e.g., Figure 2.3. On one hand, the MFVS of the instance is n because one vertex must be removed from each of the n cycles to make the graph acyclic. On the other hand, the MRB is just 1 because each cyclic dependency can be resolved independently from other cycles using a single external buffer. Therefore, whereas the total number of buffers used has more bearing on global solution optimality, MRB sheds more light on *feasibility*. Knowing the MRB tells us whether a certain number of external buffers will be sufficient for solving a class of rearrangement problems. This is critical for practical applications where the number of external buffers is generally limited to be a small constant. For example, in solving everyday rearrangement tasks, e.g., sorting things or retrieving items in the fridge, a human may attempt to temporarily hold multiple items, sometimes awkwardly. There is clearly a limit to the number of items that can be held simultaneously this way.

We give an example where the MRB and MFVS cannot always be optimized simultaneously, i.e., they form a Pareto front. For the setup in Figure 2.4, the MFVS $\{7, 9, 10\}$ has size 3 - it can be readily checked that deleting $\{7, 9, 10\}$ leaves the dependency graph acyclic. Using our algorithms, the MRB can be computed to be 2 with the witness sequence being 1, 10, 8, 4, 5, 3, 6, 7, 2, 9, corresponding to the plan of $\langle 1 \rightarrow g, 10 \rightarrow b, 8 \rightarrow g, 4 \rightarrow b, 5 \rightarrow g, 3 \rightarrow g, 10 \rightarrow g, 6 \rightarrow b, 7 \rightarrow g, 6 \rightarrow g, 2 \rightarrow b, 9 \rightarrow g, 4 \rightarrow g, 2 \rightarrow g \rangle$, where b refers to a buffer and g refers to the goal of the corresponding object. The RB reaches the maximum 2 when 4 and 6 are moved to the buffer. However, in this case, the total number of buffers used is 4: 2, 4, 6, and 10 are moved to buffers. This turns out to be the best we

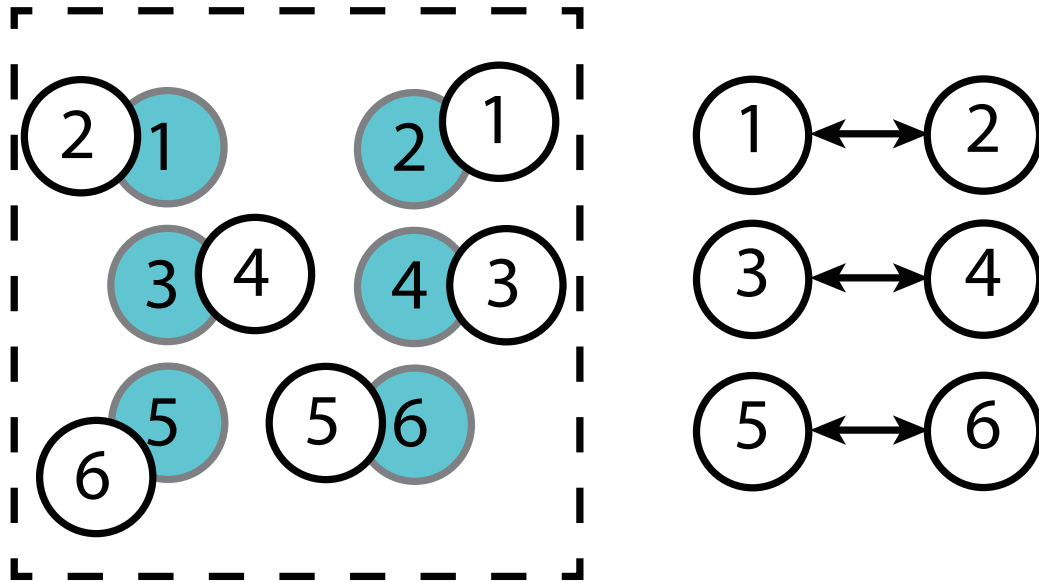


Figure 2.3: An instance with the labeled dependency graph formed by 3 copies of 2-cycles. The MFVS is 3. On the other hand, the MRB is just 1 for the problem. The example scales to have arbitrarily large MFVS with MRB remaining at 1.

can do for this example, that is, if we are constrained by solutions with $\text{MRB} = 2$, the total number of buffers that must be used is at least 4 instead of the MFVS size of 3.

We note that it is rarely the case that MFVS will be larger when the solution space is constrained to MRB solutions; for uniform cylinders, for example, the total number of buffers needed after first minimizing the running buffer is almost always the same as the MFVS size.

2.4.2 Running Buffers and Linear Vertex Ordering

Given a graph with vertex set V , a *linear ordering* of V is a bijective function

$$\varphi : \{1, \dots, |V|\} \rightarrow V$$

Given a labeled dependency graph $G^\ell(V, A)$ for an LRBM problem and a linear ordering φ for V , we may turn φ into a plan P for the LRBM problem by sequentially picking up objects corresponding to vertices $\varphi(1), \varphi(2), \dots$. For each object that is picked up, it is moved to

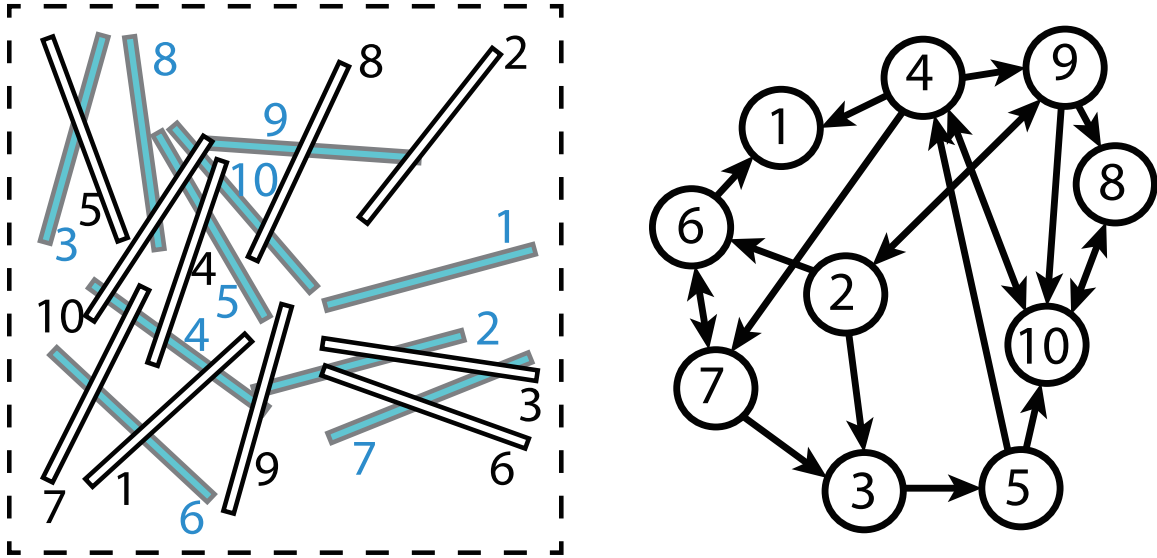


Figure 2.4: An LRBM instance with uniform thin cuboids (left) and its labeled dependency graph, where the total number of buffers needed is more than the size of the MFVS when the number of running buffers is minimized.

its goal pose if it has no further dependencies; otherwise, it is stored in the buffer. Objects already in the buffer will be moved to their goal pose at the earliest possible opportunity.

For example, given the linear ordering 1, 5, 6, 3, 4, 2, 7 for the dependency graph from Figure 2.1(b), first, 1 can be directly moved to its goal. Then, 5 is moved to the buffer because it has dependencies on 3 and 7 (but no longer on 1). Then, 6 can be directly moved to its goal because 5 is now at a buffer location. Similarly, 3 can be moved to its goal next. Then, 4 and 2 must be moved to the buffer, after which 7 can be moved to its goal directly. Finally, 2, 4, and 5 can be moved to their respective goals from the buffer. This leads to a maximum running buffer size of 3. This is not optimal; an optimal sequence is 5, 6, 2, 7, 4, 3, 1, with $\text{MRB} = 2$. Both sequences are illustrated in Figure 2.5.

The discussion suggests that we may effectively view the number of running buffers as a function of a dependency graph G^ℓ and a linear ordering φ . We thus define $\text{RB}(G^\ell, \varphi)$ as the number of running buffers needed for rearranging G^ℓ following the order given by φ . It is straightforward to see that $\text{MRB}(G^\ell) = \min_{\varphi} \text{RB}(G^\ell, \varphi)$.

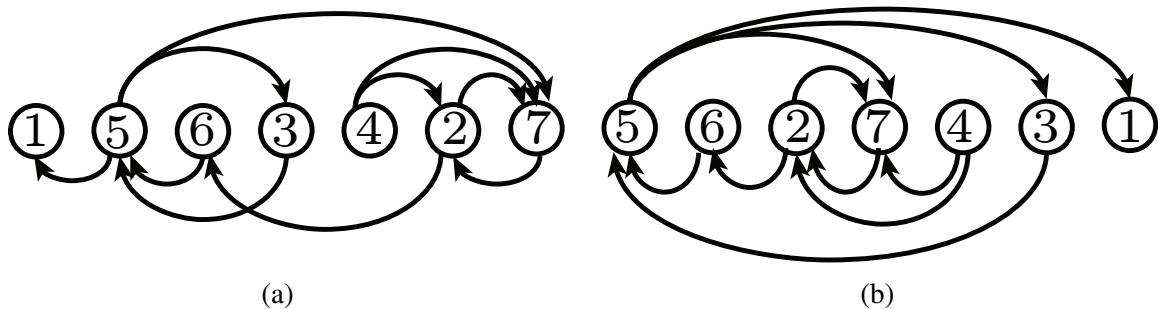


Figure 2.5: Two linear orderings of vertices of the labeled dependency graph from Figure 2.1(b) (i.e., these are different representations of the same graph). The right one minimizes MRB.

2.4.3 Intractability of Computing MRB

Since computing MFVS is NP-hard [1], one would expect that computing MRB for a labeled dependency graph, which can be any directed graph, is also hard. We show that this is indeed the case, by examining the interesting relationship between MRB and the *vertex separation problem* (VSP), which is equivalent to path width, gate matrix layout, and search number problems as described in Theorem 3.1 in [50], resulting from a series of studies [64, 65, 66]. Unless $P = NP$, there cannot be an absolute approximation algorithm for any of these problems [55]. First, we describe the vertex separation problem. Intuitively, given an undirected graph $G = (V, E)$, VSP seeks a linear ordering φ of V such that, for a vertex with order i , the number of vertices that come no later than i in the ordering, with edges to vertices that come after i , is minimized.

Vertex Separation (VSP)

Instance: Graph $G(V, E)$ and an integer K .

Question: Is there a bijective function $\varphi : \{1, \dots, n\} \rightarrow V$, such that for any integer $1 \leq i \leq n$, $|\{u \in V \mid \exists(u, v) \in E \text{ and } \varphi(u) \leq i < \varphi(v)\}| \leq K$?

As an example, in Figure 2.6(a), with the given linear ordering, at the second vertex, both the first and the second vertices have edges crossing the vertical separator, yielding a crossing number of 2. Given a graph G and a linear ordering φ , we define $\text{VS}(G, \varphi) := \max_i |\{u \in V \mid \exists(u, v) \in E \text{ and } \varphi(u) \leq i < \varphi(v)\}|$, VSP seeks φ that minimizes

$\text{VS}(G, \varphi)$. Let $\text{MINVS}(G)$, the vertex separation number of graph G , be the minimum K for which a VSP instance has a yes answer, then $\text{MINVS}(G) = \min_{\varphi} \text{VS}(G, \varphi)$. Now, given an undirected graph G and a labeled dependency graph G^{ℓ} obtained from G by replacing each edge of G with two directed edges in opposite directions, we observe that there are clear similarities between $\text{VS}(G, \varphi)$ and $\text{RB}(G^{\ell}, \varphi)$, which is characterized by the following lemma.

Lemma 2.4.1. $\text{VS}(G, \varphi) \leq \text{RB}(G^{\ell}, \varphi) \leq \text{VS}(G, \varphi) + 1$.

Proof. Fixing a linear ordering φ , it is clear that $\text{VS}(G, \varphi) \leq \text{RB}(G^{\ell}, \varphi)$, since the vertices on the left side of a separator with edges crossing the separator for G correspond to the objects that must be stored at buffer locations. For example, in Figure 2.6(a), past the second vertex from the left, both the first and the second vertices have edges crossing the vertical “separator”. In the corresponding dependency graph shown in Figure 2.6(b), objects corresponding to both vertices must be moved to the external buffer. On the other hand, we have $\text{RB}(G^{\ell}, \varphi) \leq \text{VS}(G, \varphi) + 1$ because as we move across a vertex in the linear ordering, the corresponding object may need to be moved to a buffer location temporarily. For example, as the third vertex from the left in Figure 2.6(a) is passed, the vertex separator drops from 2 to 1, but for dealing with the corresponding dependency graph in Figure 2.6(b), the object corresponding to the third vertex from the left must be moved to the buffer before the first and the second objects stored in the buffer can be placed at their goals. \square

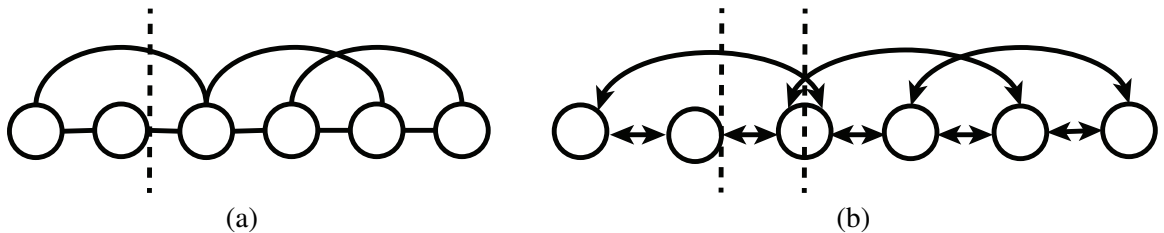


Figure 2.6: (a) An undirected graph and a linear ordering of its vertices. (b) A corresponding labeled dependency graph with the same vertex ordering.

Theorem 2.4.1. *Computing MRB, even with an absolute approximation, for a labeled dependency graph is NP-hard.*

Proof. Given an undirected graph G , we reduce from approximating VSP within a constant to approximating MRB within a constant for a dependency graph G^ℓ from G constructed as stated before, replacing each edge in G as a bidirectional dependency.

Unless $P = NP$, VSP does not have absolute approximation in polynomial time. Henceforth, if $\text{MRB}(G^\ell, \varphi)$ can be approximated within α in polynomial time, which means for graph G , we can find a φ^* in polynomial time such that $\text{RB}(G^\ell, \varphi^*) \leq \text{MRB}(G^\ell) + \alpha$, we then have $\text{VS}(G, \varphi^*) \leq \text{RB}(G^\ell, \varphi^*) \leq \alpha + \text{MRB}(G^\ell) \leq \text{MINVS}(G) + \alpha + 1$, which shows vertex separation can have an absolute approximation, implying $P = NP$. \square

With some additional effort, we can show that computing MRB solutions for certain TORE instances is NP-hard.

Theorem 2.4.2. *Computing MRB for TORE is NP-hard.*

Proof. By [67], VSP remains NP-complete for planar graphs with a maximum degree of three. From Lemma 2.4.1 and Theorem 2.4.1 and the corresponding proofs, if we can show that we can convert an arbitrary planar graph with maximum degree three into a corresponding TORE instance, then we are done. That is, all we need to show is that, if Figure 2.6(a) is a planar graph with maximum degree three, we can construct a TORE instance for which the dependency graph is Figure 2.6(b).

We proceed to show something stronger: instead of showing the above for planar graphs with a maximum degree of three, we will do so for all planar graphs. By [68], all planar graphs can be drawn in the plane without edge crossings using only straight-line edges. Given an arbitrary planar graph and one of its straight-line-edge non-crossing embedding in the plane, we show how we can convert the embedding to a corresponding TORE instance.

The construction process is explained using Figure 2.7 as an illustration, where Figure 2.7(a) shows a straight-line-edge non-crossing embedding of planar graph. We con-

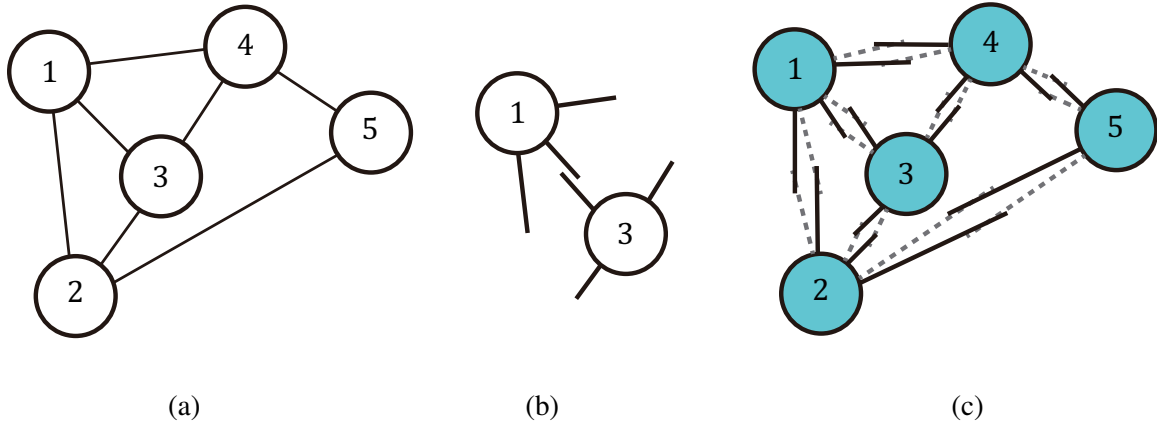


Figure 2.7: (a) An undirected planar graph with five vertices (b) “Object gadgets” for two of the vertices. (c) The corresponding TORE instance.

struct *object gadgets* based on the embedding’s geometric structure as follows. For each node of the graph, we take the node and a bit more than half of each of the edges coming out of it. For example, for nodes 1 and 3, the corresponding objects are given in Figure 2.7(b). We now construct a TORE instance with a dependency graph corresponding to replacing edges of Figure 2.7(a) with bidirectional edges. To do so, we place each object gadget as they appear in Figure 2.7(a). For the goal configuration, we rotate each object *counterclockwise* by some small angle ε around the center of the corresponding node. For the start configuration, we perform a similar rotation but in the *clockwise* direction. The process yields Figure 2.7(c) for Figure 2.7(a). It is straightforward to check that the construction converts each edge (i, j) in the planar graph into a mutual dependency between two objects i and j . For example, there is a cyclic dependency between object gadgets 1 and 3 in Figure 2.7(c). \square

2.5 Lower and Upper Bounds on MRB

After connecting computing MRB to vertex linear ordering and proving the computational intractability, we proceed to establish quantitative bounds on MRB, i.e., what is the lowest possible MRB for LRBM and URBM, and what is the best that we can do to lower MRB?

2.5.1 Intrinsic MRB Lower Bounds

When there is no restriction on object geometry, MRB can easily reach the maximum possible $n - 1$ for an n object instance, even in the URBM case. An example of when this happens is given in Figure 2.8, where $n = 6$ thin cuboids are aligned horizontally in \mathcal{A}_s , one above the other. The cuboids are vertically aligned in \mathcal{A}_g . Every pair of start pose and goal pose then induces a (unique) dependency. Clearly, this yields a bidirectional K_6 labeled dependency graph in the LRBM case and a $K_{6,6}$ unlabeled dependency graph in the URBM case. For both, $n - 1 = 5$ objects must be moved to buffers before the problem can be resolved. The example readily generalizes to an arbitrary number of objects.

Proposition 2.5.1. *MRB lower bound is $n - 1$ for n objects for both LRBM and URBM, which is the maximum possible, even for uniform convex objects.*

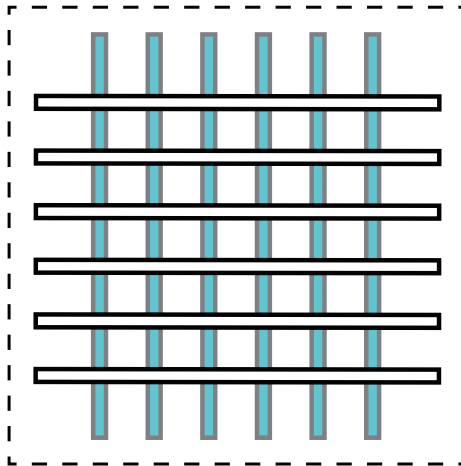


Figure 2.8: An instance with 6 cuboids where horizontal and vertical sets represent start and goal poses, respectively. An arbitrary labeling of the objects may be given in the labeled setting.

The lower bound on MRB being $\Omega(n)$ is undesirable, but it seems to depend on having objects that are thin; everyday objects are not often like that. An ensuing question of high practical value is then: what happens when the footprint of the objects is “fat”? Next, we establish that, the lower bound drops to $\Omega(\sqrt{n})$ for uniform cylinders, which approximate

many real-world objects/products. Furthermore, we show that this lower bound is tight for URBM (in Section Subsection 2.5.2).

For convenience, assume n is a perfect square, i.e., $n = m^2$ for some integer m . To establish the $\Omega(\sqrt{n})$ lower bound, a grid-like unlabeled dependency graph is used, which we call a *dependency grid*, where \mathcal{A}_s and \mathcal{A}_g have similar patterns with \mathcal{A}_g offset from \mathcal{A}_s to the left (or right/above/below) by the length of one grid edge. An illustration of a portion of such a setup is given in Figure 2.9. We use $\mathcal{D}(w, h)$ to denote a dependency grid with w columns and h rows.

Lemma 2.5.1. *Given a URBM instance with $n = m^2$ objects and whose dependency graph is $\mathcal{D}(m, 2m)$, its MRB is lower bounded by $\Omega(m) = \Omega(\sqrt{n})$*

Because the proof has limited relevance to the delivery of the main contributions of the paper, we highlight the main idea and refer the readers to the appendix for the complete proof. What we show is that, for certain unlabeled TORE instance with n objects with such a dependency graph, at least $\Omega(\sqrt{n})$ objects must be moved to buffers simultaneously to solve the TORE instance.

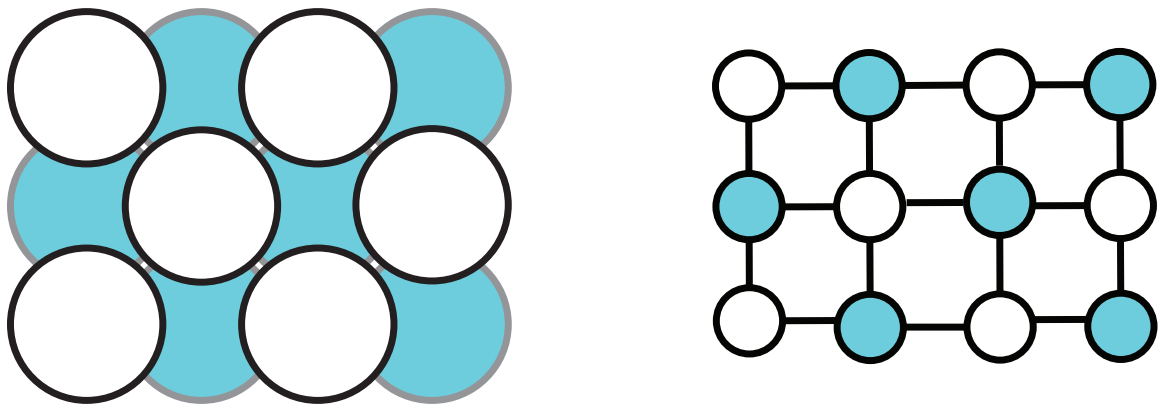


Figure 2.9: A URBM instance (left) and its unlabeled dependency graph (right), a 4×3 dependency grid. Unshaded (resp., shaded) discs/vertices indicate start poses (resp., goal poses).

Because URBM instances always have lower or equal MRB than the LRBM instances with the same objects and goal placements, the conclusion of Lemma 2.5.1 directly applies

to LRBM. Therefore, we have

Theorem 2.5.1. *For both URBM and LRBM with n uniform cylinders, MRB is lower bounded by $\Omega(\sqrt{n})$.*

For uniform cylinders, while the lower bound on URBM is tight (as shown in Section Subsection 2.5.2), we do not know whether the lower bound on LRBM is tight; our conjecture is that $\Omega(\sqrt{n})$ is not a tight lower bound for LRBM. Indeed, the $\Omega(\sqrt{n})$ lower bound can be realized when uniform cylinders are simply arranged on a cycle, an illustration of which is given in Figure 2.10. For a general construction, for each object o_i , let o_i depend on $o_{(i-1 \bmod n)}$ and $o_{(i+\sqrt{n} \bmod n)}$, where n is the number of objects in the instance. From the labeled dependency graph, we can construct the actual LRBM instance where start and goal arrangements both form a cycle. It can be shown that when $n/2$ objects are at the goal poses, $\Omega(\sqrt{n})$ objects are at the buffer. We omit the proof, which is similar in spirit to that for Lemma 2.5.1.

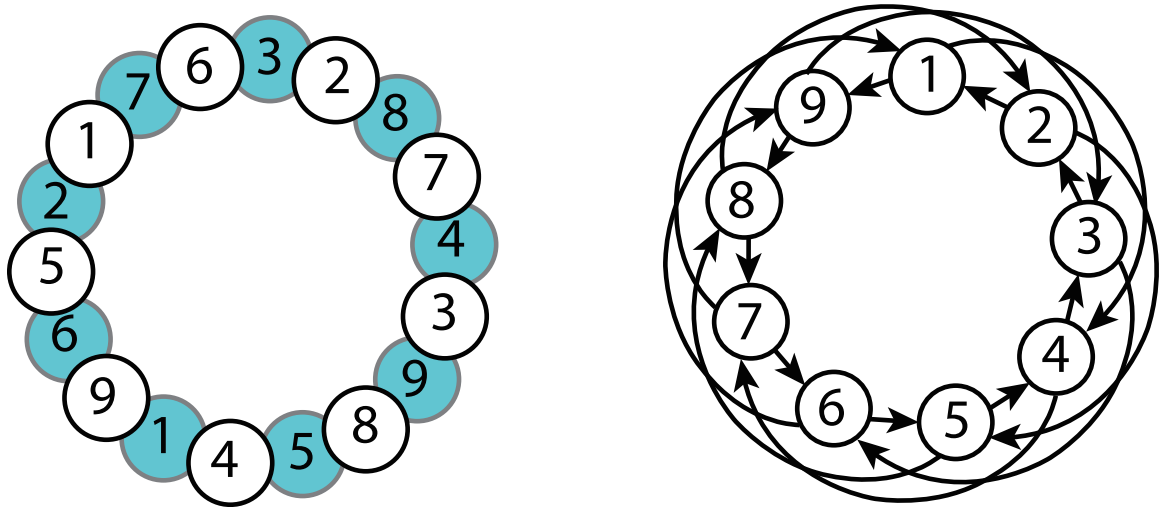


Figure 2.10: An example of a 9-object LRBM yielding $\Omega(\sqrt{n})$ MRB (left) and the corresponding dependency graph (right).

2.5.2 Upper Bounds on MRB for URBM

We now establish, regardless of how n uniform cylinders are to be rearranged, the corresponding URBM instance admits a solution using $\text{MRB} = O(\sqrt{n})$. Lower and upper bounds on URBM agree; therefore, the $O(\sqrt{n})$ bound is tight.

To prove the upper bound, We propose an $O(n \log(n))$ -time algorithm SEPPLAN for the setting based on a vertex separator of $G_{\mathcal{A}_s, \mathcal{A}_g}^u$. SEPPLAN computes a sequence of goal vertices to be removed from the dependency graph. Given a sequence of goal vertices to be removed, the running buffer size at each moment equals $\max(0, \|N(g, G_{\mathcal{A}_s, \mathcal{A}_g}^u)\| - \|g\|)$, where g is the set of removed goal vertices at this moment, and $N(g, G_{\mathcal{A}_s, \mathcal{A}_g}^u)$ is the set of neighbors of g in $G_{\mathcal{A}_s, \mathcal{A}_g}^u$. We prove that SEPPLAN can find a rearrangement plan with $O(\sqrt{n})$ running buffers.

Algorithm 1: SEPPLAN

Input : $G_{\mathcal{A}_s, \mathcal{A}_g}^u(V, E)$: unlabeled dependency graph
Output: π : goal sequence

- 1 $\pi, V, E \leftarrow \text{RemovalTrivialGoals}(G_{\mathcal{A}_s, \mathcal{A}_g}^u(V, E))$
- 2 **if** V is \emptyset **then return** π ;
- 3 $A, B, C \leftarrow \text{Separator}(G_{\mathcal{A}_s, \mathcal{A}_g}^u(V, E))$
- 4 $\pi \leftarrow \pi + g(C)$
- 5 $A' \leftarrow A - N(g(C), G_{\mathcal{A}_s, \mathcal{A}_g}^u(V, E))$
- 6 $B' \leftarrow B - N(g(C), G_{\mathcal{A}_s, \mathcal{A}_g}^u(V, E))$
- 7 $\pi_{A'} \leftarrow \text{SEPPLAN}(G_{\mathcal{A}_s, \mathcal{A}_g}^u(A', E(A')))$
- 8 $\pi_{B'} \leftarrow \text{SEPPLAN}(G_{\mathcal{A}_s, \mathcal{A}_g}^u(B', E(B')))$
- 9 **if** $\delta(A') \geq \delta(B')$ **then** $\pi \leftarrow \pi + \pi_{A'} + \pi_{B'}$;
- 10 **else** $\pi \leftarrow \pi + \pi_{B'} + \pi_{A'}$;
- 11 **return** π

The algorithm is presented in Algorithm 1. SEPPLAN consumes a graph $G_{\mathcal{A}_s, \mathcal{A}_g}^u(V, E)$, which is a subgraph of $G_{\mathcal{A}_s, \mathcal{A}_g}^u$ induced by vertex set V . To start with, the isolated goal vertices or those with only one dependency in $G_{\mathcal{A}_s, \mathcal{A}_g}^u(V, E)$ can be removed without using buffers (Line 1). After that, V can be partitioned into three disjoint subsets A , B and C [57] (Line 3), such that there is no edge connecting vertices in A and B , $|A|, |B| \leq 2|V|/3$, and $|C| \leq 2\sqrt{2|V|}$ (Figure 2.11(a)). For the start vertices in C and the neighbors of the

goal vertices in C , we remove them from $G_{\mathcal{A}_s, \mathcal{A}_g}^u$. Since there are at most 5 neighbors for each goal vertex, there are at most $10\sqrt{2|V|}$ objects moved to the buffer in this operation. After that, we remove the goal vertices in C , which should be isolated now (Line 4). Function $g(\cdot)$ obtains the goal vertices in a given vertex set. Let A', B' be the remaining vertices in A and B (Line 5-6). And correspondingly, let C' be the removed vertices, i.e., $C' := (A \cup B \cup C) \setminus (A' \cup B')$. Function $N(\cdot, \cdot)$ obtains the neighbors of a vertex set in a given dependency subgraph. With the removal of C' from $G_{\mathcal{A}_s, \mathcal{A}_g}^u$, A' and B' form two independent subgraphs (Figure 2.11(b)). We can deal with the subgraphs one after the other by recursively calling SEPPLAN (Figure 2.11(c)) (Line 7-8). Let $\delta(V') := |g(V')| - |s(V')|$ where $g(V')$ and $s(V')$ are the goal and start vertices in a vertex set V' respectively. Between vertex subsets A' and B' , we prioritize the one with larger $\delta(\cdot)$ value (Line 9-10). That is because, after solving a rearrangement subproblem induced by a vertex set V' , there is $\delta(V')$ fewer objects in buffers or $\delta(V')$ more available goal poses.

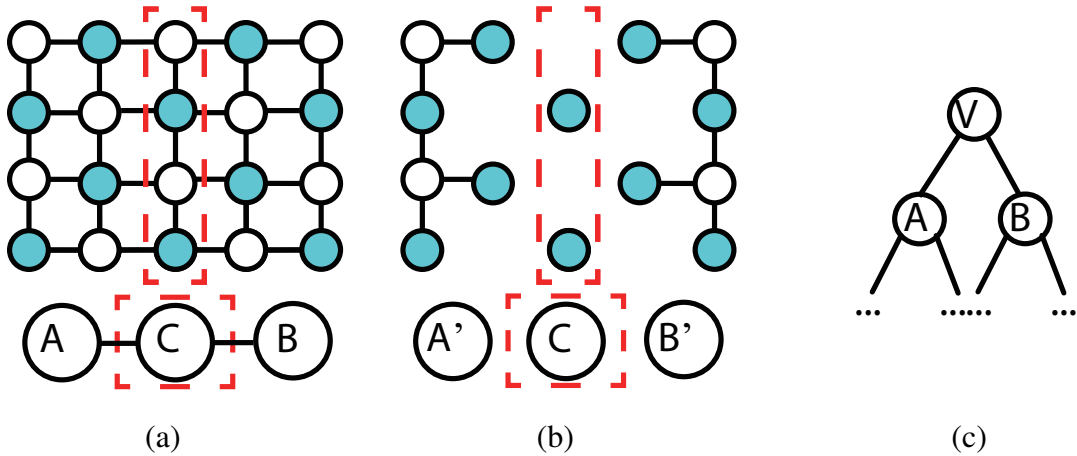


Figure 2.11: The recursive solver SEPPLAN for URBM. (a) A $O(\sqrt{|V|})$ vertex separator for the planar dependency graph. (b) By removing the start vertices in C and the neighbors of the goal vertices in C , the remaining graph consists of two independent subgraphs and isolated goal poses in C . (c) The problem can be solved by recursively calling SEPPLAN.

As shown in detail in the appendix, SEPPLAN guarantees an MRB upper bound of $\frac{20}{1 - \sqrt{2/3}}\sqrt{n}$.

Theorem 2.5.2. *For URBM with n uniform cylinders, a polynomial time algorithm can compute a plan with $O(\sqrt{n})$ RB, which implies that MRB is bounded by $O(\sqrt{n})$.*

2.6 Algorithms for TORE

In this section, several algorithms for computing solutions for TORE tasks under various MRB objectives are described. The hardness result (Theorem 2.4.2) suggests that the challenge in computing MRB solutions for TORE resides with filtering through an exponential number of vertex linear orderings of the dependency graph. This leads to our algorithms being largely search-based, which are enhanced with many effective heuristics.

We first describe a dynamic programming-based method for LRBM (Subsection 2.6.1). Then, we propose a priority queue-based method in Subsection 2.6.2 for URBM. Furthermore, a significantly faster depth-first modification of DP for computing MRB is provided in Subsection 2.6.3. Finally, we also developed an integer programming model, denoted TB_{MRB} , for computing the minimum total number of buffers needed subject to the MRB constraint, which is compared with the algorithm that computes the minimum total buffer without the MRB constraint, denoted as TB_{FVS} , from [1]. A brief description of TB_{MRB} is given in Subsection 2.6.4.

2.6.1 Dynamic Programming (DP) for LRBM

As established in Subsection 2.4.2, a rearrangement plan in LRBM can be represented as a linear ordering of object labels. That is, given an ordering of objects, π , we start with $o_{\pi(1)}$. If $x_{\pi(1)}^g$ is not occupied, then $o_{\pi(1)}$ is directly moved there. Otherwise, it is moved to a buffer location. We then continue with the second object in the order, and so on. After we work with each object in the given order, we always check whether objects in buffers can be moved to their goals, and do so if an opportunity is present. We now describe a *dynamic programming* (DP) algorithm for computing such a linear ordering that yields the MRB.

The pseudo-code of the algorithm is given in Algorithm 2. The algorithm maintains a

search tree T , each node of which represents an arrangement where a set of objects S have left the corresponding start poses. We record the objects currently at the buffer ($T[S].b$) and the minimum running buffer from the start arrangement \mathcal{A}_s to the current arrangement ($T[S].MRB$). The DP starts with an empty T . We let the root node represent \mathcal{A}_s (Line 1). At this moment, there is no object in the buffer and the MRB is 0 (Line 2-3). And then we enumerate all the arrangements with $|S| = 1, 2, \dots$ and finally n (Line 4-5). For arbitrary S , the objects at the buffer are the objects in S whose goal poses are still occupied by other objects (Line 6), i.e., $\{o \in S \mid \exists o' \in \mathcal{O} \setminus S, (o, o') \in A\}$, where A is the set of arcs in $G_{\mathcal{A}_s, \mathcal{A}_g}^\ell$. $T[S].MRB$, the minimum running buffer from the root node $T[\emptyset]$ to $T[S]$, depends on the last object o_i added into S and can be computed by enumerating o_i (Line 7-20):

$$T[S].MRB = \min_{o_i \in S} \max(T[S \setminus \{o_i\}].MRB, \\ |T[S \setminus \{o_i\}].b| + \text{TC}(S \setminus \{o_i\}, S)),$$

where the *transition cost* TC is given as

$$\text{TC}(S \setminus \{o_i\}, S) = \begin{cases} 1, & o_i \in T[S].b, \\ 0, & \text{otherwise,} \end{cases}$$

with x_i^g currently occupied (Line 10), the transition cost is due to objects dependent on o_i cannot be moved out of the buffer before moving o_i to the buffer (Line 11). Specifically, $T[S \setminus \{o_i\}].MRB$ is the previous MRB and $|T[S \setminus \{o_i\}].b| + \text{TC}(S \setminus \{o_i\}, S)$ is the running buffer size in the new transition. If $T[S].MRB$ is minimized with o_i being the last object in S from the starts, then $T[S \setminus \{o_i\}]$ is the parent node of $T[S]$ in T (Line 16-19). Once $T[\mathcal{O}]$ is added into T , $T[\mathcal{O}].MRB$ is the MRB of the instance (Line 23) and the path in T from $T[\emptyset]$ to $T[\mathcal{O}]$ is the corresponding solution to the instance.

For the LRBM instance in Figure 2.1, Table 2.1 shows $T[S].MRB$ with different last-object options when $S = \{o_2, o_5, o_6\}$. If the last object o_i is o_5 , then we need to move

Algorithm 2: Dynamic Programming for LRBM

Input : $G^\ell(\mathcal{O}, A)$: labeled dependency graph
Output: MRB: the minimum number of running buffers

```

1  $T.root \leftarrow \emptyset$ 
2  $T[\emptyset].b \leftarrow \emptyset$  % objects currently at the buffer
3  $T[\emptyset].MRB \leftarrow 0$  % current minimum running buffer
4 for  $1 \leq k \leq |\mathcal{O}|$  do
    % enumerate cases where  $k$  objects have left the start poses
5   for  $S \in k\text{-combinations of } \mathcal{O}$  do
6      $T[S].b \leftarrow \{o \in S \mid \exists o' \in \mathcal{O} \setminus S, (o, o') \in A\}$ 
        % Find the MRB from  $T[\emptyset]$  to  $T[S]$ 
7      $T[S].MRB \leftarrow \infty$ 
8     for  $o_i \in S$  do
9        $parent = S \setminus \{o_i\}$ 
10      if  $o_i \in T[S].b$  then
11         $RB \leftarrow \max(T[parent].MRB, |T[parent].b| + 1)$ 
12      end
13      else
14         $RB \leftarrow T[parent].MRB$ 
15      end
16      if  $RB < T[S].MRB$  then
17         $T[S].MRB \leftarrow RB$ 
18         $T[S].parent \leftarrow parent$ 
19      end
20    end
21  end
22 end
23 return  $T[\mathcal{O}].MRB$ 

```

o_5 into the buffer before moving o_6 out of the buffer. Therefore, even though the buffer size of the parent node and the current node are both 2, there is a moment when all three objects are at the buffer. However, when we choose o_2 or o_6 as the last object to add, the $T[S].MRB$ becomes 2.

Table 2.1: $T[S].MRB$ for different last objects ($[p] = [parent]$)

Last object	$T[p].MRB$	$T[p].b$	$T[S].b$	$T[S].MRB$
o_2	1	$\{o_5\}$	$\{o_2, o_5\}$	2
o_5	2	$\{o_2, o_6\}$	$\{o_2, o_5\}$	3
o_6	2	$\{o_2, o_5\}$	$\{o_2, o_5\}$	2

2.6.2 A Priority Queue-Based Method for URBM

Similar to LRBM, rearrangement plans for URBM can be represented by a linear ordering of goal vertices in $G_{\mathcal{A}_s, \mathcal{A}_g}^u$. We can compute the ordering that yields MRB by maintaining a search tree as we have done in Algorithm 2. Each node $T[g]$ in the tree represents an arrangement where a set of goal vertices g have been removed from $G_{\mathcal{A}_s, \mathcal{A}_g}^u$. The remaining dependencies of $T[g]$ is an induced graph of $G_{\mathcal{A}_s, \mathcal{A}_g}^u$, formed from $V(G_{\mathcal{A}_s, \mathcal{A}_g}^u) \setminus (g \cup N(g, G_{\mathcal{A}_s, \mathcal{A}_g}^u))$ where $V(G_{\mathcal{A}_s, \mathcal{A}_g}^u)$ is the vertex set of $G_{\mathcal{A}_s, \mathcal{A}_g}^u$, $N(g, G_{\mathcal{A}_s, \mathcal{A}_g}^u)$ is the neighbors of g in $G_{\mathcal{A}_s, \mathcal{A}_g}^u$. When the goal vertices g are removed from G^u , the running buffer size is $\max(0, |N(g)| - |g|)$, i.e., the number of objects cleared away minus the number of available goal poses. Specifically, when $|N(g)| > |g|$, some objects are in buffers; when $|N(g)| < |g|$, some goal poses are available; when $|N(g)| = |g|$, the cleared objects happen to fill all the available goal poses. Given an induced graph $I(g)$, denote the goal vertices with no more than one neighbor in $I(g)$ as *free goals*. We make two observations. First, given an induced graph $I(g)$, we can always prioritize the removal of free goals without optimality loss. Second, multiple free goals may appear after a goal vertex is removed. For example, in the instance shown in Figure 2.1(a), when the vertex representing x_g^5 is removed, x_g^2 , x_g^3 , and x_g^4 become free goals and can be added to the linear ordering in an arbitrary order. Denote nodes without free goals in the induced graph as *key nodes*. In conclusion, the key nodes in the search tree may be sparse and enumerating all possible nodes with DP carries much overhead.

As such, instead of exploring the search tree layer by layer like DP, we maintain a sparse tree with a priority queue Q . While each node still represents an arrangement, each edge in the tree represents actions to clear out the next goal pose x_i^g . The corresponding child node of the edge represents the arrangement where x_i^g and free goals are removed from the induced graph. Similar to A*, we always pop out the key node with the smallest MRB in Q . We denote this priority queue-based search method PQS.

2.6.3 Depth-First Dynamic Programming

Both LRBM and URBM can be viewed as solving a series of decision problems, i.e., asking whether we can find a rearrangement plan with $k = 1, 2, \dots$ running buffers. As dynamic programming is applied to solve such decision problems, instead of performing the more standard breadth-first exploration of the search tree, we identified that a depth-first exploration is much more effective. We call this variation of dynamic programming DFDP, which is a fairly straightforward alteration of a standard DP procedure. The high-level structure of DFDP is described in Algorithm 3. It consumes a dependency graph and returns the minimum running buffer size for the corresponding instance. Essentially, DFDP fixes the running buffer size RB and checks whether there is a plan requiring no more than RB running buffers. As the search tree (see Subsection 2.6.1) is explored, depth-first exploration is used instead of breadth-first (Line 4).

Algorithm 3: Dynamic Programming with Depth-First Exploration

Input : G^ℓ : labeled dependency graph
Output: RB: the minimum number of running buffers

- 1 RB \leftarrow 0
- 2 **while** *not time exceeded* **do**
- 3 $T.\text{root} \leftarrow \emptyset$
- 4 $T \leftarrow \text{Depth-First-Search}(T, \emptyset, \text{RB}, G^\ell)$
- 5 **if** $\mathcal{O} \in T$ **then return** RB;
- 6 **else** RB += 1;
- 7 **end**

The details of the depth-first exploration are shown in Algorithm 4. Similar to DP, each node in the tree represents an object state indicating whether an object is at the start pose, the goal pose, or external buffers. And as described in Subsection 2.4.2, essential object states can be represented by the set of objects S that have picked up from start poses. If S is \mathcal{O} , then all the objects are at the goal poses and we find a path on the search tree from the start state to the goal state (Line 1). Given the set of objects away from the start poses S , we can get the sets of objects at start poses S_S , goal poses S_G , and external buffers S_B

(Line 2). Specifically, $S_S = \mathcal{O} \setminus S$, S_G are the objects in S that have no dependency in S_S , and S_B are the objects in S that have dependencies in S_S . We further explore child nodes of the current state by moving one object away from the start pose (Line 3). By checking the dependencies in $G^\ell(\mathcal{O}, A)$, we determine whether this object should be moved to buffers or its goal pose (Line 4). The transition from S to $S \sqcup \{o\}$ fails if the external buffers are overloaded or the child node has been explored (Line 5). Otherwise, we can add $S \sqcup \{o\}$ into the tree (Line 7) and explore the new node (Line 8). The algorithm returns a tree.

Algorithm 4: Depth-First-Search

Input : T : Search Tree; S : The set of objects away from start poses; RB : Running buffer size; $G^\ell(\mathcal{O}, A)$: labeled dependency graph

Output: T

- 1 **if** S is \mathcal{O} **then return** T ;
- 2 $S_S, S_G, S_B = \text{GetState}(S)$
- 3 **for** $o \in S_S$ **do**
- 4 $ToBuffer = \text{CollisionCheck}(S_S \setminus \{o\}, o, G^\ell)$
- 5 **if** ($ToBuffer$ and $\|S_B\| + 1 > RB$) or $(S \sqcup \{o\} \in T)$ **then return** T ;
- 6 **else**
- 7 $\text{AddNode}(T, S, S \sqcup \{o\})$
- 8 $T \leftarrow \text{Depth-First-Search}(T, S \sqcup \{o\}, RB, G^\ell)$
- 9 **if** $\mathcal{O} \in T$ **then return** T ;
- 10 **end**
- 11 **end**
- 12 **return** T

The intuition is that, when there are many rearrangement plans on the search tree that do not use more than k running buffers, a depth-first search will quickly find such a solution, whereas a standard DP must grow the full search tree before returning a feasible solution. A similar depth-first exploration heuristic is used in [69].

2.6.4 Minimizing Total Buffers Subject to MRB Constraints

We also construct a Mixed Integer Programming(MIP) model minimizing MRB or total buffers. Let binary variables $c_{i,j}$ represent the dependency graph $G_{\mathcal{A}_s, \mathcal{A}_g}^\ell$: $c_{i,j} = 1$ if and only if (i, j) is in the arc set of $G_{\mathcal{A}_s, \mathcal{A}_g}^\ell$. Let $y_{i,j} (1 \leq i < j \leq n)$ be the binary sequential

variables: $y_{i,j} = 1$ if and only if o_i moves out of the start pose before o_j . $y_{i,j}$ are used to represent the ordering of actions. We further introduce two sets of binary variables $g_{i,j}$ and $b_{i,j}$ ($1 \leq i, j \leq n$) to indicate object positions at each moment. $g_{i,j} = 1$ indicates that o_j has no dependency on other objects when moving o_i from the start pose. In other words, the goal pose of o_j is available at the moment. $b_{i,j} = 1$ indicates that o_j stays at the buffer after moving o_i away from the start pose. Finally, binary variables $B_i = 1$ if and only if o_i is moved to a buffer at some point. The objective function consists of two terms: the total buffer term and running buffer term. The total buffer term, scaled by α , counts the number of objects that need buffer locations. MRB is represented with an integer variable K and scaled by β . To minimize total buffers subject to MRB constraints, we set $\alpha = 1, \beta = n$. The objective function is adaptable to different demands on rearrangement plans. Specifically, when $\alpha = 0, \beta > 0$, the MIP model minimizes MRB. When $\alpha > 0, \beta = 0$, the MIP model minimizes total buffers, i.e. total actions in the rearrangement plan. When $\alpha/\beta > n - 1$, the MIP model first minimizes total buffers, and then minimizes running buffers. When $\beta/\alpha > n - 1$, the MIP model first minimizes running buffers, and then minimizes total buffers.

In the MIP model, Constraints Equation 2.2 imply the rules for sequential variables to make sure a valid ordering of indices $1, \dots, n$ can be encoded from $y_{i,j}$. Constraints Equation 2.3 imply that $B_j = 1$ if o_j has been to buffers in the plan. Constraints Equation 2.4 imply that MRB K is lower bounded by the maximum number of objects concurrently placed in buffers. With Constraints Equation 2.5 and Equation 2.6, $g_{i,j} = 0$ if and only if o_j depends on an object o_k which is still at the start pose when o_i is moved. With Constraints Equation 2.7-Equation 2.9, $b_{i,j} = 1$ if and only if o_j is moved before o_i and the goal pose is still unavailable when o_i is moved from the start pose.

$$\arg \min \alpha \left[\sum_{i=1}^n B_i \right] + \beta K \quad (2.1)$$

$$0 \leq y_{i,j} + y_{j,k} - y_{i,k} \leq 1 \quad \forall 1 \leq i < j < k \leq n \quad (2.2)$$

$$B_j \geq \sum_{1 \leq i \leq n} \frac{b_{i,j}}{n} \quad \forall 1 \leq j \leq n \quad (2.3)$$

$$K \geq \sum_{1 \leq j \leq n} b_{i,j} \quad \forall 1 \leq i \leq n \quad (2.4)$$

$$\sum_{1 \leq k < i} \frac{c_{j,k}(1 - y_{k,i})}{n} + \sum_{i < k \leq n} \frac{c_{j,k}y_{i,k}}{n} \leq 1 - g_{i,j} \quad (2.5)$$

$$\forall 1 \leq i, j \leq n$$

$$1 - g_{i,j} \leq \sum_{1 \leq k < i} c_{j,k}(1 - y_{k,i}) + \sum_{i < k \leq n} c_{j,k}y_{i,k} \quad (2.6)$$

$$\forall 1 \leq i, j \leq n$$

$$\frac{g_{i,j} + y_{i,j}}{2} \leq 1 - b_{i,j} \leq g_{i,j} + y_{i,j} \quad (2.7)$$

$$\forall 1 \leq i < j \leq n$$

$$\frac{g_{j,i} + (1 - y_{i,j})}{2} \leq 1 - b_{j,i} \leq g_{j,i} + (1 - y_{i,j}) \quad (2.8)$$

$$\forall 1 \leq i < j \leq n$$

$$b_{i,i} = 1 - g_{i,i} \quad (2.9)$$

2.7 Experimental Results

Our evaluation focuses on uniform cylinders, given their prevalence in practical applications. For simulation studies, instances with different object densities are created, as measured by *density level* $\rho := n\pi r^2/(h * w)$, where n is the number of objects and r is the base radius. h and w are the height and width of the workspace. In other words, ρ is the proportion of the tabletop surface occupied by objects.

The evaluation is conducted on both random object placements and manually constructed difficult setups (e.g., dependency grids with $MRB = \Omega(\sqrt{n})$). For generating test cases with high ρ value, we invented a physic engine (we used Gazebo [70]) based approach for doing so. Within a rectangular box, we sample placements of cylinders at lower

density and then also sample locations for some smaller “filler” objects (see Figure 2.12, left). From here, one side of the box is pushed to reach a high-density setting (Figure 2.12, right), which is very difficult to generate via random sampling. By controlling the ratio of the two types of objects, different density levels can be readily obtained. Figure 2.13 shows three random object placements for $\rho = 0.2, 0.4$ and 0.6 .

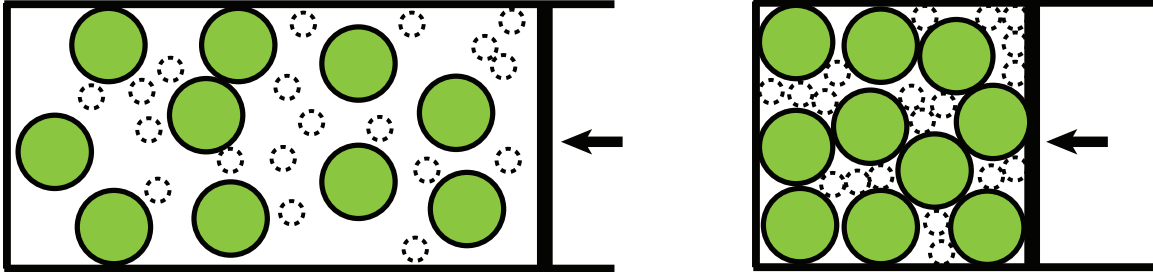


Figure 2.12: Generating dense instances using a physics-engine-based simulator through compression of the left scene to the right scene.

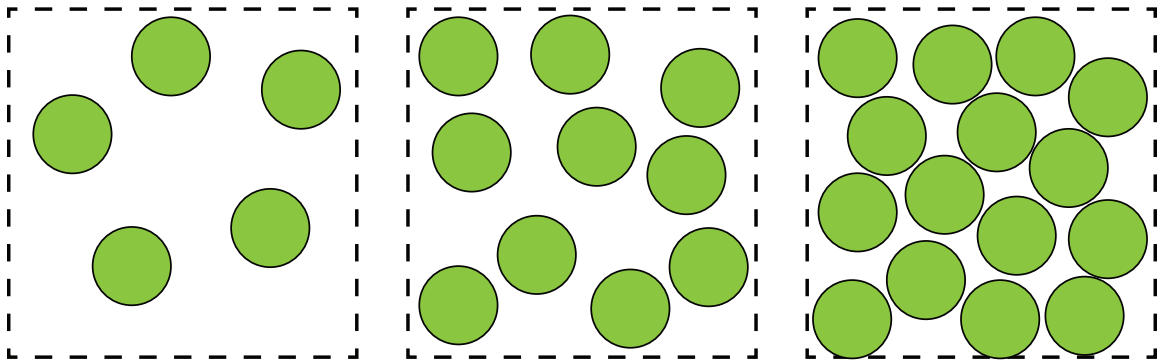


Figure 2.13: Unlabeled arrangements with $\rho = 0.2, 0.4, 0.6$ respectively.

From two randomly generated object placements with the same ρ and n values, a URBM instance can be readily created by superimposing one over the other. LRBM instances can be generated from URBM instances by assigning each object a random label in $[n]$ for both start and goal configurations.

The proposed algorithms are implemented in Python and all experiments are executed on an Intel[®] Xeon[®] CPU at 3.00GHz. For solving MIP, Gurobi 9.16.0 [71] is used.

Table 2.2: Evaluated methods for TORE.

Problems	Methods
LRBM	DFDP, DP, TB_{FVS} , TB_{MRB}
URBM	DFDP, PQS

2.7.1 LRBM over Random Instances

In Figure 2.14, we compare the effectiveness of DP and DFDP, in terms of computation time and success rate, for different densities. Each data point is the average of 30 test cases minus the unfinished ones, if any, subject to a time limit of 300 seconds per test case. For LRBM, we are able to push to $\rho = 0.4$, which is fairly dense. The results clearly demonstrate that DFDP significantly outperforms the baseline DP. Based on the evaluation, both methods can be used to tackle practical-sized problems (e.g., tens of objects), with DFDP demonstrating superior efficiency and robustness.

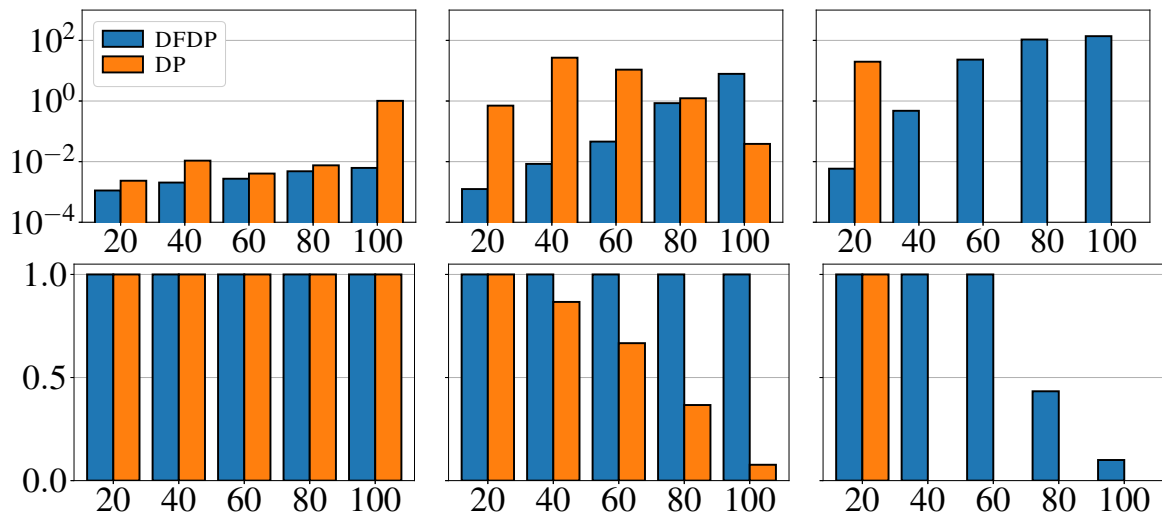


Figure 2.14: Performance of DFDP and DP over LRBM. The top row shows the average computation time (s) and the bottom row the success rate, for density levels $\rho = 0.2, 0.3, 0.4$, from left to right. The x -axis denotes the number of objects involved in a test case.

The actual MRB sizes for the same test cases from Figure 2.14 are shown in Figure 2.15 on the left. We observe that MRB is rarely very large even for fairly large LRBM instances. The size of MRB appears correlated to the size of the largest connected component of the

underlying dependency graph, shown in Figure 2.15 on the right.

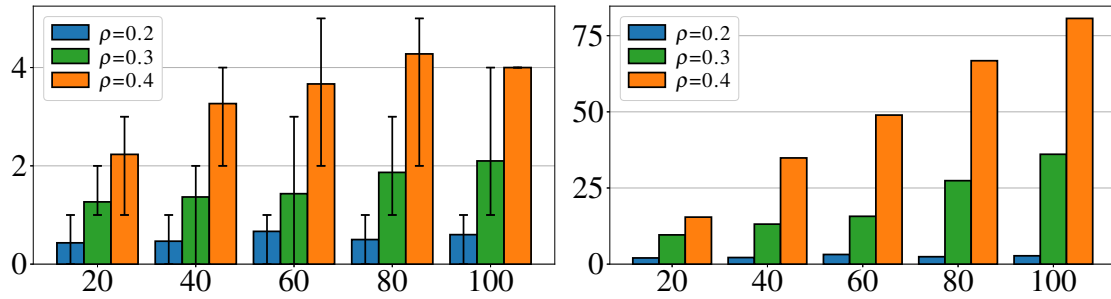


Figure 2.15: For LRBM instances with $\rho = 0.2-0.4$ and $n = 20-100$, the left figure shows average MRB size and range. The right figure shows the size of the largest connected component of the dependency graph.

For LRBM with $\rho = 0.3$ and n up to 50, we computed the MFVS sizes using TB_{FVS} (which does not scale to higher ρ and n) and compared that with the MRB sizes, as shown in Figure 2.16 (a). We observe that the MFVS is about twice as large as MRB, suggesting that MRB provides more reliable information for estimating the design parameters of pick-n-place systems. For these instances, we also computed the total number of buffers needed subject to the MRB constraint using TB_{MRB} . Out of about 150 instances, only 1 showed a difference as compared with MFVS (therefore, this information is not shown in the figure). In Figure 2.16 (b), we provided a computation time comparison between TB_{FVS} and TB_{MRB} , showing that TB_{MRB} is practical, if it is desirable to minimize the total buffers after guaranteeing the minimum number of running buffers.

Considering our theoretical findings and the evaluation results, an important conclusion can be drawn here is that MRB is effectively a small constant for random instances, even when the instances are very large. Also, minimizing the total number of buffers used subject to MRB constraint can be done quickly for practical-sized problems.

2.7.2 URBM over Random Instances

For URBM, we carry out a similar performance evaluation as we have done for LRBM. Here, PQS and DFDP are compared. For each combination of ρ and n , 100 random test cases

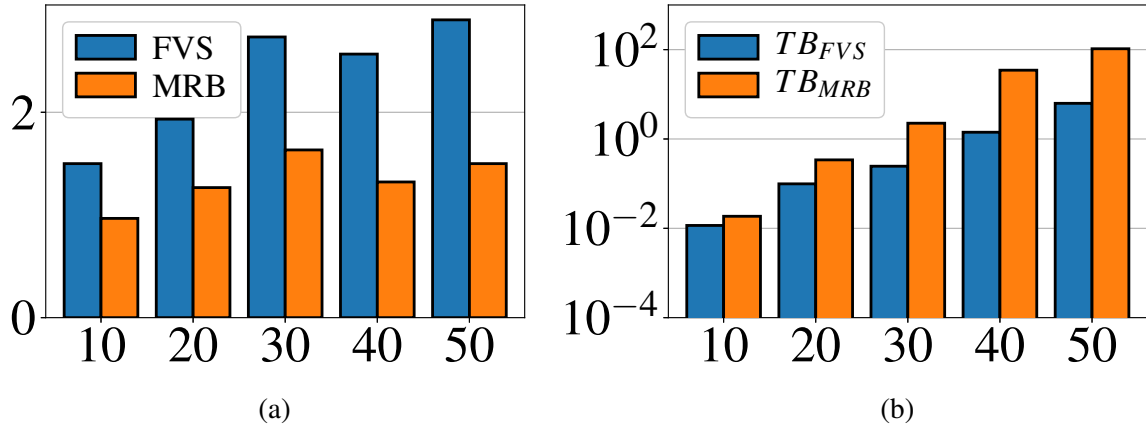


Figure 2.16: (a) Comparison between size of MRB and MFVS. (b) Computation time comparison between TB_{FVS} and TB_{MRB} .

are evaluated. Notably, we can reach $\rho = 0.6$ with relative ease. From Figure 2.17, we observe that DFDP is more efficient than PQS, especially for large-scale dense settings. In terms of the MRB size, all instances tested have an average MRB size between 0 and 0.7, which is fairly small (Figure 2.18). Interestingly, we witness a decrease of MRB as the number of objects increases, which could be due to the lessening “border effect” of the larger instances. That is, for instances with fewer objects, the bounding square puts more restriction on the placement of the objects inside. For larger instances, such restricting effects become smaller. We mention that the total number of buffers for random URBM cases subject to MRB constraints are generally very small.

2.7.3 Manually Constructed Difficult Cases of TORE

In the random scenario, the running buffer size is limited. In particular, for LRBM, the dependency graph tends to consist of multiple strongly connected components that can be dealt with independently. We further show the performance of DFDP on the instances with $MRB = \Theta(\sqrt{n})$. We evaluate three kinds of instances: (1) UG: m^2 -object URBM instances whose G_{A_s, A_g}^u are dependency grid $\mathcal{D}(m, 2m)$ (e.g., Figure 2.9); (2) LG: m^2 -object LRBM instances whose start and goal arrangements are the same as the instances in (1). (3) LC: m^2 -object LRBM instances with objects placed on a cycle (Figure 2.10). The computation

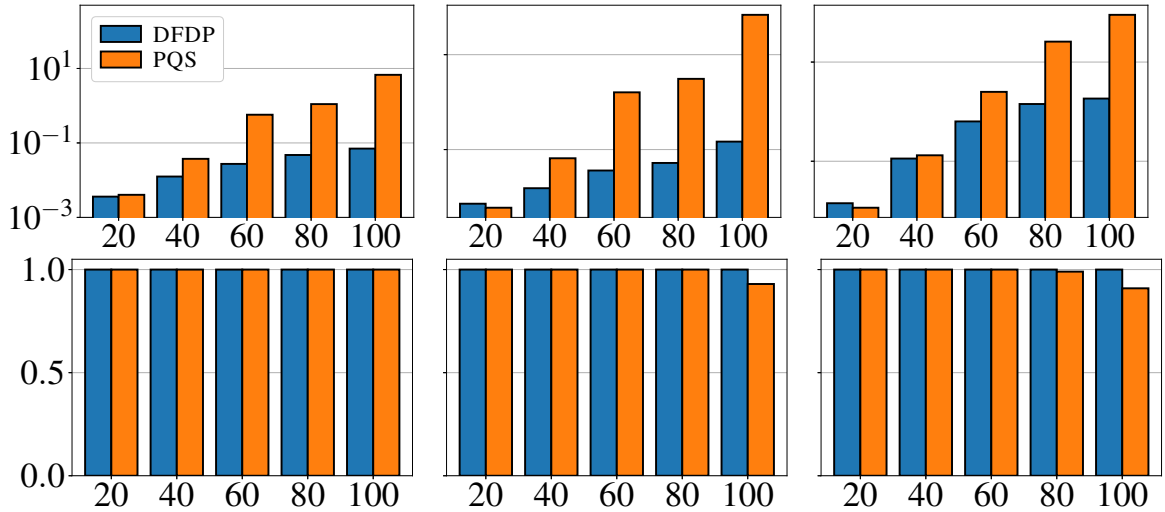


Figure 2.17: Performance of DFDP and PQS over URBM. The top row shows the average computation time and the bottom row shows the success rate, for density levels $\rho = 0.4, 0.5, 0.6$, from left to right.

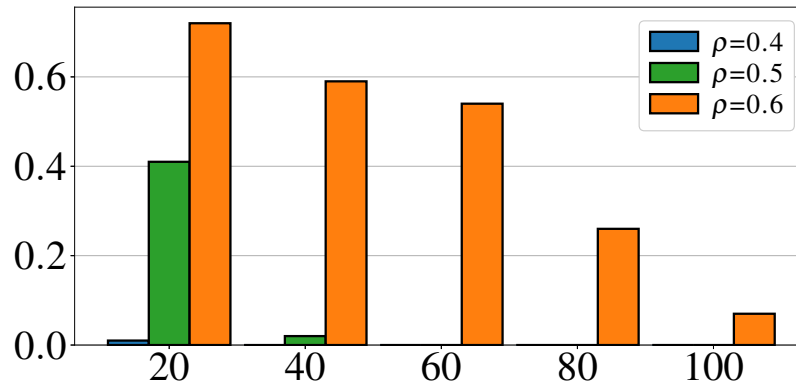


Figure 2.18: Average MRB size for URBM instances with $\rho = 0.4 - 0.6$ and $n = 20 - 100$. For $\rho = 0.4$ and 0.5 , the MRB sizes are near zero as the number of objects goes beyond 20.

time and the corresponding MRB are shown in Figure 2.19. For LG instances, the labels are randomly assigned. We try 30 test cases and then plot out the average. We observe that the MRB is much larger for these handcrafted instances as compared with random instances with similar density and number of objects.

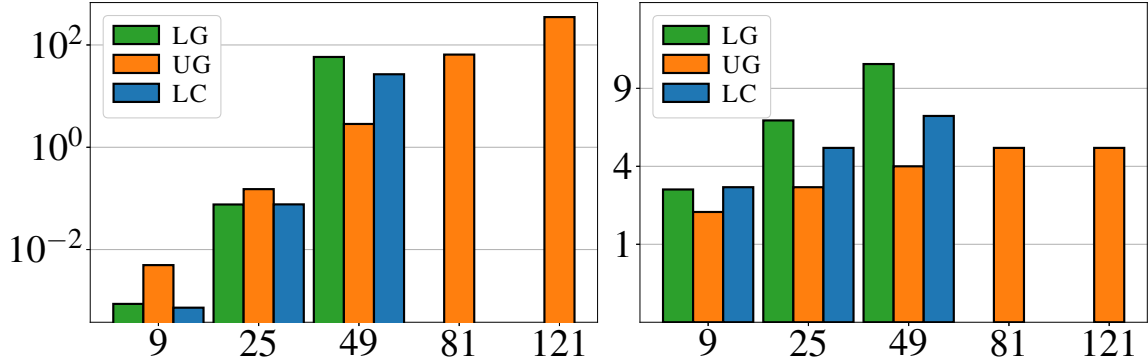


Figure 2.19: For handcrafted cases and different numbers of objects, the left figure shows the computation time by DFDP and the right figure the resulting MRB size.

2.8 Physical Experiments

In this section, we demonstrate that the plans computed by proposed algorithms can be readily executed on real robots in a complete vision-planning-control pipeline. We first introduce the hardware setup and the pipeline during the execution of the rearrangement plans. After that, we present experimental results based on the execution of computed rearrangement plans.

2.8.1 Hardware Setup

In our hardware setup (Figure 2.20), we use a UR-5e robot arm with an OnRobot VGC 10 vacuum gripper to execute pick-n-places. An Intel RealSense D435 RGB-D camera is set up above the environment to provide an overview of the entire workspace. The camera calibration is done with four 2D fiducial markers at the corners of the environment using a C++ cross-platform software library Chilitags [72]. An example instance of our experiment is shown in Figure 2.21¹. The right side of the pad works as an external space for buffer placements. For the cylindrical objects, pose estimation is conducted with the aid of Chilitags. Demonstrations are available online.

The rearrangement pipeline is shown in Algorithm 5. The system first estimates the

¹More demonstrations are available in a [video](#) online.

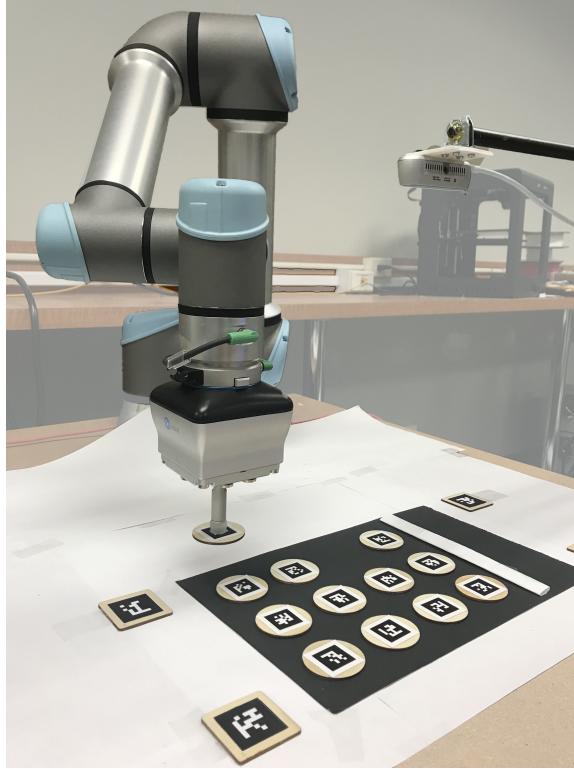


Figure 2.20: Our hardware setup for executing rearrangement plans computed by proposed algorithms.

current poses of workspace objects \mathcal{A}_c (Line 1). Given the current arrangement \mathcal{A}_c and goal arrangement \mathcal{A}_g , the rearrangement solver computes a rearrangement plan π (Line 2). Each action in π consists of three components: manipulating object o , current pose p_c , and target pose p_t (Line 3). To improve the accuracy of pick-n-places, we update the grasping pose before each grasp (Lines 4-5).

2.8.2 Experimental Validation

We conduct hardware experiments on TORE, comparing the execution time of RBM plans and TBM plans. With the same notations as those in Section 2.7, RBM plans minimize running buffer size and TBM plans minimize total buffer size. In TORE, minimizing the total buffer size is equivalent to minimizing the number of total actions. We tried 10 instances with 12 cylindrical objects. The results are shown in Table 2.3. While minimizing running buffer size, RBM plans are only 5% longer than TBM plans on average.

Algorithm 5: Rearrangement Pipeline

Input : \mathcal{A}_g : goal arrangement

- 1 $\mathcal{A}_c \leftarrow \text{PoseEstimation}()$
- 2 $\pi \leftarrow \text{RearrangementSolver}(\mathcal{A}_c, \mathcal{A}_g)$
- 3 **for** (o, p_c, p_t) **in** π **do**
- 4 $p_c \leftarrow \text{UpdatePose}(o)$
- 5 $\text{ExecuteAction}((o, p_c, p_t))$
- 6 **end**

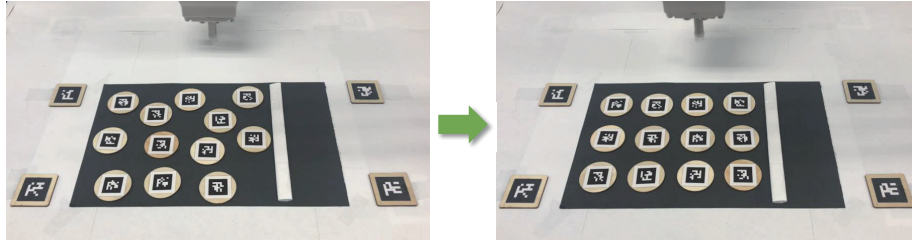


Figure 2.21: An example instance of our experiment. The right side of the pad works as an external space for buffer placements.

Table 2.3: Comparison between RBM plans and TBM plans in execution time and the number of actions.

instance	RBM		TBM	
	execution time (secs)	# actions	execution time (secs)	# actions
1	211.35	15	194.52	14
2	197.76	14	197.66	14
3	184.49	13	185.82	13
4	201.32	14	205.96	14
5	227.03	16	195.44	14
6	193.84	14	192.61	14
7	216.49	15	198.90	14
8	250.13	17	211.15	15
9	176.75	13	179.83	13
10	179.07	12	160.96	12
Average	203.82	14.3	192.28	13.7

2.9 Summary

In this work, we investigate the problem of minimizing the number of running buffers (MRB) for solving labeled and unlabeled tabletop rearrangement problems with overhead grasps (TORO), which translates to finding a best linear ordering of vertices of the associated underlying dependency graph. For TORO, MRB is an important quantity to under-

stand as it determines the problem's feasibility if only external buffers are to be used, which is the case in some real-world applications [1]. Despite the provably high computational complexity that is involved, we provide effective dynamic programming-based algorithms capable of quickly computing MRB for large and dense labeled/unlabeled TORO instances. In addition, we also provide methods for minimizing the total number of buffers subject to MRB constraints. Whereas we prove that MRB can grow unbounded for both labeled and unlabeled settings for special cases for uniform cylinders, empirical evaluations suggest that real-world random TORO instances are likely to have much smaller MRB values.

We conclude by leaving the readers with some interesting open problems. As for bounds, the lower and upper bounds of MRB for LRBM for uniform cylinders do not yet agree; can the bound gap be narrowed further? Objects may have different sizes. An interesting question here is if we can move a large object to buffer or a small object to buffer, which is more beneficial? Moving larger objects are more challenging but we may need to do this fewer times.

CHAPTER 3

TRLB: TABLETOP REARRANGEMENT WITH LAZY BUFFER POSE VERIFICATION

3.1 Motivations

This chapter investigates TORO with internal buffers (TORI). While solving TORE only deals with *inherent* constraints defined by the start and goal poses, some objects in TORI may be temporarily displaced inside the workspace and induce further *acquired* constraints. For instance, to solve the problem in Figure 1.1 with external buffers, we can move the Pepsi can to an external buffer to break the cycle, move the Coke first and then Fanta to their goal locations, and finally, bring back the Pepsi can into the workspace. In TORI, we must find a temporary location for the Pepsi can in the workspace. If the buffer location overlaps with the goal of the Coke can (or the Fanta can), then the Coke can (or the Fanta can) depends on the Pepsi can again. To avoid these acquired constraints, the buffer location needs to avoid the goals of Coke and Fanta.

Due to acquired constraints arising from internal buffer selection, TORI is more challenging than TORE. Intuitively, selecting buffers inside the workspace (TORI) is much more difficult and constrained than using buffers outside the workspace (TORE) to store displaced objects. Since TORE has been shown to be computationally intractable [1], and is equivalent to a special case of TORI where the workspace is large enough that collision-free buffer locations are guaranteed, TORI is also NP-hard. Additionally, in TORI, it may be challenging to allocate valid buffer locations so it is necessary to limit the running buffer size. With this observation, TORI solutions are computed based on methods for TORE.

For TRLB, we propose Tabletop Rearrangement with Lazy Buffers (TRLB), an effective framework for solving TORI based on TORE algorithms. We first describe a re-

arrangement solver with lazy buffer allocation, where buffer allocation is delayed after DFDP computes a “rough” schedule of object movements. Second, we design a preprocessing routine based on the TORE planner for the unlabeled variant in order for further speedups. Third, the TRLB framework recovers from buffer allocation failures to enhance scalability to larger and more cluttered instances. Finally, TRLB is extended to consider object heterogeneity (e.g., object size and shape).

3.2 Related Work

Rearrangement Approaches: Object rearrangement is a topic of interest within Task and Motion Planning (TAMP). Typical definitions in this domain [73, 69, 74, 75] involve arranging multiple objects to specific goals. Certain variations such as NAMO (Navigation among Movable Obstacles) [6, 76, 77], and retrieval problems [78, 32], focus on clearing out a path for a target object while identifying objects that need to be relocated. Rearrangement may be approached either via simple but inaccurate non-prehensile actions, e.g., pushes [73, 79, 80], or more purposeful prehensile actions, such as grasps [9, 47, 75, 81, 82, 83]. Focusing on the combinatorial challenges, some planners use external space for temporary object storage [1, 74, 31, 32], while others exploit problem linearity to simplify search [84, 6, 77, 85]. By linking rearrangement to established graph-based problems, efficient algorithms have been obtained for various tasks and objectives [1, 74, 31]. This chapter uses a plan generated given access to external buffer locations as a “primitive plan”, which then guides buffer allocation inside the workspace.

Dependency Graph: We represent the combinatorial constraints of such problems via a dependency graph, which was first applied to general multi-body planning problems [46] and then rearrangement [9, 47]. Choosing different manipulation sequences gives rise to multiple dependency graphs for the same problem instance, which limits scalability. Prior work [1] has applied full dependency graphs to address TORO, showing that the challenge embeds the NP-hard Feedback Vertex Set (FVS) and the Traveling Salesperson (TSP) prob-

lems. More recently, some of the authors [74] examined an optimization objective, *running buffers*, which is the size of the external space needed for rearrangement, and also examined an unlabeled setting. Similar structures are also used in other problems, such as packing [48]. Deep neural networks have been also applied to detect the embedded dependency graph of objects in a cluttered space to determine the ordering of object retrieval [78].

Buffer Identification: In rearrangement, collision-free locations are needed for obstacle displacements. Some previous efforts predetermine buffer candidates and place obstacles to accessible candidate locations when necessary [69, 86]. Others decouple the problem into successive subproblems [47, 69]. Intuitively speaking, a valid buffer location needs to avoid other objects at their current poses. Backtracking search further constrains object displacements given paths of future manipulation actions [76, 77]. Nevertheless, these methods are computationally expensive since they deal with inherent and acquired constraints at the same time. To reduce the associated cost, a lazy strategy can be applied [87, 88, 89], which delays path/configuration collision checking. A similar idea is proposed here. Feasible object locations are obtained with the aid of a “rough schedule” of object manipulation actions, which is computed given only the inherent constraints. By decoupling inherent and acquired constraints, the proposed method computes high-quality solutions efficiently.

3.3 Tabletop Rearrangement with Internal Buffer Space (TORI)

3.3.1 Problem Statement

Consider a 2D bounded workspace $\mathcal{W} \subset \mathbb{R}^2$ containing a set of n objects $\mathcal{O} = \{o_1, \dots, o_n\}$. Each object is assumed to be an upright *generalized cylinder*. A *feasible arrangement* $\mathcal{A} = \{p_1, \dots, p_n\}$, $p_i = \{x_i, y_i, \theta_i\} \in SE(2)$ is a set of poses for objects in \mathcal{O} , such that (1) each object’s footprint is contained in \mathcal{W} , and (2) no two objects collide.

Consider (overhand) pick-n-place actions to move objects one by one. A pick-n-place action, represented as an ordered pair (o, p) , grasps an object o at its current pose and lifts

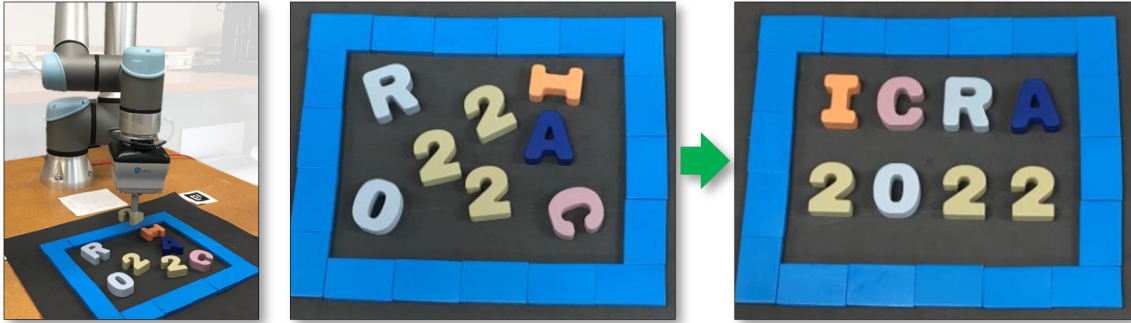


Figure 3.1: A robot arm rearranges word patterns with overhand grasps, minimizing the number of pick-n-place actions. The letters cannot go out of the bounding box and cannot overlap on the tabletop.

it above all other objects. It then moves it horizontally, and places it at the target pose p within \mathcal{W} . An action is collision-free iff both the current and resulting arrangements are feasible. A plan P from a feasible \mathcal{A}_s to a feasible \mathcal{A}_g is a sequence of collision-free pick-n-place actions transforming \mathcal{A}_s into \mathcal{A}_g . We want to compute feasible plans that minimize the number of pick-n-place actions, which leads to increased system throughput, i.e.,

Problem 2 (TORO w/ Internal Buffers (TORI)). *Given feasible arrangements $\mathcal{A}_s = \{p_1^s, \dots, p_n^s\}$ and $\mathcal{A}_g = \{p_1^g, \dots, p_n^g\}$, find a feasible plan P sequentially moving objects from \mathcal{A}_s to \mathcal{A}_g , which minimizes the number of actions.*

3.4 Algorithmic Solutions

We first describes a rearrangement solver with lazy buffer allocation (Subsection 3.4.1), where buffer allocation is delayed after getting a “rough” schedule of object movements. To enhance scalability to larger and more cluttered instances, the TRLB framework (Subsection 3.4.2) recovers from buffer allocation failures. Finally, a preprocessing routine helps with further speedups (Subsection 3.4.3).

3.4.1 Lazy Buffer Pose Verification

When an object stays at a buffer, it should avoid blocking the upcoming manipulation actions of other objects. Otherwise, either the object in the buffer or the manipulating object

has to yield, which increases the number of necessary actions. In other words, we need to carefully choose acquired constraints. If we know the schedule of other objects in advance, a buffer can be selected to minimize unnecessary obstructions. This observation motivates us to “lazily” allocate buffers by ignoring initially acquired constraints and solve the rearrangement problem in two steps: First, compute a *primitive plan*, which is an incomplete schedule ignoring acquired constraints; second, given the incomplete schedule as a reference, generate buffers to optimize the selection of acquired constraints.

3.4.1.1 Primitive Plan

To compute a *primitive plan*, we assume enough free space is available so that no acquired constraints will be created. This transforms the problem into a TORE problem, where each object is displaced at most once before it moves to the goal pose. Then, an object $o_i \in \mathcal{O}$ can have three *primitive* actions:

1. $(o_i, s \rightarrow g)$: moving from p_i^s to p_i^g ;
2. $(o_i, s \rightarrow b)$: moving from p_i^s to a buffer;
3. $(o_i, b \rightarrow g)$: moving from a buffer to p_i^g .

A primitive plan is a sequence of primitive actions; computing such a plan is similar to finding a linear vertex ordering [63, 62] of the dependency graph. We use dynamic programming based methods in Chapter 2 to achieve this, which minimizes the number of total buffers or running buffers.

3.4.1.2 Buffer Allocation

Free space inside the workspace \mathcal{W} is scarce in cluttered spaces (e.g., Figure 3.6) and acquired constraints must be dealt with through the careful allocation of buffers inside \mathcal{W} . We apply a greedy strategy to find feasible buffers based on a primitive plan (Algorithm 6). The general idea is to incrementally add constraints on the buffers until we find feasible

buffers for the whole primitive plan or terminate at a step where there are no feasible buffers for the primitive plan. In Algorithm 6, $\mathcal{O}_s, \mathcal{O}_g, \mathcal{O}_b$ are the sets of objects currently at start poses, goal poses and buffers respectively.

Algorithm 6: Buffer Allocation

Input : π : a primitive plan; $\mathcal{A}_s = \{p_1^s, \dots, p_n^s\}$: start arrangement; $\mathcal{A}_g = \{p_1^g, \dots, p_n^g\}$: goal arrangement

Output: B : buffers; TerminatingStep: the action step where buffer generation fails, ∞ if Success.

```

1  $\mathcal{O}_s \leftarrow \mathcal{O}; \mathcal{O}_g, \mathcal{O}_b \leftarrow \emptyset; B \leftarrow \text{RandomPoses}(\mathcal{O})$ 
2 for  $(o_i, m) \in \pi$  do
3   if  $m$  is  $s \rightarrow b$  then
4      $\mathcal{O}_b.\text{add}(o_i)$ 
5      $\text{Constraints}[o_i] \leftarrow \text{GetPoses}(\mathcal{O}_s \cup \mathcal{O}_g - \{o_i\})$ 
6   end
7   else if  $m$  is  $b \rightarrow g$  then
8     for  $o \in \mathcal{O}_b \setminus \{o_i\}$  do  $\text{Constraints}[o].\text{add}(p_i^g)$ ;
9   end
10  else
11    for  $o \in \mathcal{O}_b$  do  $\text{Constraints}[o].\text{add}(p_i^g)$ ;
12  end
13   $\text{Success}, B' \leftarrow \text{BufferGeneration}(\mathcal{O}_b, \text{Constraints}, B)$ 
14  if Success then
15     $B \leftarrow B'$ 
16     $\mathcal{O}_s, \mathcal{O}_g, \mathcal{O}_b \leftarrow \text{UpdateState}(\mathcal{O}_s, \mathcal{O}_g, \mathcal{O}_b)$ 
17  end
18  else return  $B, \pi.\text{index}(\text{action})$ ;
19 end
20 return  $B, \infty$ 

```

We start with \mathcal{A}_s where all the objects are at start poses and the buffers are initialized at random poses (Line 1). Each action in π indicates an object o_i that is manipulated and the action m performed (Line 2). If o_i is moved to a buffer (Line 3), then we add it into \mathcal{O}_b (Line 4). The current poses of other objects in $\mathcal{O}_s \cup \mathcal{O}_g$ are seen as fixed obstacles for o_i (Line 5). If o_i is leaving the buffer (Line 6), then other objects in \mathcal{O}_b should avoid the goal pose p_i^g of o_i (Line 7). If o_i is moving directly from p_i^s to p_i^g (Line 8, the “else” corresponds to m being $s \rightarrow g$, e.g., directly go from start to goal), then all buffers for objects in the current \mathcal{O}_b need to avoid p_i^g (Line 9). After setting up acquired constraints,

we generate new buffers for objects in O_b to satisfy these constraints by either sampling or solving an optimization problem (Line 10). Old buffers in B satisfying new constraints will be directly adopted. If feasible buffers are found (Line 11), then buffers and object states will be updated (Line 12-13). Otherwise, we return the feasible buffers computed and record the terminating step of the algorithm (Line 14). In the case of a failure, we provide a TRLB framework to recover, which is presented in Subsection 3.4.2.

Figure 3.2 illustrates the buffer allocation process via an example. The green, cyan, and transparent discs represent the current poses, goal poses and allocated buffers respectively. When we move o_1 to a buffer B_1 (Figure 3.2(b)), it only needs to avoid collision with p_2^s and p_3^s . But as we move o_3 to a buffer, B_1 needs to avoid o_3 's buffer B_3 as well. To satisfy the added constraint, B_1 will be reallocated. Since the new buffers B_1 and B_3 (Figure 3.2(c)) satisfy the constraints added in the following steps, they need not to be relocated. Note that the buffer originally selected for o_1 but then replaced will not appear in the resulting plan, i.e., o_1 will move directly to the new buffer (Figure 3.2(c)-(f)). Algorithm 6 works with one strongly connected component of the dependency graph at a time, treating objects in other components as fixed obstacles.

Once the feasible buffers are found, all the primitive actions can be transformed into feasible pick-n-place actions inside the workspace. And therefore, the primitive plan can be transformed into a rearrangement plan moving objects from \mathcal{A}_s to \mathcal{A}_g . The function `BufferGeneration` is implemented by either sampling or solving an optimization problem, both of which are discussed below.

Sampling Given the object poses that buffers need to avoid so far, feasible buffers can be generated by sampling poses inside the free space. When objects stay in buffers at the same time, we sample buffers one by one and previously sampled buffers will be seen as obstacles for latter ones.

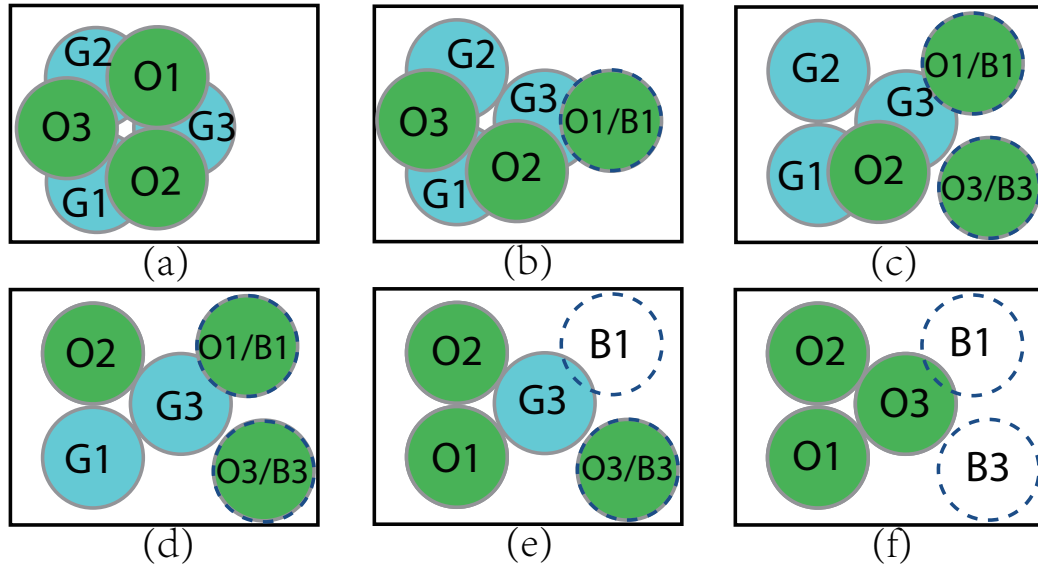


Figure 3.2: A working example with three objects defined in (a). The primitive plan is $[(o_1, s \rightarrow b), (o_3, s \rightarrow b), (o_2, s \rightarrow g), (o_1, b \rightarrow g), (o_3, b \rightarrow g)]$. Figures (b)-(f) show the steps of Alg. 1 after each action. The transparent discs with dashed line boundaries (B_i) represent the buffers satisfying constraints up to each step. For each object o_i , the green (O_i) and cyan (G_i) discs represent the current and goal poses respectively.

Optimization For cylindrical objects o_i at (x_i, y_i) with radius r_i , and o_j at (x_j, y_j) with radius r_j , they are collision-free when $(x_i - x_j)^2 + (y_i - y_j)^2 \geq (r_i + r_j)^2$ holds. Therefore, the collision constraints obtained in Algorithm 6 can be transformed into quadratic inequalities. By further restricting the range of buffer centroids to assure they are in the workspace, the buffer allocation problem can be transformed into a quadratic programming problem with no objective function. For objects with general shapes, collision avoidance cannot be presented by inequalities of object centroids. We can construct the optimization problem with ϕ functions of the objects [90] and solve the problem with gradients.

3.4.2 Failure Recovery with Bi-Directional Search

The TRLB framework builds on the insight that a new TORI instance is generated when lazy buffer allocation fails. The new instance has the same goal \mathcal{A}_g as the original one but some progress has been made in solving the TORI task. There are two straightforward implementations of TRLB: forward search and bidirectional search. In the first case, by

accepting partial solutions, a rearrangement plan can be computed by developing a search tree T rooted at \mathcal{A}_s . In the search tree T , nodes are feasible arrangements and edges are partial plans containing a sequence of collision-free actions. When buffer allocation fails, we add the resulting arrangement into the tree and resume the rearrangement task from a random node in T . This randomness and the randomness in primitive plan computation and buffer allocation allows TRLB to recover from failures.

Algorithm 7: TRLB with Bidirectional Search

Input : $\mathcal{A}_s, \mathcal{A}_g, max.time$
Output: Search trees: T_1, T_2

- 1 $T_1.root, T_2.root \leftarrow \mathcal{A}_s, \mathcal{A}_g$
- 2 **while** *not exceeding max.time* **do**
- 3 $\mathcal{A}_{rand} \leftarrow \text{RandomNode}(T_1)$
- 4 $\mathcal{A}_{new1} \leftarrow \text{LazyBufferAllocation}(\mathcal{A}_{rand}, T_2.root)$
- 5 $T_1.add(\mathcal{A}_{new1})$
- 6 **if** \mathcal{A}_{new1} *is* $T_2.root$ **then return** T_1, T_2 ;
- 7 $\mathcal{A}_{near} \leftarrow \text{NearestNode}(\mathcal{A}_{new1}, T_2)$
- 8 $\mathcal{A}_{new2} \leftarrow \text{LazyBufferAllocation}(\mathcal{A}_{near}, \mathcal{A}_{new1})$
- 9 $T_2.add(\mathcal{A}_{new2})$
- 10 **if** \mathcal{A}_{new2} *is* \mathcal{A}_{new1} **then return** T_1, T_2 ;
- 11 $T_1, T_2 \leftarrow T_2, T_1$
- 12 **end**

In bidirectional search, two search trees rooted at \mathcal{A}_s and \mathcal{A}_g are developed. This more involved procedure is shown in Algorithm 7, which computes two search trees that connect \mathcal{A}_s and \mathcal{A}_g . In Line 1, the trees are initialized. For each iteration, we first rearrange between a random node \mathcal{A}_{rand} on T_1 to the root node of T_2 (Line 3-5). The function `LazyBufferAllocation` refers to the overall algorithm developed in Subsection 3.4.1. A found path yields a feasible plan for TORI (Line 6). Otherwise, we rearrange between the new arrangement \mathcal{A}_{new1} and its nearest neighbor in T_2 (Line 7-9). This paper defines the distance between arrangement nodes as the number of objects at different poses. If a path is found, then we find a feasible rearrangement plan for TORI (Line 10). Otherwise, we switch the trees and attempt rearrangement from the opposite side (Line 11).

3.4.3 Preprocessing for Rearrangement in Confined Workspace

In dense environments, allocating buffers is hard, motivating minimizing the number of running buffers (mentioned in Chapter 2), which is generally low even in high density settings if we treat objects as *unlabeled*. Based on this, for each component of the dependency graph that is not a single vertex/cycle, we reduce the running buffer size to at most 1 by first solving an *unlabeled* instance (also mentioned in Chapter 2). After preprocessing, we obtain a TORI requiring at most one running buffer. Figure 3.3 shows an example of preprocessing. o_1, o_2 and o_3 form a complete graph, where at least two objects need to be placed at buffers simultaneously. We conduct preprocessing of the three-vertex component by moving o_2 to a buffer position, o_1 to p_3^g and o_3 to p_2^g . o_2 will not move to p_1^g since it does not occupy other goal poses. The preprocessing step needs one buffer and the resulting rearrangement problem is monotone.

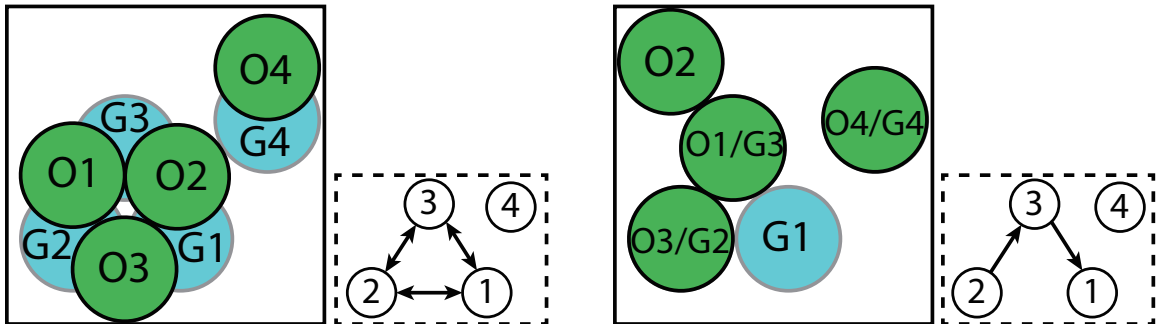


Figure 3.3: A four-object example of preprocessing. The green and cyan discs represent current and goal arrangements respectively. Before preprocessing (left), two buffers need to be allocated synchronously. After preprocessing (right), the problem becomes monotone.

3.5 Heterogeneous TORI

3.5.1 Motivation

Latest algorithmic research on TORI is mainly limited to solving instances with mostly homogeneous objects [1, 81, 91, 92]. The assumption of homogeneous objects leads to a relatively simple model where each object manipulation action has the same or very

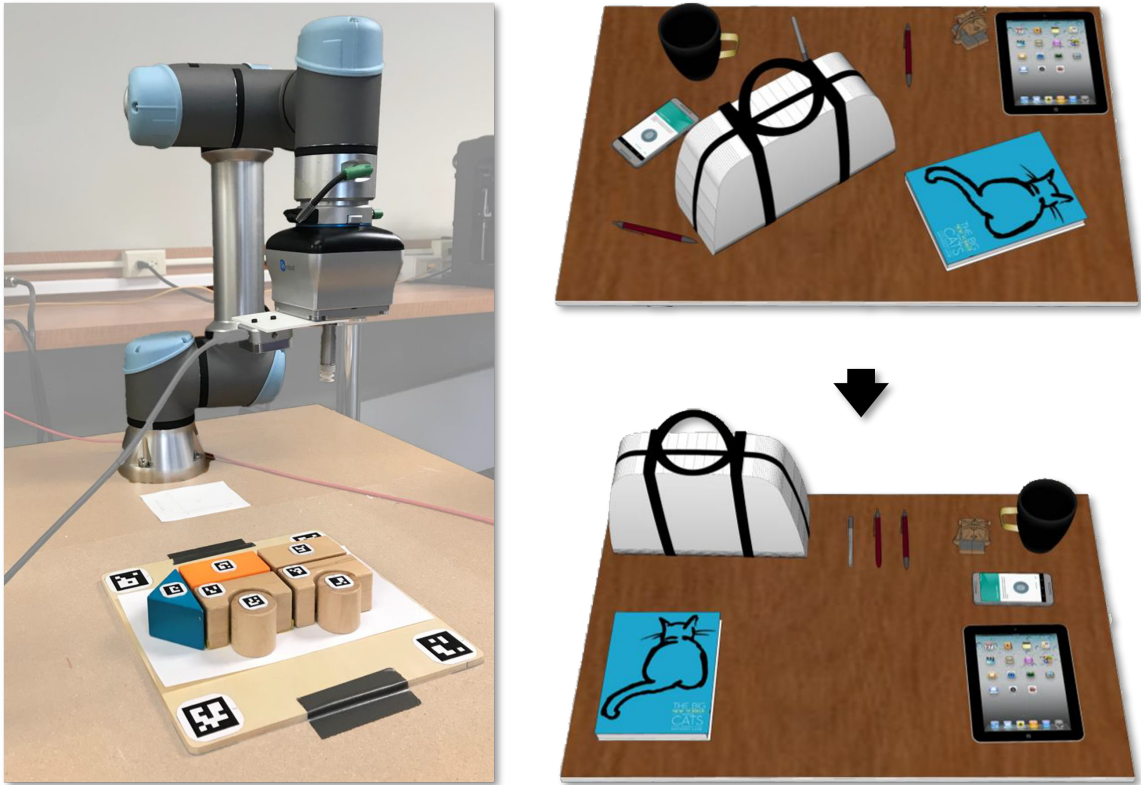


Figure 3.4: [Left] Our hardware setup for evaluating tabletop rearrangement of multiple heterogeneous objects. One of the test cases is also shown. [Right] The illustration of an example instance where many objects of drastically different sizes and weights are to be rearrangements.

similar cost, which in turn limits the applicability of the resulting methods. In many real-world tabletop rearrangement problems, objects are often heterogeneous. For example, in Figure 3.4, some objects are small and thin, e.g., pens, while others can be bulky, e.g., the white bag. Intuitively, objects' sizes and shapes impact the rearrangement planning process - it is more difficult to relocate larger objects temporarily. Furthermore, other properties, such as weight, affect the effort needed to move them around. This further complicates the computation of optimal rearrangement plans. We thus ask a natural question here: Can we leverage objects' properties to guide multi-object rearrangement planning?

With the question in mind, we investigate heterogeneous TORI (HeTORI), in which the characteristics of workspace objects, such as size, shape, weight, and other properties, can vary significantly. Taking object characteristics into consideration immediately leads

to a much more general problem model, allowing each manipulation operation to have a cost that is affected by the properties of the objects. For example, manipulating an object that is large, heavy, and/or fragile is naturally more challenging. As a result, such an operation could take more time to complete. Therefore, a higher cost may be given for such operations than manipulating an object that is small, light, and/or tough. This section focuses on developing methods that take such differences into account. More specifically, we develop methods for addressing two problem variants. In one of the variants, object shape and size are considered in generating the manipulation plan. Object characteristics are directly reflected in the optimization objective in the other variant.

3.5.2 Problem Formulation

HeTORI assumes full knowledge of object characteristics $\mathcal{I} = \{I_1, I_2, \dots, I_n\}$. \mathcal{I} may include properties of objects, including geometry, mass, material properties, and so on. In practice, \mathcal{I} can be estimated based on sensing data.

For HeTORI, if the robot is sufficiently powerful, it may still be the case that grasping/releasing objects takes the same amount of time for each object, regardless of their sizes and mass (with some range); but it could also be that different objects requires different (time) cost to grasp/release. Based on the observation, for HeTORI, two cost objectives are examined, which are:

1. **(PP)** Total number of relocations, i.e., $J(\Pi) = |\Pi|$.
2. **(TI)** Total task *impedance*, i.e.,

$$J(\Pi) = \sum_{(o_i, p_i^1, p_i^2) \in \Pi} f(I_i). \quad (3.1)$$

Specifically, the PP objective is the number of grasps or places a robot needs to execute in a rearrangement plan. The TI objective enables the prioritization of manipulation

actions based on objects’ intrinsic properties, where $f(I_i)$ represents the actual cost of manipulating object o_i , as determined by the robot and I_i . Compared to PP, the TI objective represents the manipulation cost with higher levels of fidelity. For example, if a robot is tasked to rearrange gold and iron bars of the same size and shape, it is certainly better to move iron bars more due to iron’s significantly lower density.

Based on the descriptions so far, HeTORI can be formally summarized as follows:

Problem 3 (HeTORI). *Given two feasible arrangements \mathcal{A}_s and \mathcal{A}_g of objects \mathcal{O} , compute a rearrangement plan Π moving \mathcal{O} from \mathcal{A}_s to \mathcal{A}_g with the minimum cost $J(\Pi)$.*

3.5.3 Weighting Heuristics for HeTORI

Our algorithmic design methodology is general: different (weighting) heuristics can be employed by different search strategies (e.g., TRLB and MCTS) for solving HeTORI. Here, we first describe our carefully constructed heuristics that are applicable to both PP and TI objectives.

3.5.3.1 Collision Probability (HeCP) for PP

In a cluttered workspace, it is difficult to allocate collision-free poses for use as buffers. Even when a pose is collision-free in the current arrangement, it may overlap/collide with some goal poses, blocking the movements of other objects. It is generally more challenging to allocate high-quality buffers for objects with large sizes or aspect ratios (e.g., stick-like objects). A natural question would be: How much do the object’s size and shape impact its collision probability with other objects? We compute an estimated collision probability for each object to answer the question. Based on the collision probability, we propose a heuristic HeCP (Heterogeneous object Collision Probability) to address the buffer allocation challenge in HeTORI and guide the rearrangement search.

Given two objects A and B with fixed orientations, positions of B colliding with A can

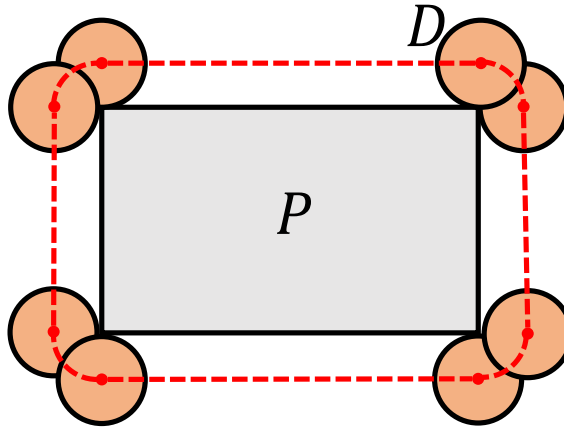


Figure 3.5: An illustration of the Minkowski difference $P \ominus D(0, 0)$ (red dashed region) of a rectangle P and a disc D .

be represented by the *Minkowski difference* of the two objects. That is,

$$A \ominus B(0, 0) := \{a - b \mid a \in P_A, b \in P_B(0, 0)\},$$

where P_A is the point set of A at the current pose and P_B is the point set of B at position $(0, 0)$ with the current orientation. Note that when B is rotational symmetric, the Minkowski difference is the same as the Minkowski sum, which replaces the minus with a plus in the formula above.

Specifically, for a convex polygon P and a disc D , the area of $P \ominus D(0, 0)$ can be simply represented as $S_N = S_P + S_D + r_D C_P$, where S and C are the area and circumference of corresponding objects, r_D is the radius of D . In the example of Figure 3.5, S_P comes from the polygon P in the center of N , S_D comes from the four rounded corners, and $r_D C_P$ comes from the area along the edges. Since one of the objects is a disc, the formula is rotation invariant. Furthermore, if P is at least $2r_D$ away from the boundary of \mathcal{W} , the probability of D colliding with P is

$$\Pr = \frac{S_N}{(H - 2r_D)(W - 2r_D)} = \frac{S_P + S_D + r_D C_P}{(H - 2r_D)(W - 2r_D)} \quad (3.2)$$

Assuming both P and D are small compared to \mathcal{W} , \Pr is a fairly tight upper bound of

the collision probability of P and D in the workspace.

Based on Equation 3.2, the HeCP heuristics can be computed as in Algorithm 8. The algorithm consumes the object characteristics \mathcal{I} . We first compute the area and circumference of each object based on \mathcal{I} (Lines 1-4). In Lines 5-6, we create a disc whose size is the average size of workspace objects. The area and radius of the average-sized disc are denoted as \bar{s} and \bar{r} , respectively. The weight of each object is then computed as the estimated collision probability between the object and the average-sized disc (Lines 7-9).

In general, HeCP measures the difficulty of allocating a collision-free pose for an object and the probability of the sampled pose blocking other objects' movements.

Algorithm 8: HeCP

Input : \mathcal{I} : object characteristics.
Output: HeCP: weights on \mathcal{O}

- 1 **for** $o_i \in \mathcal{O}$ **do**
- 2 $s_i \leftarrow \text{getSize}(I_i)$
- 3 $c_i \leftarrow \text{getCircumference}(I_i)$
- 4 **end**
- 5 $\bar{s} = (\sum_{1 \leq i \leq n} s_i) / n$
- 6 $\bar{r} = \sqrt{\bar{s} / \pi}$
- 7 **for** $o_i \in \mathcal{O}$ **do**
- 8 $w_i \leftarrow \frac{s_i + \bar{s} + \bar{r}c_i}{(H - 2\bar{r})(W - 2\bar{r})}$
- 9 **end**
- 10 **return** $\{w_1, w_2, \dots, w_n\}$

3.5.3.2 Task Impedance (HeTI) for TI

When task impedance is evaluated, directly applying the existing methods, which seek rearrangement plans with the minimum number of actions, may lead to undesirable sub-optimality. For the TI objective, the weighting heuristic is denoted as HeTI. HeTI gives each object o_i a weight $f(I_i)$ as defined in Equation 3.1.

3.5.4 Extended TRLB (ETRLB) for HeTORI

For TRLB, we construct a weighted dependency graph with the heuristics and formulate the corresponding feedback vertex set problem and running buffer minimization problem.

Recall that TRLB first computes a primitive plan and then allocates buffers to check plan feasibility. For HeTORI, we leverage weighting heuristics to guide the primitive plan computation in TRLB, which yields to *Extended TRLB* (ETRLB). To do so, we first construct a weighted dependency graph \mathcal{G}_w , where each vertex v_i has a weight w_i . Correspondingly, in the primitive plan computation process, we solve weighted TBM and weighted RBM of \mathcal{G}_w . For convenience, we use the notations ETBM and ERBM to represent ETRLB with weighted TBM and RBM, respectively. ETBM computes a primitive plan minimizing the total weights of objects moving to buffers. We transform the problem into computing the feedback vertex set of \mathcal{G}_w with the minimum sum of weights, which can be solved by dynamic programming or integer programming similar to TBM in TRLB. The same as the TRLB with RBM, ERBM computes the minimum running buffer size for the rearrangement problem but it assumes each object o_i to take w_i amount of space in buffers.

In the original RBM computation, TRLB fixes the running buffer size and checks whether there is a feasible rearrangement plan given the running buffer size in order to make use of the efficiency of depth-first search. If not, the algorithm increases the running buffer size by one and checks the feasibility again. This process continues until it finds the lowest running buffer size with a feasible primitive plan. Since this framework needs an integer running buffer size, ERBM rounds the weights to the nearest integers so that the sum of weights is still an integer.

For HeTORI with the PP objective, applying HeCP in primitive plan computation discourages relocation of objects for which the allocation of high-quality buffers is difficult, which reduces the challenge in the buffer allocation process. When weighting heuristic HeCP is used, ETBM and ERBM seek primitive plans minimizing the total amount of “difficulty on buffer allocation” and the maximum “concurrent difficulty on buffer alloca-

tion”. For the TI objective, we apply HeTI to primitive plan computation instead.

3.5.5 Extended MCTS (EMCTS) for HeTORI

For MCTS, we use the heuristics with additional improvements, which yields Extended Monte Carlo Tree Search (EMCTS) for heterogeneous instances. Specifically, for HeTORI with the PP objective, EMCTS applies HeCP to the exploration term in the UCB function, replacing constant C with

$$C(1 + \frac{w_i}{\sum_{i=1}^n w_i}).$$

EMCTS prioritizes actions making progress in sending high-weight objects to the goals (moving them to goals or clearing out their goal poses). We do this for two reasons. First, as mentioned in Subsection 3.5.3, it is difficult to move objects with high HeCP weights to buffers. And their allocated buffers are more likely to block other objects’ goal poses. Second, these high-weighted objects at goal poses are guaranteed to be collision-free from other goal poses. For HeTORI with the TI objective, the reward in EMCTS is the total HeTI weights of objects in the goal poses.

Besides the application of weighting heuristics, to tackle the challenge in HeTORI , we introduce two additional improvements to both MCTS and EMCTS.

3.5.5.1 Reducing action space

For each state, we only consider actions a_i whose corresponding object o_i are away from goal poses. This modification significantly reduces the action space when the state is close to the goal state and will not lead to optimality loss since the neglected actions will not make any difference to the workspace.

3.5.5.2 Efficient collision checker for HeTORI

In TORI , MCTS spends most of the computation time on collision checks for buffer allocation and goal pose feasibility checks. The original paper[81] uses the bounding discs

for collision checks. For HeTORI , our collision checker has two steps: in the broad phase, we check collisions between bounding discs of object poses, which aims at pruning out most objects in the workspace that are far from the target object. In the narrow phase, for objects whose bounding discs overlap with that of the target object, we check the collision of their polygonal approximations. We also tried other broad-phase collision checkers, such as quadtrees and uniform space partitions. While these methods have good performance in large-scale collision checking, we observe limited speed-up but a large amount of overhead in maintaining the structures in HeTORI instance. That is because few robotic manipulation instances need to deal with more than 100 objects simultaneously.

3.6 Experimental Results for TORI

We implemented the algorithms of the TRLB framework in Python. Simulated experiments use environments with different density levels ρ , defined as the proportion of the tabletop surface occupied by objects, i.e., $\rho := (\sum_{o_i \in \mathcal{O}} S_{o_i}) / S_{\mathcal{W}}$, where S_{o_i} is the base area of o_i and $S_{\mathcal{W}}$ is the area of \mathcal{W} .

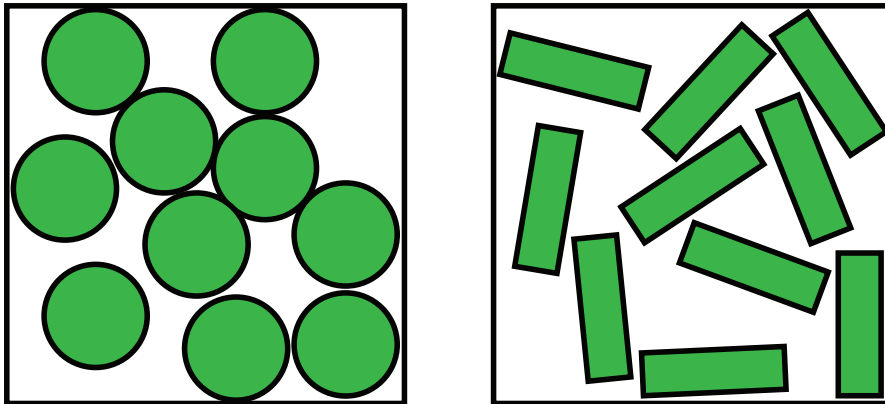


Figure 3.6: [left] 10 cylinders with $\rho = 0.5$, [right] 10 cuboids with $\rho = 0.4$.

Figure 3.6 shows a dense 10-cylinder arrangement with $\rho = 0.5$, and a dense 10-cube arrangement with $\rho = 0.4$. The experiments are executed on an Intel[®] Xeon[®] CPU at 3.00GHz. Each data point is the average of 30 cases except for unfinished trials, given a time limit of 300 sec. per case.

3.6.1 Ablation Study for Cylindrical Objects

We first present experiments with cylindrical objects to compare lazy buffer generation algorithms given different options, including: (1) Primitive plan computation: running buffer minimization (RBM), total buffer minimization (TBM), random order (RO); (2) Buffer allocation methods: optimization (OPT), sampling (SP); (3) High level planners: one-shot (OS), forward search tree (ST), bidirectional search tree (BST); and (4) With or without preprocessing (PP). Here, the one-shot (OS) planner is using primitive plans and buffer allocation (Subsection 3.4.1) without tree search (Subsection 3.4.2). In OS, we attempt to compute a feasible rearrangement plan up to $30|\mathcal{O}|$ times before announcing a failure. Notice that at least $|\mathcal{O}|$ actions are required for solving any instance.

A full TRLB algorithm is a combination of components, e.g., RBM-SP-BST stands for using the primitive plans that minimize running buffer size, performing buffer allocation by sampling, maintaining a bidirectional search tree, and doing so without preprocessing.

For evaluation, we first compare the primitive plan computation options, using sampling-based buffer allocation, bidirectional tree search and no preprocessing. TBM and RBM plans are computed using dynamic programming solvers from Chapter 2. The results are shown in Figure 3.7. Even though plans generated by TBM-SP-BST are slightly shorter than RBM-SP-BST, TBM-SP-BST is less scalable as either the density level or the number of objects in the workspace increases. Compared to RBM plans, individual RO plans can be generated almost instantaneously but there is little benefit in computation for the overall algorithm. The results indicate that RBM should be used for primitive plan computation as it results in efficient and high-quality solutions.

In Figure 3.8, buffer allocation methods are compared using the RBM primitive planner and the OS high-level planner. Optimization-based allocation guarantees completeness and generates high-quality plans but it is computationally expensive. When $\rho = 0.5$, the success rate tends to be low in instances with a small number of objects. That is because for the given density level, the smaller the number of objects, the larger the object size relative to

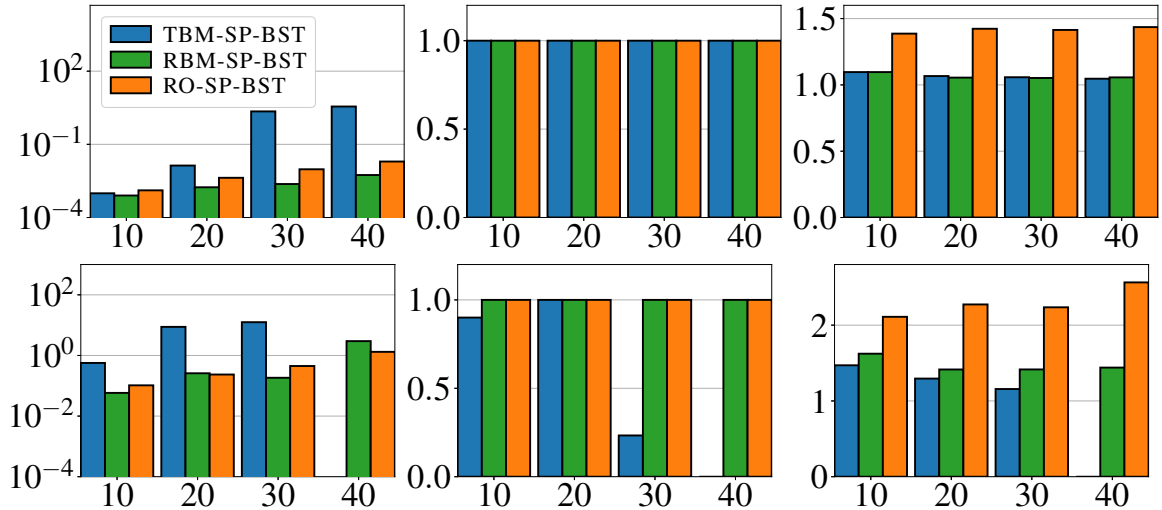


Figure 3.7: Comparison of primitive planners with 10-40 cylinders and density levels $\rho = 0.3$ (top), 0.5 (bottom) (left: computation time in seconds; middle: success rate; right: number of actions as multiples of $|\mathcal{O}|$).

the environment, and the smaller the configuration space size relative to the environment.

Thus, precisely allocating buffer locations with OPT is helpful in these cases.

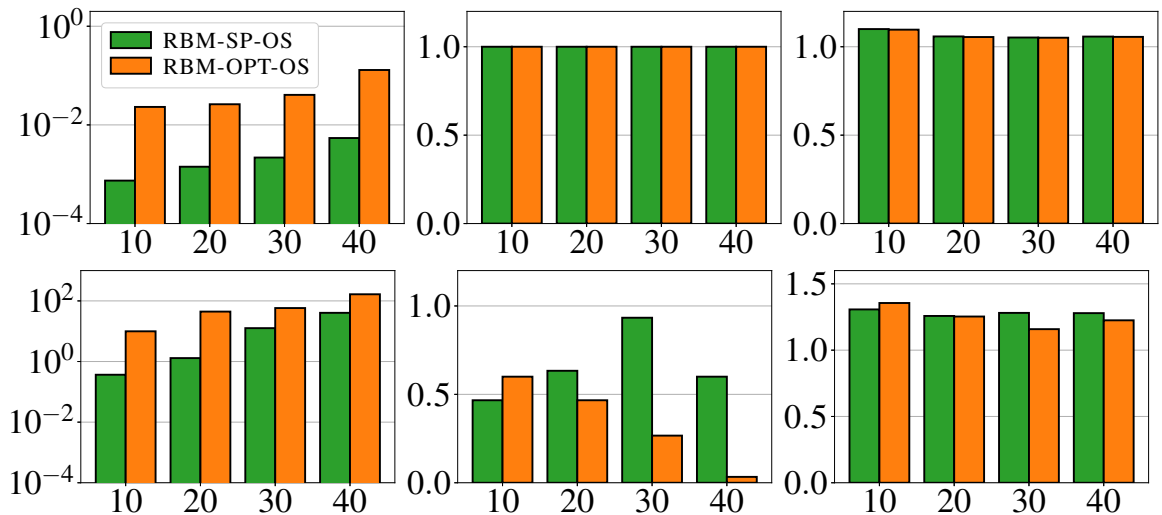


Figure 3.8: Comparison of buffer allocation methods with 10-40 cylinders at density levels $\rho = 0.3$ (top), 0.5 (bottom) (left: computation time in seconds; middle: success rate; right: number of actions as multiples of $|\mathcal{O}|$).

The effectiveness of the high-level planners and preprocessing are shown in Figure 3.9, which suggests that ST, BST and preprocessing are all effective in increasing success rate in dense environments. In addition, preprocessing significantly speeds up computation in

large scale dense cases at the price of extra actions to execute preprocessing. By simplifying the dependency graph with preprocessing, less time is needed to compute a primitive plan.

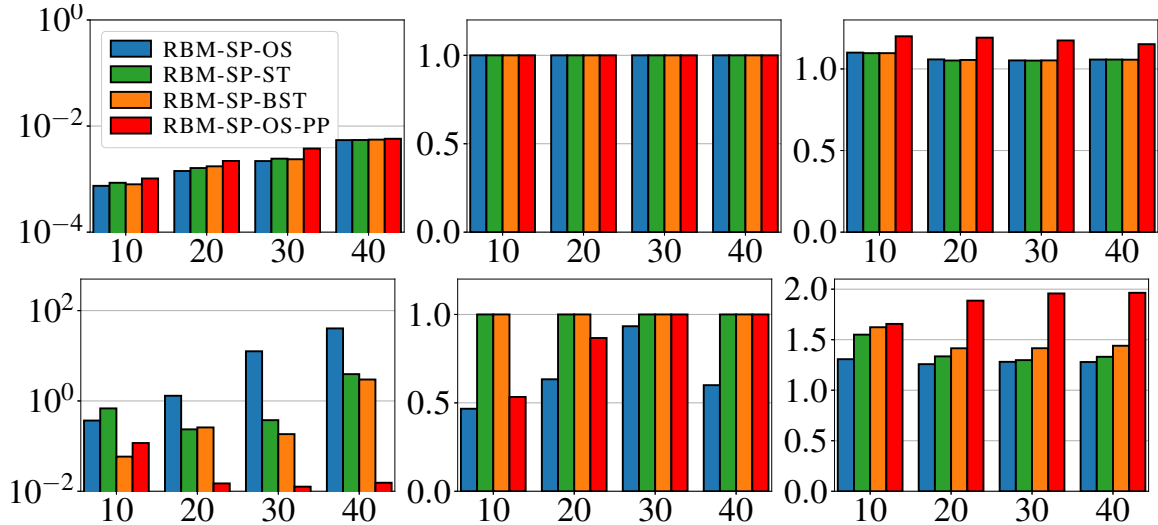


Figure 3.9: Comparison among high-level frameworks and OS with preprocessing. There are 10-40 cylinders in the workspace at density levels $\rho = 0.3$ (top), 0.5 (bottom) (left: computation time in seconds; middle: success rate; right: number of actions as multiples of $|\mathcal{O}|$).

The robustness of ST and BST are further evaluated with “dense-small” instances where a few objects are packed densely (Figure 3.10). The bidirectional search tree has a higher success rate in these cases, especially in 5-object instances.

In addition to the above evaluations, we also tried integrating the preprocessing into the BST framework (RBM-SP-BST-PP), which speeds up the computation: for 60-object instances with $\rho = 0.5$, only 63% of them can be solved by RBM-SP-BST in 300 seconds. All of them, however, can be solved together with the preprocessing and the solution time averaged 0.29 seconds. Similarly to the results in Figure 3.9, preprocessing makes the solution plan much longer than necessary (needs around 30% more actions than RBM-SP-BST). Based on the analysis on computation time, success rate, and solution quality, RBM-SP-BST is the best overall combination, and preprocessing significantly speeds up the solver with a reduction of solution quality.

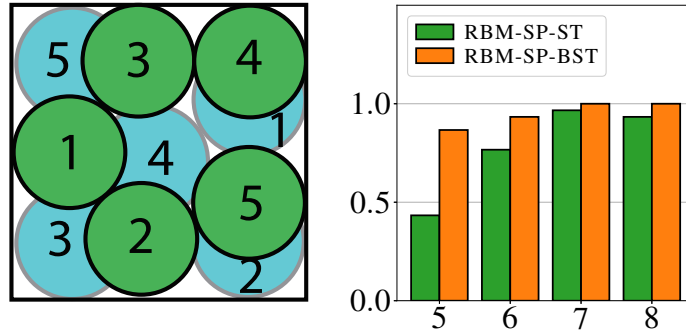


Figure 3.10: Comparison between ST and BST frameworks with “dense-small” instances where 5-8 cylinders packed in the environment and density level $\rho = 0.5$. [left] An example with 5 cylinders, [right] success rate of methods.

3.6.2 Comparison with Alternatives for Cylindrical Objects

We compare the proposed method RBM-SP-BST with BiRRT(fmRS) [47] and a MCTS planner [81], which, to the best of our knowledge, are state-of-the-art planners for TORI. The MCTS planner is a C++ solver, while the other two methods are implemented in Python. Besides success rate, solution quality, and computation time, we also compare the number of collision checks which are time-consuming in most planning tasks. In Figure 3.11, we compare the methods in large scale problems with $\rho = 0.3$. The success rate is 100% for all. Our method, RBM-SP-BST, avoids repeated collision checks due to the use of the dependency graph. BiRRT(fmRS), which only uses dependency graphs locally, spends a lot of time and conducts a lot of collision checks to generate random arrangements. MCTS generates solutions with similar optimality but does so also with a lot of collision checking, which slows down computation. We note that a value of 1 in the right figure (number of actions) is the minimum possible, so both RBM-SP-BST and MCTS compute high-quality solutions, which RBM-SP-BST does slightly better. To sum up, in sparse large scale instances, RBM-SP-BST is two magnitudes faster and conducts much fewer collision checks than the alternatives.

Next, we compare the methods in “dense-small” instances (Figure 3.12). Here, RBM-SP-BST is the only method that maintains high success rate in these difficult cases.

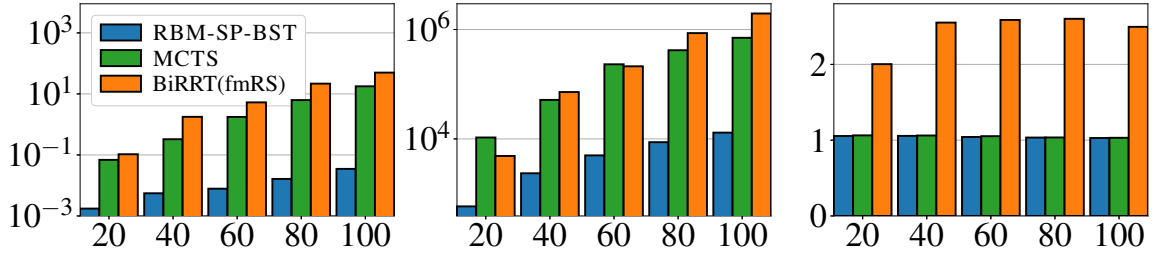


Figure 3.11: Comparison of algorithms with 20-100 cylinders at density level $\rho = 0.3$ (left: computation time in seconds; middle: number of collision checks; right: number of actions as multiples of $|\mathcal{O}|$).

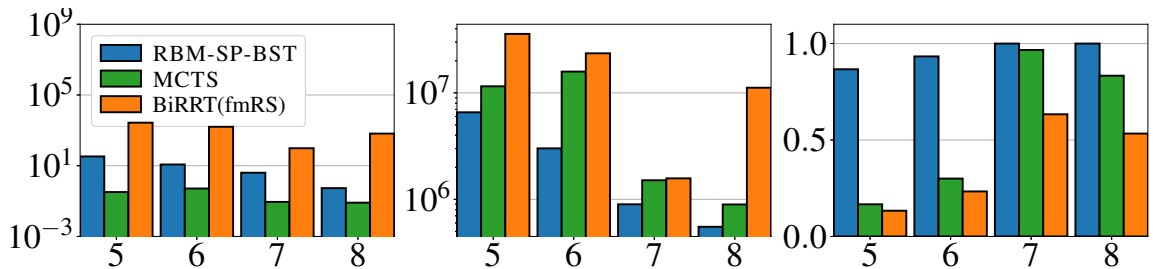


Figure 3.12: Comparison of methods on “dense-small” instances where 5-8 objects are packed in an environment with $\rho = 0.5$ (left: computation time in seconds; middle: number of collisions; right: success rate).

We further compare the performance of RBM-SP-BST and MCTS in lattice rearrangement problems recently studied in the literature [93]. An example with 15 objects is shown in Figure 3.13[left]. In the start and goal arrangements, gaps between adjacent objects are set to be 0.01 object radius, and thus buffer allocation is challenging for sampling-based methods. While MCTS tries all actions on each node, RBM-SP-BST can detect the embedded combinatorial object relationship via the dependency graph and therefore needs less buffer allocations. As shown in Figure 3.13[right], RBM-SP-BST has much higher success rate in lattice rearrangement tasks.

3.6.3 Cuboid Objects

Because the MCTS solver only supports cylindrical objects, we only compare RBM-SP-BST and BiRRT(fmRS) in the cuboids setup (Figure 3.6[right]). When $\rho = 0.3$, RBM-SP-BST computes high quality solutions efficiently, while BiRRT(fmRS) can only solve

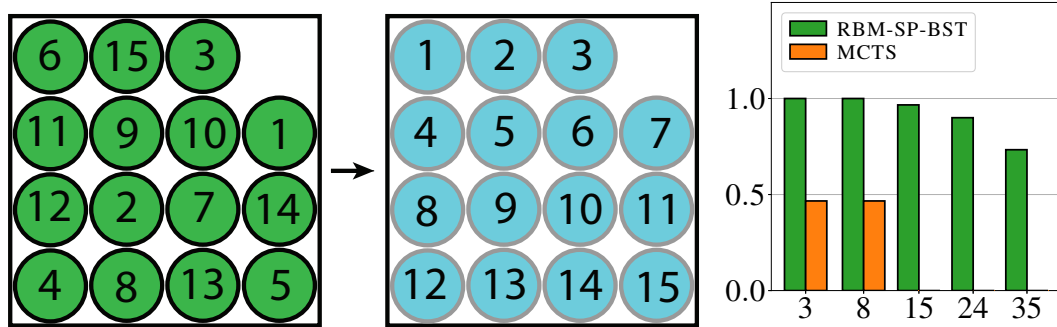


Figure 3.13: Comparison among methods in lattice instances with 3-35 objects. [left] lattice example; [right] success rate

instances with up to 20 cuboids. We mention that, when $\rho = 0.4$, BiRRT(fmRS) cannot solve any instance, but RBM-SP-BST can solve 50-object rearrangement problems in 28.6 secs on average.

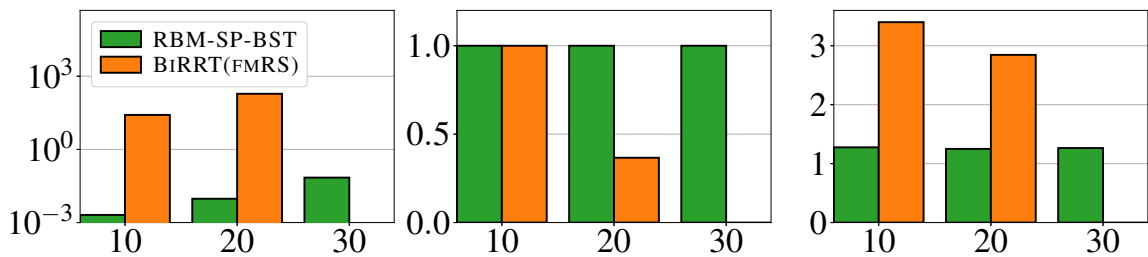


Figure 3.14: Comparison between methods in cuboid instances with 10-30 cuboids and $\rho = 0.3$ (left: computation time in seconds; middle: success rate; right: number of actions as multiples of $|\mathcal{O}|$).

3.6.4 Hardware Demonstration

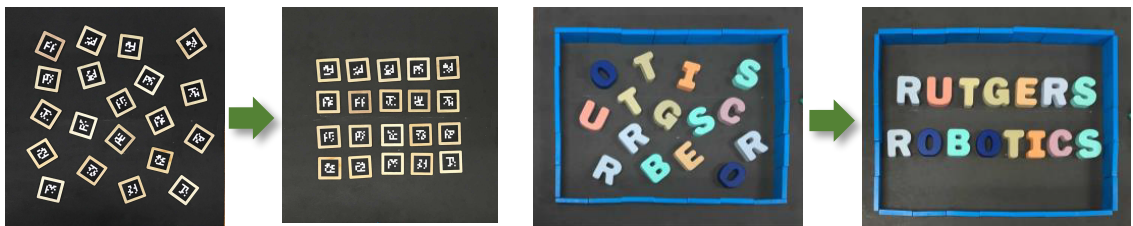


Figure 3.15: Experimental settings in addition to that of Figure 3.1.

We further demonstrate that the plans computed by TRLB can be readily executed on real robots in a complete vision-planning-control pipeline. Our hardware setup consists of

a UR-5e robot arm, an OnRobot VGC 10 vacuum gripper, and an Intel RealSense D435 RGB-D camera. As shown in the accompanying video¹, TRLB solves all attempted instances (Figure 3.1 and Figure 3.15), which involves concave objects, in an apparently natural and efficient manner.

3.7 Experimental Results for HeTORI

The proposed algorithms’ performance is evaluated using simulation and real robot experiments. All methods are implemented in Python, and the experiments are executed on an Intel[®] Xeon[®] CPU at 3.00GHz. Each data point is the average of 50 cases except for unfinished trials, given a time limit of 600 seconds per case.

3.7.1 Numerical Results in Simulation

Simulation experiments are conducted in two scenarios:

1. (RAND) In the RAND (random) scenario, for each object, the base shape is randomly chosen between an ellipse and a rectangle. The aspect ratios and the areas are uniformly random values in $[1.0, 3.0]$ and $[0.05, 1]$, respectively. The areas of the objects are then normalized to a certain sum S , whose value depends on specific problem setups. Examples of the RAND scenario are shown in the first row of Figure 3.16. This setup is used to examine algorithm performance in general HeTORI instances.
2. (SQ) In the SQ (squares) scenario, there are 2 large squares and $|\mathcal{O}| - 2$ small squares. The area ratio between the large and small squares is 9 : 1. This setup simulates the rearrangement scenario where object size varies significantly. Examples of arrangements in the SQ scenario are shown in the second row of Figure 3.16.

For each test case, object start and goal poses are uniformly sampled in the workspace for both scenarios. The sampling process for a single test case is repeated in the event

¹The video is available [online](#). More demonstrations are available [here](#).

of pose collision until a valid configuration is obtained. We use the *density level* ρ to measure how cluttered a workspace is. It is defined as $(\sum_{o_i \in \mathcal{O}} S_i)/S_W$, where S_i and S_W represents the size of o_i and the workspace respectively. In other words, ρ represents the proportion of the workspace occupied by objects. Figure 3.16 shows examples of RAND and SQ scenarios for $\rho = 0.2-0.4$, where $\rho = 0.4$ is already fairly dense (e.g., 3rd column Figure 3.16). We limit the maximum number of objects in a test case to 40 as typical HeTORI cases are unlikely to have more objects.

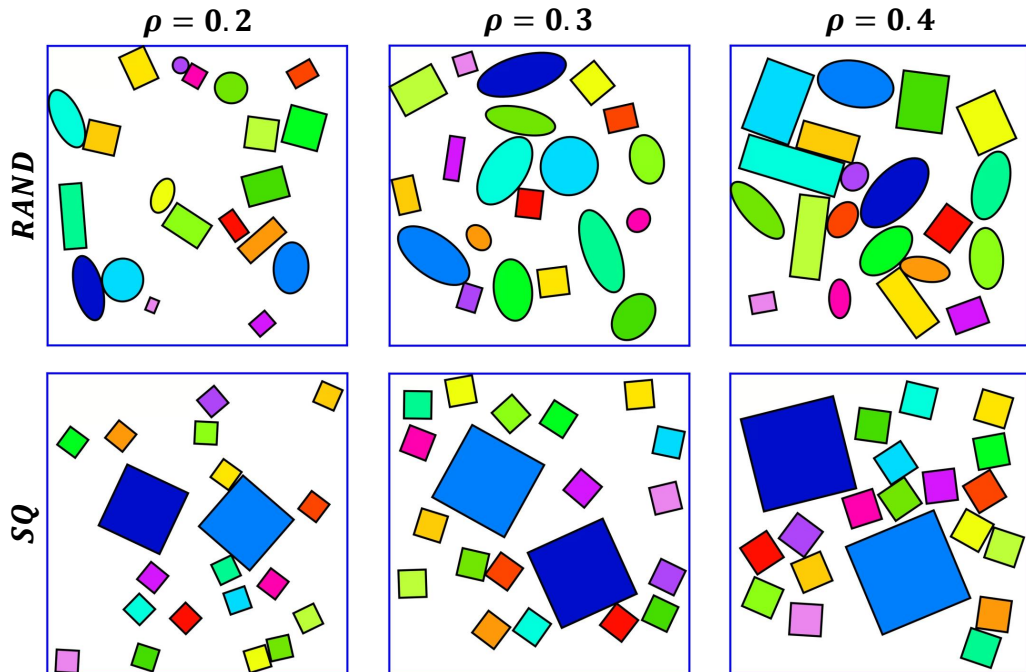


Figure 3.16: Illustrations of some simulation test cases at different densities. [top] RAND instances under different density levels. [bottom] SQ instances under different density levels.

In Figure 3.17, we first evaluate algorithm performance in dense RAND instances ($\rho = 0.4$) under the PP objective. Compared with the original TBM, ETBM shows a 7.8% improvement in solution quality with only 52% computation time, when both TBM and ETBM have 98% success rates in 20-object instances. Suffering from the expansion of solution space, neither TBM or ETBM is scalable as the number of objects increases. With HeCP, both ERBM and EMCTS show clear advantages compared to the original methods

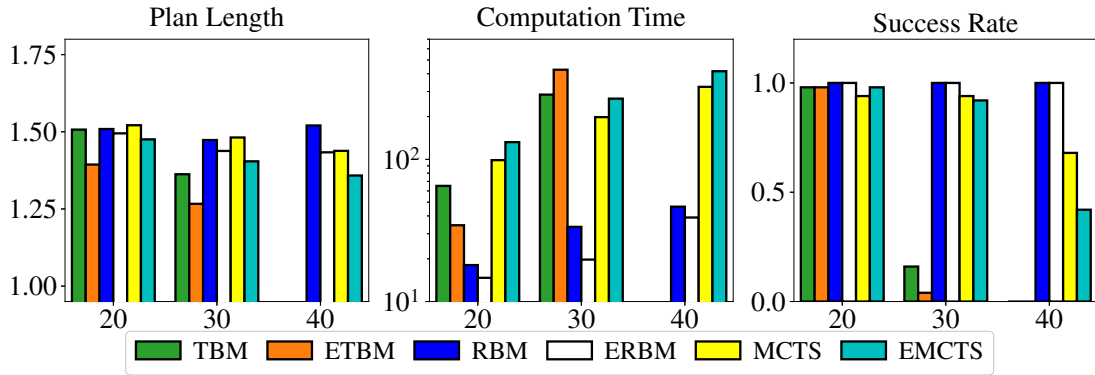


Figure 3.17: Algorithm performance in RAND instances with $\rho = 0.4$ and 20-40 objects. [Left] Plan length as multiples of $|\mathcal{O}|$. [Middle] Computation time (secs). [Right] Success rate.

(RBM and MCTS) in solution quality as the number of objects increases. In 40-object instances, plans computed by ERBM and EMCTS save 3.6 and 3.2 actions over those by RBM and MCTS, respectively. While ERBM spends less time than RBM to solve RAND instances, EMCTS spends slightly more time on computation since the weights are added to the exploration term. In general, ETBM computes solutions with the best quality in small-scale instances, ERBM is most scalable as $|\mathcal{O}|$ increases, and EMCTS balances between optimality and scalability, computing high-quality solutions in 30-object instances with a high success rate.

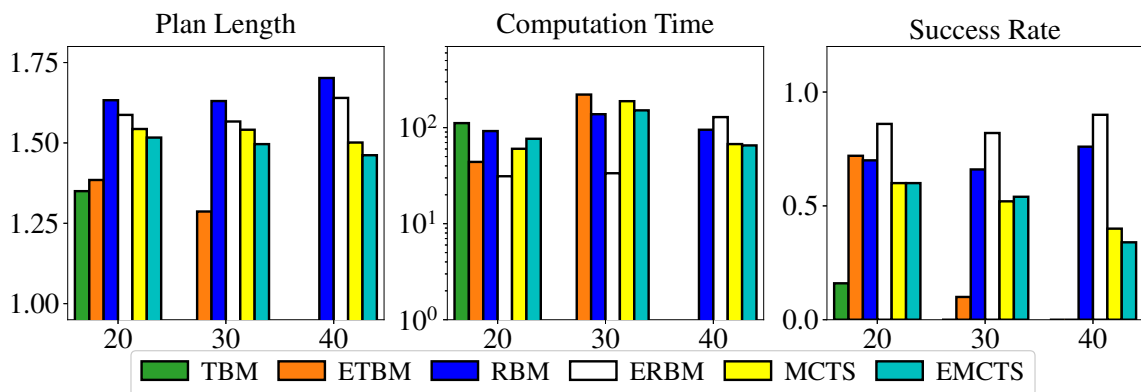


Figure 3.18: Algorithm performance in SQ instances with $\rho = 0.4$ and 20-40 objects. [Left] Plan length as multiples of $|\mathcal{O}|$. [Middle] Computation time (secs). [Right] Success rate.

In SQ instances, it is difficult to displace the large squares in the cluttered workspace.

Figure 3.18 shows the algorithm performance in SQ instances with $\rho = 0.4$ under the PP objective. The results suggest that ETBM with HeCP effectively increases the success rate from 16% to 72% when $|\mathcal{O}| = 20$. Similarly, the success rate of ERBM is around 15% higher than RBM when $|\mathcal{O}| = 20, 30$, and 40. While ERBM solves more test cases, the computed solutions are even 5% – 7% shorter than RBM. As for MCTS methods, EMCTS computes 3% – 5% shorter paths than EMCTS with a similar success rate and computation time.

Besides dense instances, we also evaluate the efficiency gain of HeCP at different density levels when $|\mathcal{O}| = 20$. The results of RAND and SQ scenarios are shown in Figure 3.19 and Figure 3.20 respectively. In sparse RAND instances ($\rho = 0.2$ or 0.3), ETBM and ERBM return plans with similar optimality without additional computational overheads. When $\rho = 0.3$, EMCTS spends additional 5 seconds for exploration and receives around 3% improvements on path length.

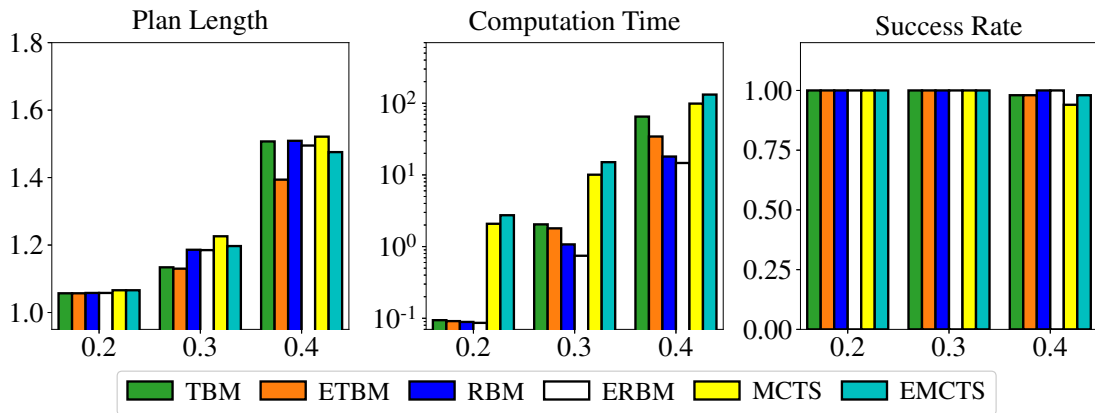


Figure 3.19: Algorithm performance in RAND instances under different density levels and $|\mathcal{O}| = 20$. [Left] Plan length as multiplies of $|\mathcal{O}|$. [Middle] Computation time (secs). [Right] Success rate.

In sparse SQ instances, HeCP helps improve computation time, which contributes to an increase in success rate. Compared with TBM, ETBM saves 70% computation time when $\rho = 0.2$ and 0.3 and increases the success rate from 82% to 98% when $\rho = 0.2$. Similarly, compared with RBM, ERBM saves 56% and 82% computation time when $\rho = 0.2$ and 0.3. In ETBM and ERBM, HeCP speeds up computation without reducing solution quality.

Compared with MCTS, EMCTS computes 5% shorter plans, saves 33% computation time, and increases the success rate by 16% when $\rho = 0.3$.

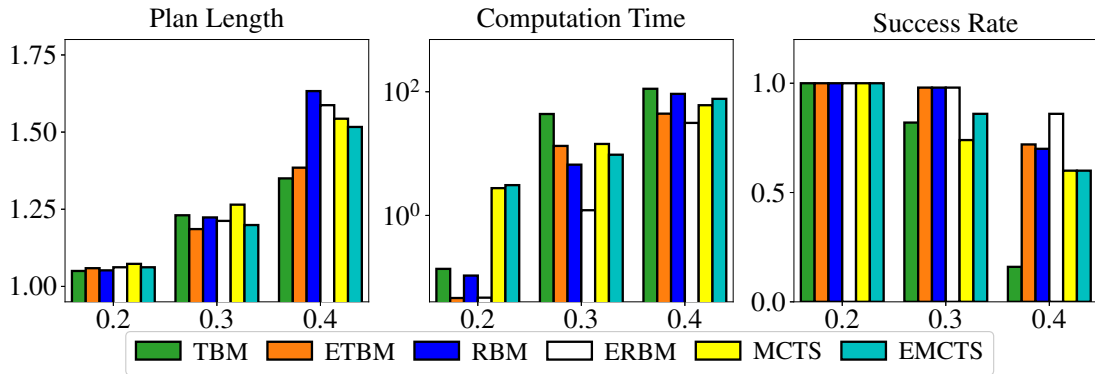


Figure 3.20: Algorithm performance in SQ instances under different density levels and $|\mathcal{O}| = 20$. [Left] Plan length as multiplies of $|\mathcal{O}|$. [Middle] Computation time (secs). [Right] Success rate.

In Figure 3.21 and Figure 3.22, we show the algorithm performance of HeTORI with TI objective in RAND and SQ instances respectively. $\rho = 0.3$ in the test cases. In RAND instances, where only around 10% objects need buffer locations, the total task impedance of computed plans is similar. Compared with original methods (TBM, RBM, and MCTS), ETBM, ERBM, and EMCTS reduce task impedance by 1% – 7%. In SQ instances, object impedance varies greatly. In this case, methods with HeTI compute much better solutions. Compared with TBM, ETBM reduce task impedance by over 30%. Similarly, ERBM reduces task impedance by around 27%. Compared with MCTS, EMCTS reduces task impedance by 6% – 15% but with additional overhead.

3.7.2 Demonstrations in Simulation and Real-World

In the accompanying video ², we further demonstrate that our algorithms can be applied to practical instances with general-shaped objects in both simulation and the real world. For simulation instances, the rearrangement plans are executed in Pybullet. For real-world instances, the objects are detected with an Intel RealSense D405 RGB-D camera and ma-

²The video is available [online](#).

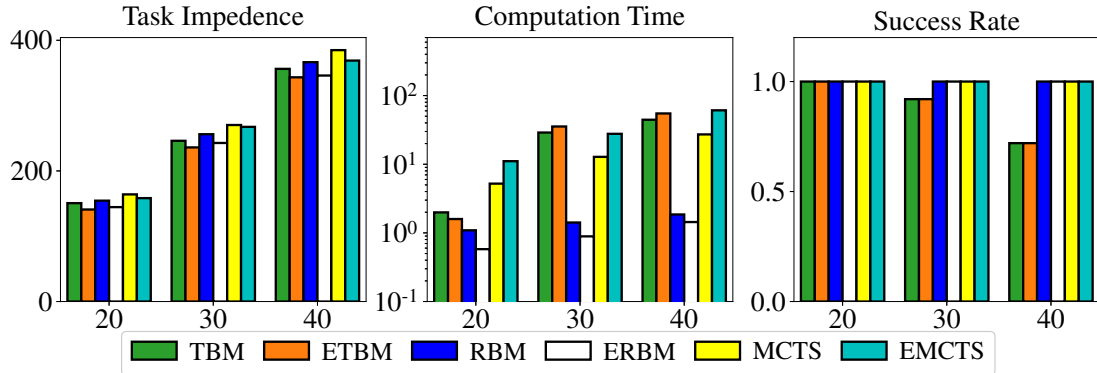


Figure 3.21: Algorithm performance in RAND instances with TI objective. $\rho = 0.3$, $20 \leq |\mathcal{O}| \leq 40$. [Left] Total task impedance. [Middle] Computation time (secs). [Right] Success rate.

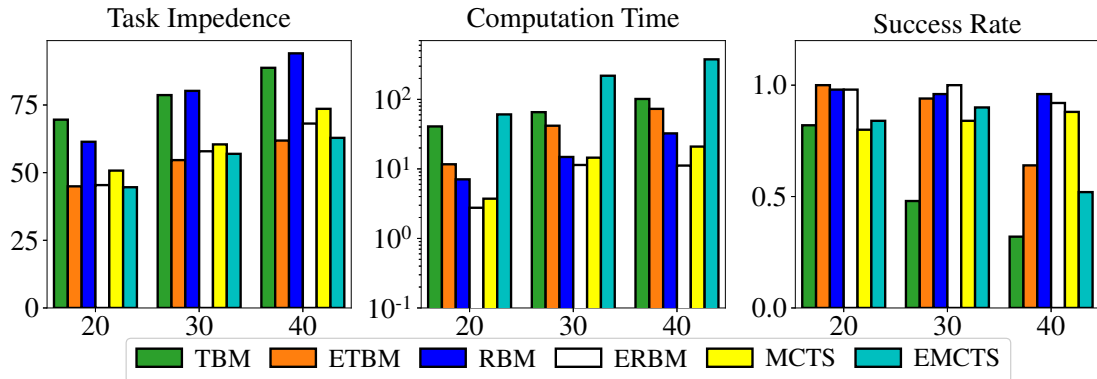


Figure 3.22: Algorithm performance in SQ instances with TI objective. $\rho = 0.3$, $20 \leq |\mathcal{O}| \leq 40$. [Left] Total task impedance. [Middle] Computation time (secs). [Right] Success rate.

nipulated with an OnRobot VGC 10 vacuum gripper on a UR-5e robot arm. Since object recognition and localization are not the focus of this study, we use fiducial markers for realizing these. The workspaces for rearrangement are rather confined (in Figure 3.23, the white areas for the first two and the wooden board for the third), translating to very high object densities, between 35-37%. In the SQ instance with 10 wooden planks, our proposed methods ETBM and ERBM offer advantages over TBM and RBM in both solution quality and computation time, saving 1 and 4 actions, respectively. Furthermore, EMCTS is able to find a 15-action plan in just 13.70 secs while MCTS fails to find a solution even after 2 minutes of computation.

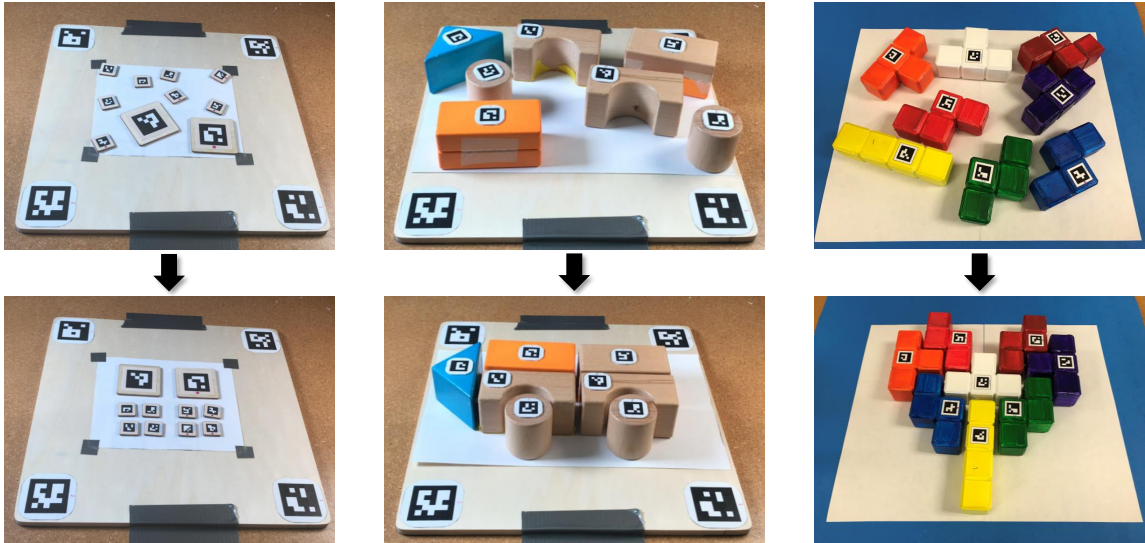


Figure 3.23: Physical experiment/demo setups. [left] Dense SQ instance with 10 square wooden planks. [middle] Rearranging densely-packed thick wooden blocks of different shapes and sizes. [right] Rearranging 3d-printed Tetris pieces into a heart shape.

3.8 Summary

The TRLB framework proposed in this work employs the dependency graph representation and a lazy buffer allocation approach for efficiently solving the problem of rearranging many tightly packed objects on a tabletop using internal buffers (TORI). Extensive simulation studies show that TRLB computes rearrangement plans of comparable or better quality as the state-of-the-art methods, and does so up to 2 magnitudes faster.

We further examine rearranging heterogeneous objects on a tabletop (HeTORI) using two different objectives: PP and TI. The PP objective assumes each object requires an equal amount of manipulation cost for a pick-n-place, while utilizing the object’s shape and size can enhance rearrangement efficiency. On the other hand, the TI objective evaluates the total task impedance, where the manipulation cost of each object varies based on its specific characteristics, such as size or weight. To optimize these objectives, we propose weighting heuristics and build SOTA algorithms with them. Extensive simulation experiments confirm the efficiency of our proposed methods.

Demonstration with real robot experiments shows that the solutions computed by the

proposed TORI and HeTORI solvers are efficient and appear natural. As such, the solutions can potentially be deployed as part of home automation and industrial automation solutions in next-generation robots.

CHAPTER 4

TRLB FOR DUAL ARM COORDINATION

4.1 Motivation

In solving multi-object rearrangement problems, employing multiple arms is a straightforward way to expand the workspace [94] and increase overall system throughput[95]. Toward enabling effective dual-arm (and multi-arm) coordination, a difficult challenge at present, this work investigates the *cooperative dual-arm rearrangement* (CDR) problem, where two robot arms' workspaces partially overlap, and each robot is responsible for a portion of the workspace (Figure 1.2[Left]). In CDR, robot-robot collaboration must be considered to realize higher throughput. Certain settings benefit from having more robots, e.g., one arm may hold an object while other arms make the goal pose of the object available. This will lead to efficiency gain as compared with using a single robot. There are also added challenges, such as some objects being handed off from one robot to another, which requires careful synchronization.

For task planning, the proposed method employs lazy or delayed verification and efficiently computes high-quality solutions for non-monotone instances in a cluttered environment. As a key component of the algorithmic solution, this work proposes a dependency graph-guided heuristic search procedure for coordinating robot-robot object handoffs and individual pick-n-places that support multiple makespan evaluation metrics.

For motion planning, we propose *Makespan-Optimized Dual-Arm (Task and Motion) Planner* (MODAP). MODAP has the following main contributions: First, MODAP intelligently samples inverse kinematics (IK) solutions during the task planning (i.e., when objects are picked or placed) phase, generating multiple feasible motion trajectories for downstream planning and improving long-horizon plan optimality. Second, MODAP leverages

a recent GPU-accelerated planning framework, cuRobo [96], to quickly generate high-quality motion plans for our dual-arm system, resulting in magnitudes faster computation of dynamically smooth motions.¹ MODAP performs further trajectory optimization over the trajectories from cuRobo to accelerate the full plan.

4.2 Related Work

Multi-Object Rearrangement: Single arm object rearrangement lies within the broader area of Task and Motion Planning (TAMP). Typical problems in this domain [73, 69, 74, 75, 97] involve arranging multiple objects to assume specific goal poses. Certain variations, however, such as NAMO (Navigation among Movable Obstacles) [6, 77], and retrieval problems [32, 78, 44, 98], focus on clearing out a path for a target object or robot. During the process, obstacles that need to be displaced are identified. Rearrangement may be approached either via simple but inaccurate non-prehensile actions, e.g., pushes [73, 79, 80, 44], or more purposeful prehensile actions, such as grasps [9, 47, 75].

Focusing on inherent combinatorial challenges associated with rearrangement tasks, some planners assume external space for temporary object storage [31, 1, 32, 74], while others exploit problem linearity to simplify the search [84, 6, 77, 85]. By linking multi-object rearrangement to established graph-based problems, efficient algorithms have been obtained for various tasks and objectives [1, 74, 31]. When external free space is not available, the robot arm needs to allocate collision-free locations for temporary object displacements [47, 86, 97]. In our work, we adopt the idea of “lazy buffer allocation” [97] to the dual-arm scenario.

Multi-robot rearrangement requires additional computation on task assignment and coordination. Ahn et al. [99] coordinate robots by maximizing the number of “turn-taking” moments when one arm is picking an obstacle from the workspace while the other arm is

¹We note that, while cuRobo can be applied to dual-arm motion planning, it cannot be directly applied to solve CDR because the two robots’ plans cannot be readily synchronized due to asynchronous pick-n-place actions.

placing the previous obstacle at the external space. Shome et al.[95] assume robot arms pick-n-places simultaneously and only solve monotone rearrangement problems, where each object can move directly to the goal pose. For objects that need to be moved to a pose outside the reachable region of a robot arm, the task can be accomplished by coordinating multiple arms to handoff the objects around[94]. Cooperative pick-n-place, a problem related to multi-arm rearrangement, is well-studied in the area of printed circuit board assembly tasks[100, 101]. These problems do not have ordering constraints on pick-n-place tasks, i.e. all the items can move directly to goal poses in any ordering. Research in these topics tends to consider multiple grippers equipped on a single arm rather than multiple arms, which reduces system flexibility. In our work, we compute dual-arm rearrangement plans for dense non-monotone instances without external storage space.

Dependency Graph: Dependencies between objects in rearrangement tasks can be naturally represented as a dependency graph, which was first applied to general multi-body planning problems [46] and then rearrangement [9, 47]. In rearrangement, different choices of grasp poses and paths give rise to multiple dependency graphs for the same problem instance, which limits the scalability in computing a solution via such representations. Prior work [1] has applied full dependency graphs to address TORO (Tabletop Object Rearrangement with Overhand Grasps), showing that the problem embeds a NP-hard Feedback Vertex Set problem [30] and a Traveling Salesperson Problem [29].

More recently, some of the authors [74] examined another optimization objective, running buffers, which is the size of the external space needed for temporary object displacements in the rearrangement task, and also examined an unlabeled setting, where goal poses of objects are interchangeable. Similar graph structures are also used in other robotics problems, such as packing problems [48]. Deep neural networks have been also applied to detect the embedded dependency graph of objects in a cluttered environment to determine the ordering of object retrieval [78].

4.3 Cooperative Dual-Arm Rearrangement (CDR)

4.3.1 Problem Statement

Consider a 2D bounded workspace $\mathcal{W} \subset \mathbb{R}^2$ containing a set of n cylindrical objects $\mathcal{O} = \{o_1, \dots, o_n\}$. An arrangement \mathcal{A} of these objects is a set of poses $\{p_1, \dots, p_n\}$ with each pose $p_i = (x_i, y_i) \in \mathcal{W}$. \mathcal{A} is *feasible* if the footprints of objects are inside \mathcal{W} and pair-wise disjoint. Outside the workspace, two robot arms $\mathcal{R} = \{r_1, r_2\}$ are tasked to manipulate objects from a feasible start arrangement \mathcal{A}_s to another feasible goal arrangement \mathcal{A}_g (e.g., Figure 1.2[Left]). Each robot arm r_i has a connected reachable region $\mathcal{S}(r_i) \subseteq \mathcal{W}$. Robot r_i can only manipulate within $\mathcal{S}(r_i)$.

It is assumed that $\mathcal{S}(r_1) \cup \mathcal{S}(r_2) = \mathcal{W}$. The overlap ratio ρ is defined as $\rho = \frac{|\mathcal{S}(r_1) \cap \mathcal{S}(r_2)|}{|\mathcal{W}|}$, which is the proportion of the environment that can be reached by both robots. In Figure 4.1[Left], we show a workspace with $\rho = 0.3$. Robot arm r_1 can reach objects whose centers are on the left of the red dashed line, which include all the objects at start poses (O_1, O_2, O_3) and o_1, o_2 at goal poses (G_1, G_2). Robot arm r_2 can reach objects whose centers are on the right of the blue dashed line, which include all the objects at goal poses (G_1, G_2, G_3) and o_1, o_2 at start poses (O_1, O_2). Objects with centers between the dashed lines can be reached by both.

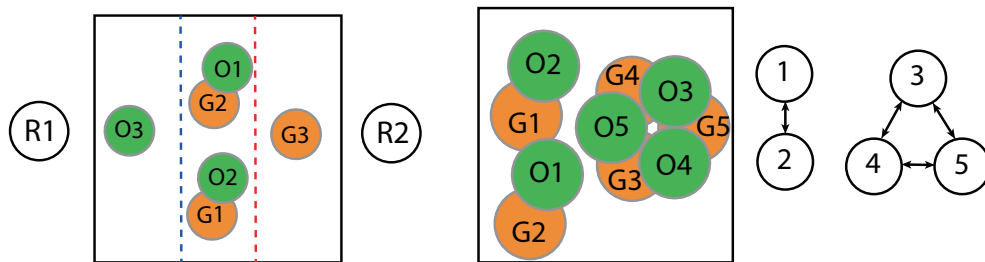


Figure 4.1: [Left] A working example of CDR instance with $\rho = 0.3$. For each object o_i , the start and goal poses are represented by green disc O_i and orange disc G_i respectively. [Right] A CDRF instance and its corresponding dependency graph.

We consider two manipulation primitives: (overhand) *pick-n-place* and *handoff*. In each pick-n-place, an arm moves above an object o_j , grasps it from \mathcal{W} , transfers it atop the

workspace, and places it at a collision-free pose inside \mathcal{W} . We allow a *handoff* operation when an object needs to cross between $\mathcal{S}(r_1) \setminus \mathcal{S}(r_2)$ and $\mathcal{S}(r_2) \setminus \mathcal{S}(r_1)$. In each handoff, an arm, say r_1 , grasps an object o_j from \mathcal{W} , passes the object to the other arm r_2 at the predefined handoff pose above the environment. r_2 receives o_j and places it at a collision-free pose in \mathcal{W} . A handoff is shown in Figure 1.2[Right].

As for the motion of each arm r_i , \mathcal{C}_{free}^i is a set of collision-free configurations for r_i without considering collisions with workspace objects or the other robot arm. Throughout the rearrangement, each arm has $n + 1$ motion modes: transit mode TS (moving on its own) and transfer modes TF_j (transferring the object o_j), $\forall j = 1, \dots, n$. Therefore, the state space Γ_i of an arm r_i is the Cartesian product $\mathcal{C}_{free}^i \times M$, where M is the motion mode set. A path of a robot arm r_i is defined as $\pi_i : [0, T] \rightarrow \Gamma_i$ with $\pi_i[0] = \pi_i[T] = (q_i^*, TS)$, where T is the makespan of the rearrangement plan and q_i^* is the rest pose of arm r_i .

The rearrangement problem we study seeks a path set $\Pi = \{\pi_1, \pi_2\}$, such that robot paths are collision-free: for all $t \in [0, T]$, arm r_1 at state $\pi_1[t]$ does not collide with arm r_2 at state $\pi_2[t]$. Additionally, the solution quality is evaluated by the makespan under two levels of fidelity:

1. (MC) manipulation cost based makespan;
2. (FC) estimated execution time based makespan.

In MC (manipulation cost) makespan, we assume the manipulation time dominates the execution time, which is often the case in today's systems. MC makespan is defined as the number of *steps* for the rearrangement task. In each step, each robot arm can complete an individual pick-n-place, execute a coordinated handoff, or idle.

In FC (full cost) makespan, solution quality is measured by the estimated complete time based on four parameters: maximum horizontal speed s of the end-effectors, the execution time of each pick (t_g), place (t_r), and handoff (t_h). The details of FC metric and its corresponding heuristic search method is presented in the appendix (Appendix B)

Given the setup, the problem studied in this paper can be summarized as:

Problem 4 (CDR: Collaborative Dual-Arm Rearrangement). *Given feasible arrangements \mathcal{A}_s , \mathcal{A}_g , and makespan metric (MC or FC), determine a collision-free path set Π for \mathcal{R} moving objects from \mathcal{A}_s to \mathcal{A}_g minimizing the makespan T .*

We also investigate two special cases of CDR. On one hand, when $\rho = 1$, $\mathcal{S}(r_1) = \mathcal{S}(r_2) = \mathcal{W}$, which yields to Collaborative Multi-Arm Rearrangement with Full Overlap (CDRF). In this case, handoff is not needed since each robot can execute pick-n-place operations individually inside the workspace. On the other hand, when $\rho = 0$, $\mathcal{S}(r_1) \sqcup \mathcal{S}(r_2) = \mathcal{W}$, which yields to Collaborative Multi-Arm Rearrangement with no Overlap (CDRN).

4.4 Task Scheduling for CDR

In this section, we study the scheduling problem of primitive actions in CDR. A primitive action can be represented by a tuple (r_i, o_j, v) indicating that r_i is tasked to transfer o_j to new status v , where v is one kind of the object status in $\{S, G, H, \mathcal{B}(r_1), \mathcal{B}(r_2)\}$. S , G , H , $\mathcal{B}(r_1)$, and $\mathcal{B}(r_2)$ represent that the object is at the start pose, goal pose, handoff pose, a buffer in $\mathcal{S}(r_1)$, and a buffer in $\mathcal{S}(r_2)$ respectively. For each primitive action a , the schedule provides the starting time and estimated ending time of a . Noting that buffer locations are not determined in the task scheduling process, they are categorized into $\mathcal{B}(r_1)$ and $\mathcal{B}(r_2)$ to indicate the arm that they are reachable by. The buffer allocation is discussed in Section 4.5. Since the scheduling problem only depends on the availability of goal poses and reachability of robot arms to the start and goal poses, the constraints can be fully expressed by the dependency graph. We describe a dependency graph guided heuristic search method for CDR under MC makespan metrics (Subsection 4.4.1). Its variant for FC makespan is shown in the appendix (Appendix B).

4.4.1 Arrangement Space Heuristic Search for CDR in MC Makespan (MCHS)

When the makespan is counted in MC metric, we can assume primitive actions are executed simultaneously in the task scheduling process without loss of generality and the makespan is counted as the number of *action steps* in the schedule. Each action at action step t is scheduled to start at time t and end at time $t + 1$. Similar to the single arm rearrangement problem, we search for a plan by maintaining a search tree in the arrangement state space. Each arrangement state in the tree represents an object arrangement, which can be expressed as a mapping $\mathcal{L} : \mathcal{O} \rightarrow \{S, G, \mathcal{B}(r_1), \mathcal{B}(r_2)\}$. The arrangement state represents a moment when all objects are stably located in the workspace and both arms are empty.

Arrangements are connected by primitive actions of two arms, which consist of one out of the three possible options: (1) individual pick-n-places: one or both arms move objects to poses that are currently collision-free; (2) coordinated pick-n-places: move an object to the goal pose while the other arm tries to clear away the last obstacle at its goal pose, e.g. swapping poses of o_1 and o_2 in Figure 4.1[Left]; (3) a coordinated handoff for an object when its start and goal poses are not both reachable by either arm. We ignore primitive actions that hold an object for more than one action step due to the unnecessary loss of efficiency.

Figure 4.2 shows the flow charts indicating the decision process of generating possible primitive actions in each arrangement state. Figure 4.2[Upper] shows the decision process for r_1 to pick-n-place $o \in \mathcal{O}$ without cooperation with the other arm. That for r_2 is equivalent. Figure 4.2[Middle] shows the decision process for r_1 to manipulate an object $o \in \mathcal{O}$ when only one object o' is blocking the goal pose of o . In this case, two arms cooperate to send o to the goal. That for r_2 is equivalent. Figure 4.2[Below] shows the decision process when an object $o \in \mathcal{O}$ needs handoff. In the process, the availability of goal poses can be checked in the precomputed dependency graph and the reachability of arms is indicated by the object status in the arrangements. Therefore, with the dependency graph, no additional collision-checking is needed in the task scheduling process of CDR.

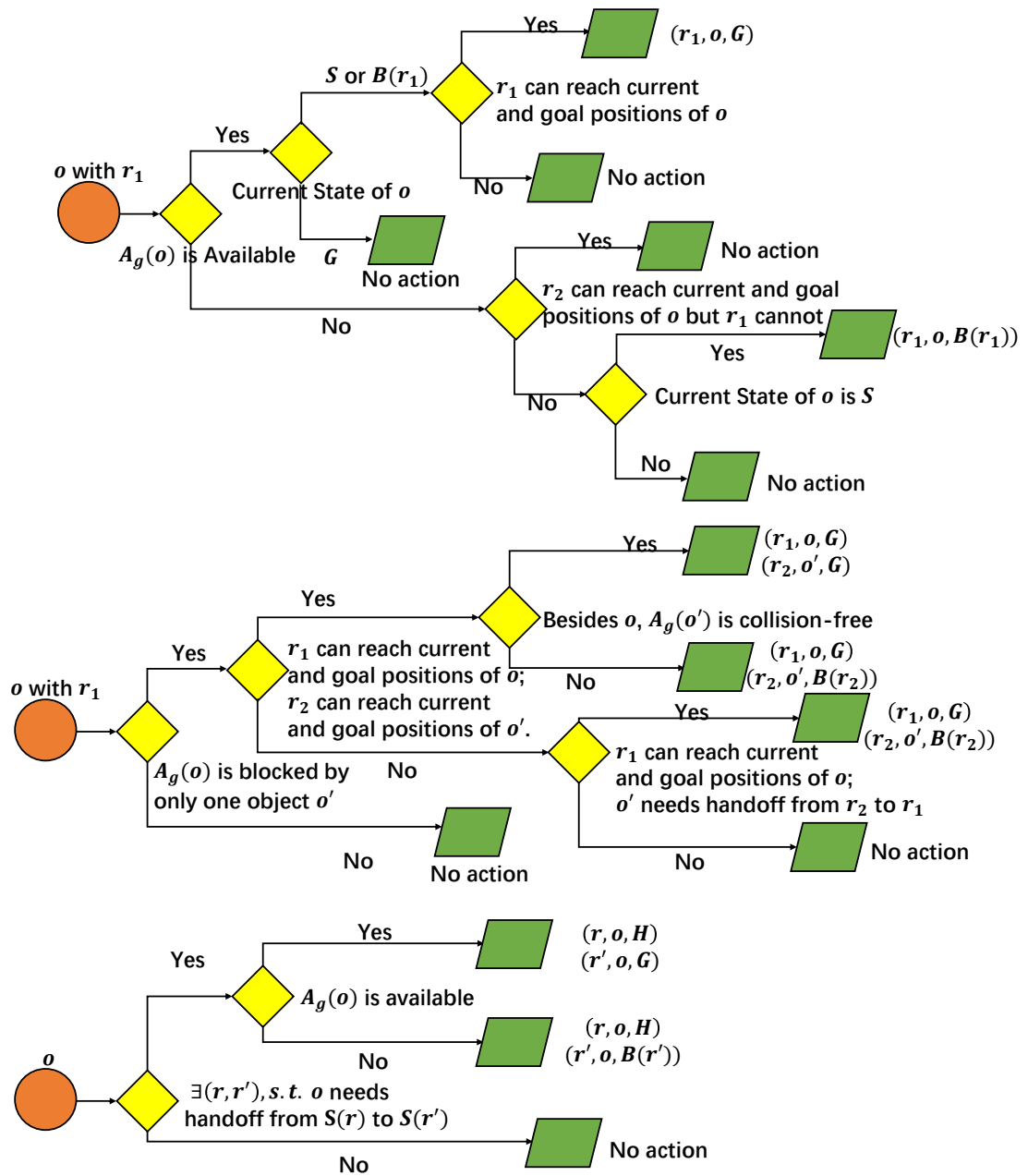


Figure 4.2: Decision process of generating possible primitive actions. [Upper] The decision process for r_1 to manipulate $o \in \mathcal{O}$ without cooperation with the other arm. That for r_2 is equivalent. [Middle] The decision process for r_1 to manipulate an object $o \in \mathcal{O}$ when only one object o' is blocking the goal pose of o . That for r_2 is equivalent. [Bottom] The decision process when an object $o \in \mathcal{O}$ needs handoff.

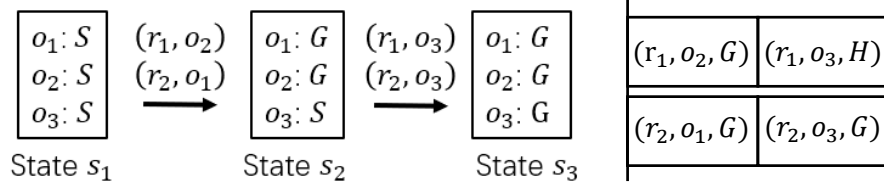


Figure 4.3: [Left] A path on the arrangement state space for the instance in Figure 4.1[Left] under MC metric. [Right] The corresponding schedule of the example instance in Figure 4.1[Left].

For the working example in Figure 4.1[Left], a corresponding rearrangement plan, in the form of a path in the arrangement state space is presented in Figure 4.3[Left]. At the start arrangement state s_1 , r_1 and r_2 move o_2 and o_1 respectively to the goal poses, which yields the next arrangement state s_2 . At s_2 , two arms coordinate to execute a handoff delivering o_3 to the goal and reach the goal arrangement state s_3 . By concatenating primitive actions from s_1 to s_3 , we obtain a corresponding task schedule for the instance (Figure 4.3).

The arrangement state heuristic search based on MC makespan (MCHS) explores the arrangement state space in a best-first manner, always developing the arrangement state s with the lowest $f(s) = g(s) + h(s)$. The g function is number of action steps from the start arrangement state to the current arrangement state. For example, in Figure 4.3, $g(s_3) = 2$. For each state s , we define the heuristic function $h(s)$ based on the needed cost to move all objects directly to goals.

The details are presented in Algorithm 9. In CDR, costs can be either exclusive cost of r_1 , or exclusive cost of r_2 , or shared cost of r_1 and r_2 . For example, on one hand, a pick-n-place in region $\mathcal{S}(r_1) \setminus \mathcal{S}(r_2)$ can only be executed by r_1 , so it leads to an exclusive cost of r_1 . On the other hand, a pick-n-place in the overlapping region $\mathcal{S}(r_1) \cap \mathcal{S}(r_2)$ can be executed by either arm so the cost can be shared by both arms. Based on this observation, we count the costs $\text{cost}[r_1]$, $\text{cost}[r_2]$, and sharedCost in the heuristic and initialize them as 0 (Line 1). We ignore the objects at the goal poses (Line 3). For the remaining objects, the cost category is determined by r_1, r_2 's reachability to the current pose (buffer or start pose) and goal pose of the object. ArmSet is the set of arms able to reach both the current pose

and goal pose (Line 4). If both arms are in `armSet` (Line 5), then the cost of moving o_i to the goal will be added to `sharedCost`, which means that it is a pick-n-place in the overlapping region. If only one arm is in `armSet` (Line 6-7), then the cost of moving o_i to the goal will be added to the cost of the specific arm, which means that this action happens out of reach of the other arm. If neither arm is in `armSet` (Line 8-10), then the object needs a handoff to the destination. In this case, both arms need to take one action for the handoff operation. Finally, on one hand, if the difference of the exclusive costs is smaller than `sharedCost` (Line 11), then $h(s)$ is half of the total cost (Line 12). In other words, the cost of two arms may be balanced by splitting the `sharedCost`. On the other hand, if the difference of the exclusive costs is too large (Line 13), then the unoccupied arm bears all the shared cost, and $h(s)$ equals the cost of the busy arm.

Algorithm 9: Manipulation Cost Search Heuristic

Input : s : current state
Output: h : heuristic value of s

```

1 cost[r1], cost[r2], sharedCost ← 0, 0, 0
2 for  $o_i \in \mathcal{O}$  do
3   if  $\mathcal{L}(o_i)$  is  $G$  then continue;
4   armSet ← ReachableArms( $s, o_i, \{\mathcal{L}(o_i), G\}$ )
5   if armSet is  $\{r_1, r_2\}$  then sharedCost++;
6   else if armSet is  $\{r_1\}$  then cost[r1]++;
7   else if armSet is  $\{r_2\}$  then cost[r2]++;
8   else
9     cost[r1] ++;
10    cost[r2] ++;
11  end
12 end
13 if  $\|cost[r_1] - cost[r_2]\| \leq sharedCost$  then
14  return (cost[r1] + cost[r2] + sharedCost) / 2 ;
15 else return max(cost[r1], cost[r2]) ;
```

Since $cost[r_1]$ and $cost[r_2]$ provide lower bounds of necessary manipulations for each arm, $h(s)$ is a lower bound of the manipulation cost from the state s to the goal arrangement. Therefore, we have:

Proposition 4.4.1. *The manipulation cost based heuristic $h(s)$ is consistent and admissi-*

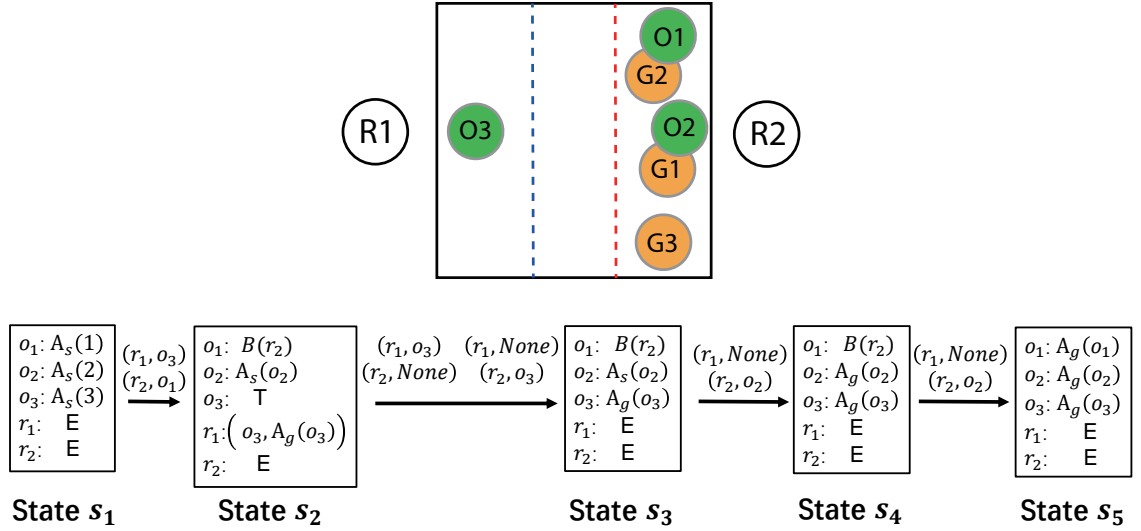


Figure 4.4: [Top] A CDR instance that needs a buffer. [Bottom] An rearrangement plan for the example.

ble.

4.5 Buffer Allocation

In this section, we allocate feasible buffer locations based on the primitive plan computed in Subsection 4.4.1 following the idea of lazy buffer allocation in Chapter 3. Given the primitive plan, we know not only the specific timespans that objects stay in buffers, but also the staying poses of the other objects in the timespans, which are treated as fixed obstacles that the buffer location needs to avoid. Besides the obstacles, the buffer location of an object moved to $\mathcal{B}(r)$ in the primitive plan is restricted to be inside $\mathcal{S}(r)$, the reachable region of r .

We illustrate the buffer allocation process with a CDR instance in Figure 4.4[Top], which is a variant of the example in Figure 4.1[Left]. When o_1 and o_2 are in $\mathcal{S}_2 \setminus \mathcal{S}_1$, at least one of them needs to be moved to buffer locations to break the cycle in the dependency graph. A rearrangement plan is shown in Figure 4.4[Bottom]. In this plan, o_1 is moved to a buffer when o_2 is at $\mathcal{A}_s(o_2)$, and o_3 waits for a handoff. And o_1 leaves the buffer when o_2 and o_3 are both at goal positions. Therefore, the buffer location of o_1 needs to be

collision-free with o_2 at $\mathcal{A}_s(o_2)$, $\mathcal{A}_g(o_2)$ and o_3 at $\mathcal{A}_g(o_3)$. Additionally, it is restricted in $\mathcal{S}(r_2)$. When multiple objects stay in buffers at the same time, the buffer locations need to be allocated disjointedly. In this paper, we search for feasible buffer locations by sampling candidates in the reachable region and check collisions with the fixed obstacles indicated by the primitive plan. The same as TRLB in Chapter 3, when buffer allocation fails, we accept partial plans and conduct a bi-directional search in the arrangement state to connect the start and goal arrangement.

4.6 GPU based Task and Motion Planning in High Dimensional C-Space

4.6.1 MCHS Task Planning

MCHS does not consider the motion planning for the dual-arm system. In reality, robot arms take different times to rearrange a single object and may need to coordinate to avoid collisions in the shared workspace. Using the task plan produced by MCHS, we decouple primitive actions in the plan into lower-level *sub-tasks*. For example, for the primitive action (r_1, o_3) in Figure 4.4, it can be decoupled into four sub-tasks of R_1 : move to pre-handoff pose, move to handoff pose, open gripper, and move back to pre-handoff pose. Even though the original task plan is synchronized (i.e., two robots start and finish individual actions simultaneously in each action step), the generated sub-task sequences allow us to enable asynchronous execution and generate smooth and executable dual-arm motions. The sub-tasks are categorized as follows.

1. A **Traveling Task (TT)** includes motions between home, pre-picking, pre-placing, and pre-handoff poses. A TT sub-task can be represented as (p_1, p_2) , where $p_1, p_2 \in SE(3)$, and the robot needs to move from the current pose p_1 to the target pose p_2 . In our implementation, we also treat idling as a TT sub-task where $p_1 = p_2$.
2. A **Manipulation Task (MT)** includes motions between a picking/placing/handoff pose and its corresponding pre-picking/pre-placing/pre-handoff pose. An MT sub-task can be

represented as (p_1, p_2) , where $p_1, p_2 \in SE(3)$, and the robot needs to move in a straight line from the current pose p_1 to the target pose p_2 .

3. A **Gripper task (GT)** includes opening/closing grippers when picking/placing an object or executing a handoff. A GT task can be represented as (p_1, k) , where the robot arm stays at the current pose p_1 for k timesteps.

4.6.2 Motion Planning Phase

MODAP’s dual-arm motion planning framework is described in Algorithm 10. Each robot executes its sub-tasks sequentially; trajectory conflicts are resolved by leveraging cuRobo’s motion generator. In Line 1, we initialize \mathcal{T} , π_1 , and π_2 , where \mathcal{T} is the dual-arm trajectory, π_1 and π_2 are current sub-tasks of R_1 and R_2 . The rearrangement is finished if all of $\Pi_1, \Pi_2, \pi_1, \pi_2$ are empty (Line 2). In Line 3, π_1 and π_2 are updated. Specifically, if the current sub-task is finished, the next sub-task in the sequence kicks in. Given π_1, π_2 , single-arm trajectories τ_1, τ_2 are computed (Line 4-5). τ_1 and τ_2 avoid self-collisions and collisions between the planning robot arm and the workspace, but they don’t consider collisions between arms. If there is no collision between τ_1 and τ_2 , a dual-arm trajectory is generated by merging τ_1 and τ_2 until one of the trajectories reaches its ending timestep (Line 7). Otherwise, there are two cases (Line 8 - 12): (1) both trajectories can be replanned (Line 8-10); (2) only one trajectory can be replanned (Line 11-12). For (1), we sample a collision-free dual-arm goal configuration q^* (Line 9). At q^* , one robot finishes this sub-task while the other is on its way. And then, we compute dual-arm trajectory via cuRobo (Line 10) from the current dual-configuration to q^* . For (2), we compute a dual-arm trajectory that prioritizes the sub-task of one arm, and the other arm yields as needed. (Line 11-12). The details of our planner for the two cases are described in Subsection 4.6.5. A third case beyond (1) and (2) exists in theory where neither of the trajectories can be replanned. We avoid this case by providing additional clearance for collision checking. A small clearance is enough since non-TT sub-task trajectories are short (a few centimeters). The planner computes a

dual-arm trajectory τ , sped up by Toppra[102], a time-optimal path parametrization solver, and added to \mathcal{T} (Line 13).

Algorithm 10: Fast Dual-Arm Motion Planning

Input : $\{\Pi_1, \Pi_2\}$: sub-task sequences
Output: \mathcal{T} : dual-arm motion

```

1  $\mathcal{T} \leftarrow \emptyset$ ;  $\pi_1, \pi_2 \leftarrow \emptyset, \emptyset$ ;
2 while not Finished( $\Pi_1, \Pi_2, \pi_1, \pi_2$ ) do
3    $\pi_1, \pi_2 \leftarrow \text{UpdateSubTasks}(\Pi_1, \Pi_2, \pi_1, \pi_2)$ ;
4    $\tau_1 \leftarrow \text{SingleArmPlanning}(\pi_1)$ ;
5    $\tau_2 \leftarrow \text{SingleArmPlanning}(\pi_2)$ ;
6   if not InCollision( $\tau_1, \tau_2$ ) then
7      $\tau \leftarrow \text{MergeTraj}(\tau_1, \tau_2)$ ;
8   end
9   else if  $\pi_1$  is TT and  $\pi_2$  is TT then
10     $q^* \leftarrow \text{SampleDualGoal}(\tau_1, \tau_2)$ ;
11     $\tau \leftarrow \text{DualArmPlanning}(q^*)$ ;
12  end
13  else if  $\pi_1$  not TT then  $\tau \leftarrow \text{PlanPartialPath}(\tau_1)$  ;
14  else if  $\pi_2$  not TT then  $\tau \leftarrow \text{PartrialPlanning}(\tau_2)$  ;
15   $\tau \leftarrow \text{ToppraImprovement}(\tau)$ ;  $\mathcal{T} \leftarrow \mathcal{T} + \tau$ 
16 end
17 return  $\mathcal{T}$ ;
```

4.6.3 Enhancing Inverse Kinematic (IK) Solutions

Given the goal end-effector pose p_2 , cuRobo motion generator will sample IK seeds and compute multiple IK solutions of p_2 . However, it may lead to undesired IK solutions of p_2 . For example, in IK computation for pre-picking poses, cuRobo may select a solution where the elbow is positioned below the end effector, preventing the robot from executing the subsequent grasping. We overcame issues caused by undesirable IK solutions by dictating IK seeds. The goal pose's seed is set to the current configuration for MT tasks because we want the target configuration to be close. The current configuration may be too far from the target configuration for TT tasks, leading to the undesired configuration mentioned above. Therefore, in TT tasks, the seed is set to a specific configuration with its corresponding end-effector pose 30 cm above its reachable workspace region as shown in Figure 4.5.

4.6.4 Improving Path Planning to Avoid Detours

cuRobo’s geometric (path) planner samples graph nodes around the straight line between the start, goal, and home (retract) configurations. Based on these nodes, seed trajectories are planned via graph search. When the planning problem is challenging (e.g., the second arm blocks the straight line between the start and goal configurations for the first arm), the computed trajectories tend to make lengthy detours by detouring through the neighborhood of the home configuration, which wastes time and yields unnatural robot paths. This is especially problematic when solving many rearrangement sub-tasks. We improve seed trajectory quality for each arm by uniformly sampling 32 overhead poses above the workspace. The corresponding IK solutions of these manipulation-related poses form 1024 dual-arm configurations, among which the collision-free configurations are added to the geometric graph. This approach proves to be highly effective in avoiding unnecessary detours.

4.6.5 Strategies to Resolve Dual-Arm Trajectory Conflicts

Two arms must coordinate to resolve conflicts and progress toward their next sub-tasks when collisions exist between individual trajectories. As mentioned in Algorithm 10, there are two different collision scenarios. In the first, when both robots have TT sub-tasks, neither has a specific trajectory to follow. In this scenario, we sample a collision-free dual-arm configuration (Algorithm 11) and plan a trajectory from the current configuration to the sampled configuration. In the second, when one of the robots has a specific trajectory to follow, the other arm needs to plan a trajectory to avoid collision. Since cuRobo does not support planning among dynamic obstacles, we propose an algorithm, PlanPartialPath (Algorithm 12), to resolve conflicts. The details of the algorithms are elaborated on in the following sections.

4.6.5.1 Dual-arm goal sampling

Algorithm 11 takes single arm trajectories τ_1 and τ_2 as input and outputs the collision-free dual-arm configuration q . Without loss of generality, we assume τ_1 is the shorter trajectory in time dimension. Usually, this means that the sub-task goal configuration of R_1 is closer to the current configuration. Therefore, we sample a configuration as the goal configuration to the dual-arm motion planning problem, where R_1 reaches the sub-task goal configuration while R_2 progresses toward its goal configuration. In Lines 1-2, we let q_1^* be the sub-task goal configuration of R_1 and q_2^* be the configuration in τ_2 when R_1 reaches q_1^* . If the dual-arm configuration (q_1^*, q_2^*) is collision-free, then we output the configuration (Line 3). Otherwise, we sample the configuration of R_2 in the neighborhood of q_2^* (Line 5-11). The sampling starts with the γ_0 -sphere centered at q_2^* and the range is constantly expanded to a γ_n -sphere, where γ_0 and γ_n are constants. When local sampling fails, we let R_2 yield to R_1 by sampling R_2 configurations on the straight line between its current configuration and its home configuration since the home configuration is guaranteed to be collision-free with the other arm. Let S_2 be the discretization (with k_2 waypoints and k_2 is a constant) of the straight-line trajectory between the current configuration of R_2 and the home configuration of R_2 (Line 12). We then find the collision-free waypoint of R_2 nearest the current configuration and return the corresponding dual-arm configuration (Line 13-15).

4.6.5.2 Priority based planning

In Algorithm 12, we compute a collision-free dual-arm trajectory when one of the robots has a pre-defined trajectory to follow. Without loss of generality, we assume R_1 has a pre-defined trajectory τ_1 to execute while R_2 needs to yield. We first compute a collision-free trajectory τ_2 for R_2 from the current configuration to its home configuration assuming R_1 is fixed at the current configuration (Line 2). In the worst case, it allows R_1 to execute its pre-defined trajectory τ_1 after R_2 moves back to its home configuration. In Line 3-9, we

Algorithm 11: SampleDualGoal

Input : τ_1 : shorter single-arm trajectory, τ_2 : longer single-arm trajectory, $k_1, k_2, \gamma_0, \gamma_n$: hyper-parameters

Output: q : collision-free dual-arm configuration

- 1 $q_1^* \leftarrow$ Ending configuration of τ_1 ;
- 2 $q_2^* \leftarrow$ configuration of τ_2 when τ_1 ends;
- 3 **if** $\text{CollisionFree}(q_1^*, q_2^*)$ **then** **return** $\text{Merge}(q_1^*, q_2^*)$; ;
- 4 **else**
- 5 $r = \gamma_0$;
- 6 **while** $r < \gamma_n$ **do**
- 7 **for** $i = 1$ to k_1 **do**
- 8 $q_2 \leftarrow$ Sample configuration in the r -sphere of q_2^* ;
- 9 **if** $\text{CollisionFree}(q_1^*, q_2)$ **then**
- 10 **return** $\text{Merge}(q_1^*, q_2)$
- 11 **end**
- 12 **end**
- 13 $r \leftarrow 2r$;
- 14 **end**
- 15 $S_2 \leftarrow k_2$ -discretization of the straight line between the start of τ_2 and robot home configuration;
- 16 **for** $q_2 \in S_2$ **do**
- 17 **if** $\text{CollisionFree}(q_1^*, q_2)$ **then**
- 18 **return** $\text{Merge}(q_1^*, q_2)$
- 19 **end**
- 20 **end**
- 21 **end**

progress on executing τ_1 and R_2 yields along τ_2 as needed. $\tau_1[i_1]$ is the next configuration of R_1 on τ . In Line 5, we compute the first index i'_2 such that $i'_2 \geq i_2$ and $\tau_2[i'_2 :]$ is collision-free with $\tau_1[i_1]$. Therefore, $\tau_2[i_2], \dots, \tau_2[i'_2 - 1]$ is collision-free with $\tau_1[i_1 - 1]$, and $\tau_2[i'_2]$ is collision-free with $\tau_1[i_1]$. We add the collision-free dual-arm configurations to τ (Line 6-7) and update indices i_1 and i_2 (Line 8). To summarize, if R_2 blocks τ_1 , then R_2 yields along τ_2 as needed; otherwise, R_2 stays.

Algorithm 12: PlanPartialPath

Input : τ_1 : pre-defined trajectory
Output: τ : dual arm trajectory

- 1 $\tau \leftarrow \emptyset$;
- 2 $\tau_2 \leftarrow$ Motion planning between the current configuration and home configuration of R_2
 while R_1 stays at the current configuration;
- 3 $i_1, i_2 \leftarrow 0, 0$;
- 4 **while** $i_1 < |\tau_1|$ **do**
- 5 $i'_2 \leftarrow$ CollisionFreeFirstIndx($\tau_1[i_1], \tau_2[i_2 :]$);
- 6 $\tau \leftarrow \tau.$ Extend($\tau_1[i_1 - 1], [\tau_2[i_2], \dots, \tau_2[i'_2 - 1]]$);
- 7 $\tau \leftarrow \tau.$ Extend($\tau_1[i_1], [\tau_2[i'_2]]$);
- 8 $i_1 + = 1; i_2 = i'_2$;
- 9 **end**
- 10 **return** τ ;

4.6.6 Real2Sim2Real

Solving CDR mainly involves computing solutions, simulating them, and transferring them to real robot systems. To apply MODAP to real robot systems, however, requires us first to build an accurate model (digital twin) of the actual system. To achieve this, we calibrate the robots relative to each other by placing them (at different times) at the same seven diverse positions in the workspace alternately. This allows us to compute an accurate transformation between the two robot arms, upon which a digital twin of the actual setup is obtained. All the objects to be manipulated are labeled with ArUco markers[103], and we can directly transfer their positions into the simulation with a calibrated camera.

Since the two real robot arms are calibrated and their positions are transferred into the simulation, the trajectories planned in simulations can be seamlessly transferred to the real

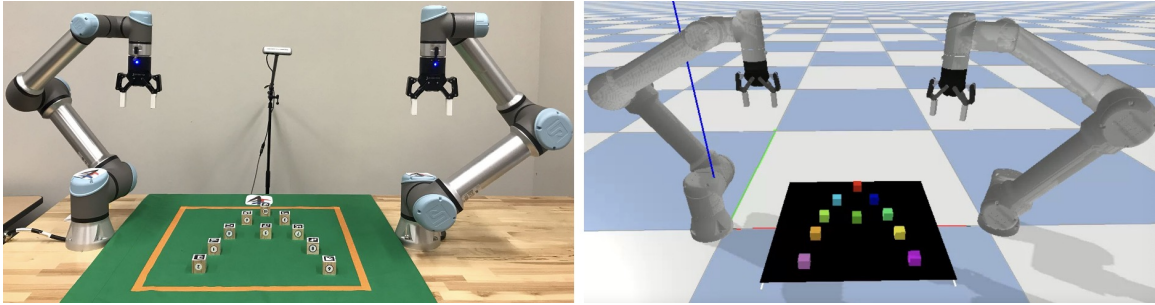


Figure 4.5: [left] A configuration of our dual-arm setup, also showing that the camera is mounted at the side to detect objects' poses. [right] The corresponding Dual-Arm setup in pyBullet simulation.

robot system and executed directly without further post-processing. Figure 4.5 shows that our real and simulated setups mirror each other.

4.6.7 Real Robot Control

The open-source Python library `ur_rtde`[104] is used to communicate with and control the robot, which allows us to receive robot pose/configuration and send control signals in real-time (up to 500Hz). Our controller sends joint positions for continuous control via the `ServoJ()` function, a PD-styled controller. The control signals are sent out alternatively at every cycle (e.g., with a 0.002-second interval), and synchronized between the two arms.

4.7 Experimental Results

4.7.1 Task Planning Evaluation

To evaluate the effectiveness of our dual-arm task planning algorithms, we integrate them with a simple priority-based motion planner. Essentially, in the presence of potential arm-arm conflict in the workspace, the motion planner will give the arm that is moving first priority while the second arm yields. The yielding arm will either take a detour to the target pose or go back to the rest pose and wait for the execution of the other arm. We make this choice, instead of using more sophisticated sampling-based asymptotically optimal planners, to highlight the benefit of our task planner.

The proposed algorithms are implemented in Python; we choose objects to be uniform cylinders. In each instance, robot arms move objects from a randomly sampled start arrangement (see, e.g., Figure 4.6). Besides different overlap ratios ρ , we test our algorithms in environments with different density levels D , defined as the proportion of the tabletop surface occupied by objects, i.e., $D := (\sum_{o_i \in \mathcal{O}} S_{o_i}) / S_{\mathcal{W}}$, where S_{o_i} is the base area of o_i and $S_{\mathcal{W}}$ is the area of \mathcal{W} . The computed rearrangement plans are executed in PyBullet with UR-5e robot arms.

For the FC makespan, we propose an interval state space heuristic search algorithm (FCHS) in Appendix B. In experiments, we let the execution time of a pick t_g , a place t_r , and a handoff t_h equal to the time spent for an arm traveling across the diameter of the workspace t_d , i.e. $t_g = t_r = t_h = t_d$. This setting mimics general manipulation scenarios in the industry, where a successful pick-n-place relies on accurate pose estimation of the target object, a careful picking to firmly hold the object, and a careful placing to stabilize the object at the desired pose. The experiments are executed on an Intel[®] Xeon[®] CPU at 3.00GHz. Each data point is the average of 20 test cases except for unfinished trials, if any, given a time limit of 300 seconds for each test case.

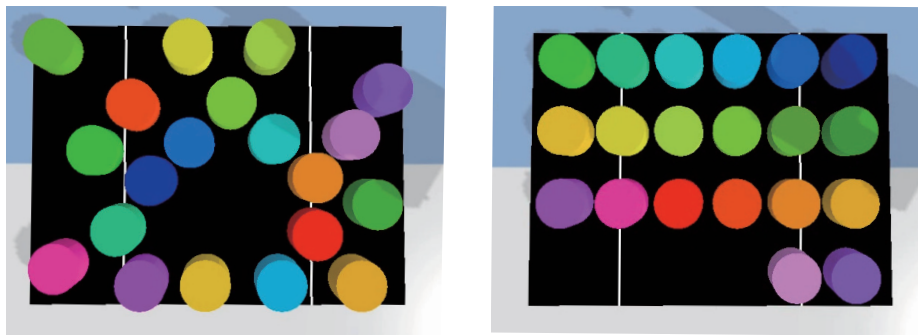


Figure 4.6: A 20-cylinder example of rearrangement instance with $D = 0.4$ and $\rho = 0.5$, moving object from a randomly sampled start arrangement [Left], to an organized goal arrangement [Right].

Manipulation versus Full Cost as Proxies. In Figure 4.7, we first compare optimal task schedules in both MC and FC makespans in instances with $\rho = 0.5$, $D = 0.3$. While FCHS shows slight advantage in actual execution time, it incurs significantly more com-

putation time and is more prone to planning failure. The results suggest that MC is more suitable as a proxy for optimizing CDR planning process. We also compare the execution time of MC-optimal and FC-optimal plans in instances under different density levels and overlap ratios and observe similar outcome. Based on the observation, for later experiments, MCHS is used exclusively.

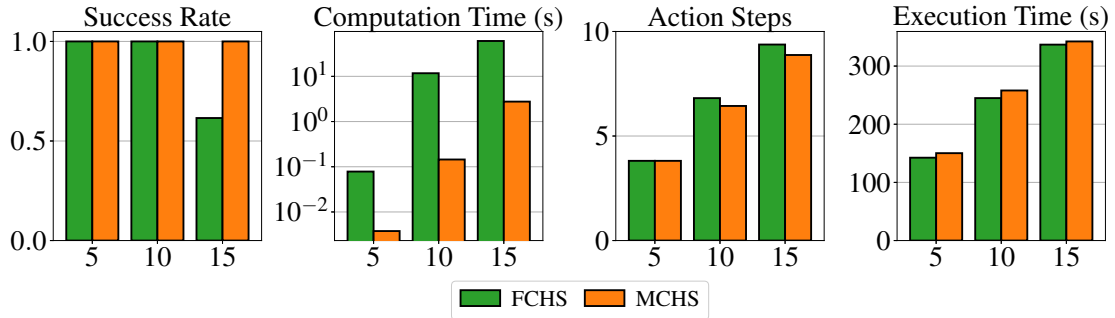


Figure 4.7: Performance of FCHS and MCHS in instances with $\rho = 0.5$, $D = 0.3$. The x-axis represents the number of objects.

Comparison with Baselines. We compare the proposed algorithms with two baseline methods:

1. *Single-MCHS-Split*: A schedule of primitive actions for a single arm is first computed, minimizing the MC makespan, i.e. the total number of actions. Then, the tasks are assigned to the two arms as evenly as possible. A handoff is coordinated if the manipulating object is moving between $\mathcal{S}(r_1)$ and $\mathcal{S}(r_2)$.
2. *Greedy*: Each arm prioritizes the manipulations moving objects from buffers to goals. When there is no such manipulation available, the arm will choose the object closest to the current end-effector position.

In Figure 4.8, we compare MCHS to the baseline algorithms in the environments with $\rho = 0.5$ and different density levels D . Comparing with Single-MCHS-Split, MCHS saves up to 10% execution time, which is fairly significant for logistic applications. We note that Single-MCHS-Split, guided by dependency graph, already performs quite well in dense

environments. The execution time gap comes from failures in coordinating Single-MCHS-Split plans, e.g. an arm idles for a few action steps waiting for a handoff or an arm holds an object for a few action steps waiting for obstacle clearance. Comparing with the greedy method, MCHS saves more execution time as D increases. Specifically, in 20-cylinder instances with $D = 0.4$, the execution time of MCHS plans is 35% shorter than greedy plans. Without a long-term plan in mind, greedy planning incurs more temporary object displacements.

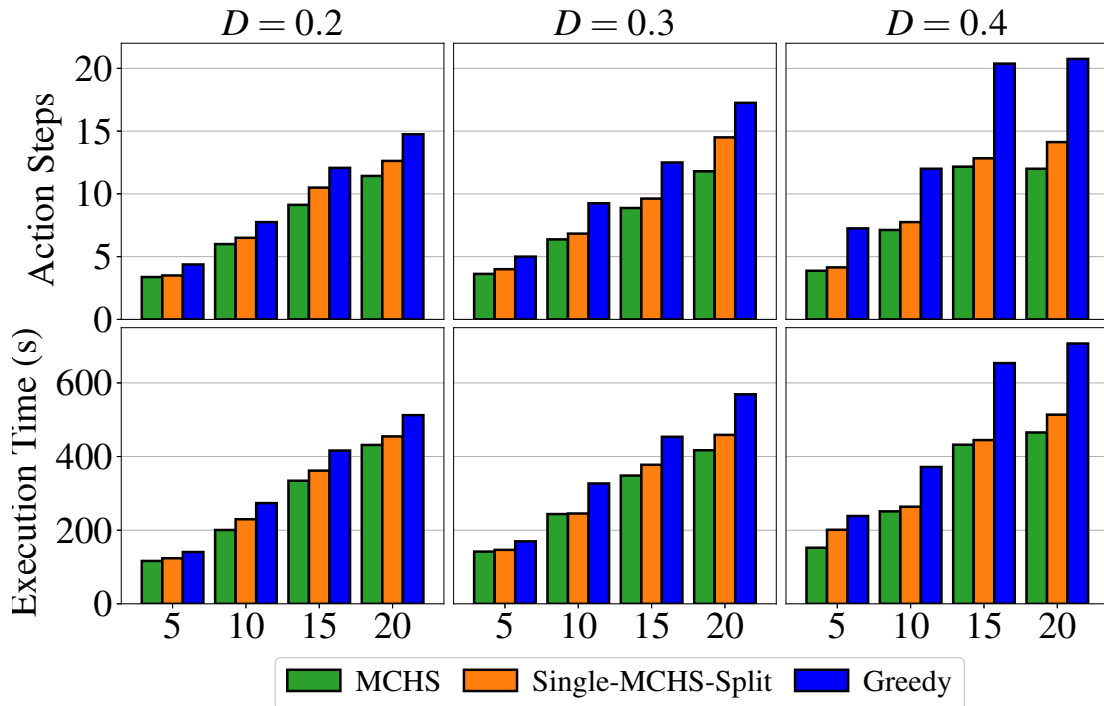


Figure 4.8: Algorithm comparison in environments with different density levels D . The x-axis represents the number of objects.

In instances with $D = 0.3$, we also evaluate the tendency of the makespan and execution time as ρ varies. The conflict proportion shows the proportion of execution time for an arm to yield to the other arm during the execution. The results are shown in Figure 4.9. As ρ increases, the shared area of robot arms expands. On one hand, the number of objects that need handoffs decreases. So does the number of action steps in the schedule. On the other hand, we see an increase of path conflicts. In instances with larger ρ , robot arms spend more time on yielding. Based on the two factors, there is a shallow “U” shape in execution

time as ρ increases.



Figure 4.9: Evaluation of instances with different ρ . The x-axis represents the number of objects.

Fully Overlapping Workspaces. MCHS can also compute CDR plans with full overlap (CDRF), i.e., $\rho = 1.0$. As shown in Figure 4.10, due to the reachability limit of UR-5e, the workspace is a bounded square with sides of length $0.6m$. In this case, each arm can reach every corner of the workspace but its manipulation is likely to be blocked by the other arm. We compare dual-arm MCHS plans to the single-arm MCHS plans, where r_1 take responsibility of all rearrangement tasks and the number of total actions is minimized. The results (Figure 4.11) indicate that each arm in the dual-arm system spends around 18% of execution time yielding or making detours due to the blockage of the other arm. Therefore, even though MCHS saves 50% action steps, the execution of the plans is only around 10% faster than that of the single-arm rearrangement plans. However, the efficiency gain shown in action steps also suggests that the dual-arm system has the potential to save up to half of the execution time with specially designed arms for CDRF problems.

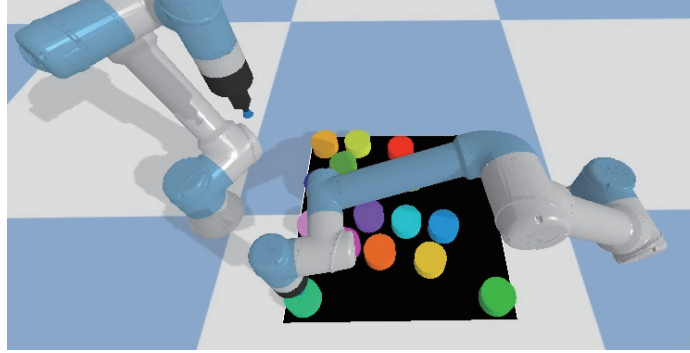


Figure 4.10: An instance of CDR with full overlap (CDRF), where each arm can reach every corner of the workspace but its manipulation is likely to be blocked by the other arm.

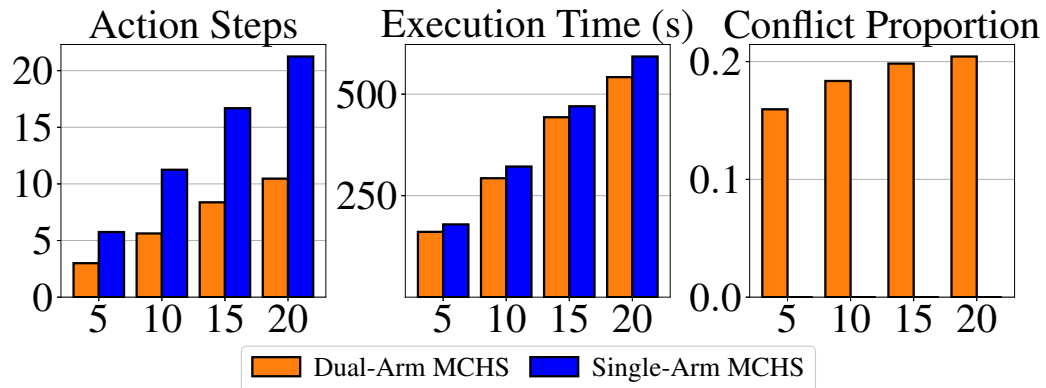


Figure 4.11: Algorithm performance in CDR instances with $\rho = 1.0$. The x-axis represents the number of objects.

4.7.2 Motion Planning Evaluation

In this section, we evaluate our MODAP and compare it with two baseline planners both in simulation and on real robots. The two baseline planners are:

1. **Baseline (BL)** Similar to MODAP, BL computes collision-free dual-arm motion plans based on MCHS task plans. When the clearance between robots is larger than a certain threshold, both arms execute their tasks individually. Otherwise, one arm yields by moving toward its home state, which is guaranteed to be collision-free. After obtaining a collision-free initial trajectory, BL smoothens the yielding trajectories: instead of switching frequently between yielding and moving toward the next target, the robot attempts to move back to a collision-free state and waits until the conflict is resolved.

2. **Baseline+Toppra (BL-TP)** BL-TP uses Toppra to speed up the trajectory planned by BL.

4.7.3 Sim2Real Gap: Trajectory Tracking Accuracy

Whereas we must evaluate plans on real robots to ensure they work in the real world, doing so extensively prevents us from running a large number of experiments as it is time-consuming to set up and run real robots. To that end, we first evaluate the sim2real gap of our system. The Root-Mean-Square Deviation(RMSD) is introduced as a metric to evaluate the accuracy of the real robot control for one waypoint q_i in the planned trajectory τ

$$RMSD(q_i) = \sqrt{\frac{(\hat{q}_i - q_i)^T (\hat{q}_i - q_i)}{|q_i|}}$$

where \hat{q}_i denotes the real configuration retrieved from the robot while executing the control signal q_i and $|q_i|$ denotes the degree of freedom of the robot system. The control quality of a trajectory can be evaluated as

$$Q(\tau) = \mathbb{E}[RMSD(q_i)]$$

Trajectories are collected from 5 different scenes with four randomly placed cubes as the start and goal, planned by different methods, and then executed in simulation and real-world at different speed limits. In the meantime, RMSD and Q for the end-effector position can be recorded. In Figure 4.12[top], we show the RMSD of the configuration and the end effector's position on each waypoint in a trajectory planned using MODAP. We observe that we can see that the execution error is about 1° for each joint and 5mm as the end-effector position is concerned, executing at a speed of 1.57rad/s at every joint. Figure 4.12[bottom] shows the average configuration Q value of 5 trajectories executed at different speed limits. First, we note that trajectory execution is perfect in simulation, as expected. We observed that MODAP induces a slightly larger (though perfectly acceptable) execution error than BL and BL-TP. This is due to trajectories produced by MODAP running at faster overall speeds.

Overall, our evaluation of the trajectory tracking accuracy indicates that the sim2real gap is negligibly small across the methods, including MODAP. This suggests we can confidently plan in simulation and expect the planned time-parameterized trajectory to execute as expected on the real system. It also means that we can compare the optimality of the methods using simulation, which we perform next.

4.7.4 Performance on Rearrangement Plans Execution

In evaluating the performance of MODAP and comparing that with the baseline methods, we first examine the execution of MODAP, BL, and BL-TP on a typical instance involving the rearrangement of five objects with $\rho = 1.0$ (full workspace overlap). The time-parameterized trajectories of the six robot joints are plotted in Figure 4.13 for all three methods. We can readily observe that MODAP is much more time-efficient than BL and BL-TP. We can also readily observe the reason behind this: BL has one arm idling in most of the execution due to inefficient dual-arm coordination. After Toppra acceleration, BL-TP is still 32% slower than MODAP.

Figure 4.14 shows the result of a full-scale performance evaluation under three overlapping ratios ($\rho = 0.5, 0.75, 1$) and different numbers of objects to be rearranged ranging between 6-18. The simulation experiments are executed on an Intel[®] Core(TM) i7-9700K CPU at 3.60GHz and an NVIDIA GeForce RTX 2080 Ti GPU for cuRobo planner. For each method, the average execution time and total trajectory length are given; each data point (with both mean and standard deviation) is computed over 20 randomly generated instances. Two example test cases are shown in Figure 4.15. We set the maximum per-instance computation time allowance to be 500 seconds, sufficient for all computations to complete. MODAP, exploring many more trajectories than BL and BL-TP, takes, on average, 2-3 times more computation time. The total length is the sum of robot trajectory lengths computed under the L2 norm in the 6-DoF robot’s configuration space. We observe that MODAP’s plans can be executed faster than BL and BL-TP even though cuRobo generates

longer trajectories, which aligns with the observation based on Figure 4.13. When $\rho = 0.5$, MODAP saves 13% – 32% execution time compared with BL, and 3% – 30% compared with BL-TP. When $\rho = 1.0$, MODAP saves 29% – 44% execution time compared with BL, and 11% – 40% compared with BL-TP. MODAP shows apparent efficiency gain as the overlap ratio ρ increases, which shows that the proposed MODAP effectively resolves conflicts between robot trajectories.

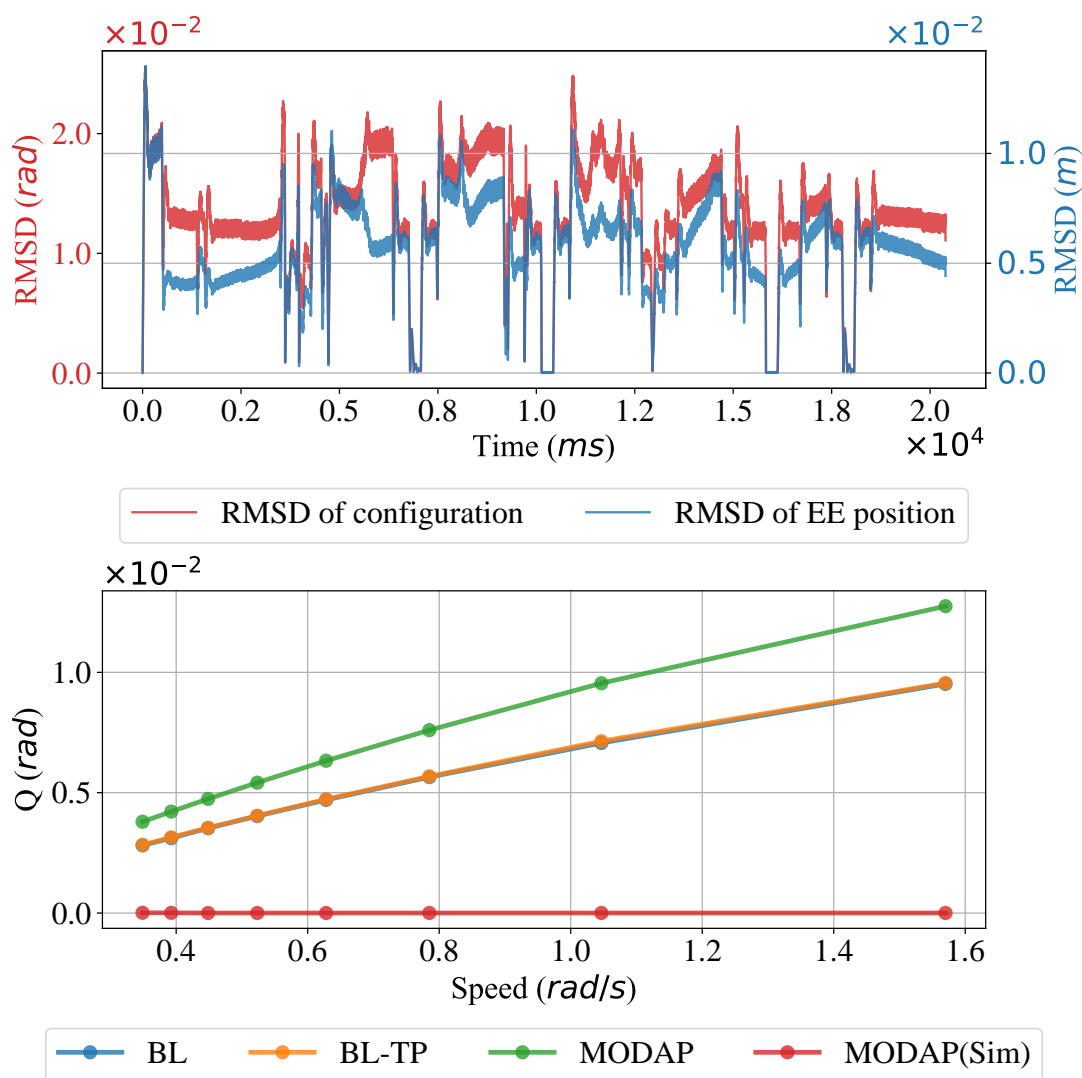


Figure 4.12: [top] RMSD of configuration and end-effector position on a sampled trajectory executed with a maximum speed of 1.57rad/s on real robots. [bottom] The average Q value of 5 sampled trajectories executed at different maximum speeds (sim denotes execution in simulation; otherwise, the execution is on a real robot). Note that the lines of BL and BL-TP overlap with each other.

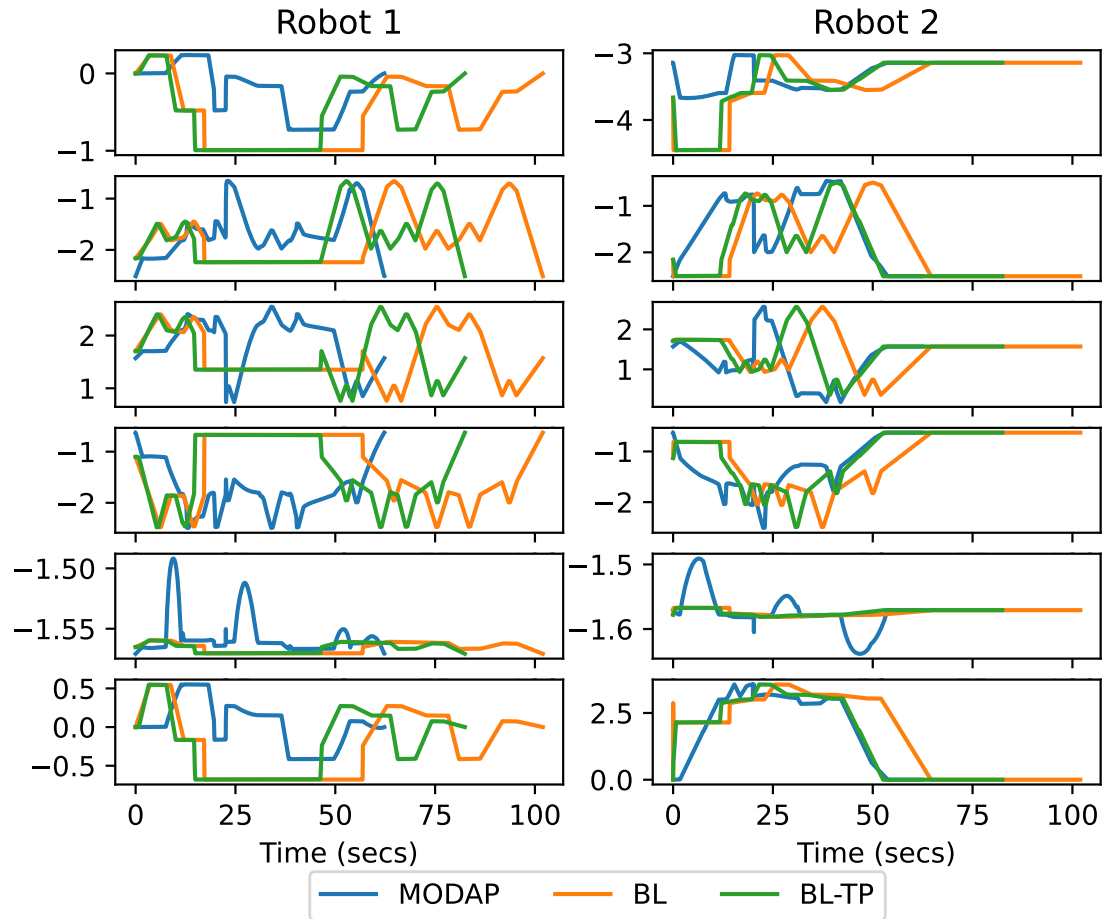


Figure 4.13: Trajectories of BL, BL-TP, and MODAP for the a typical rearrangement task. Each row, from top to bottom, corresponds to a robot joint in radians from one to six. Each column shows the trajectory of the six joint angles of a robot.

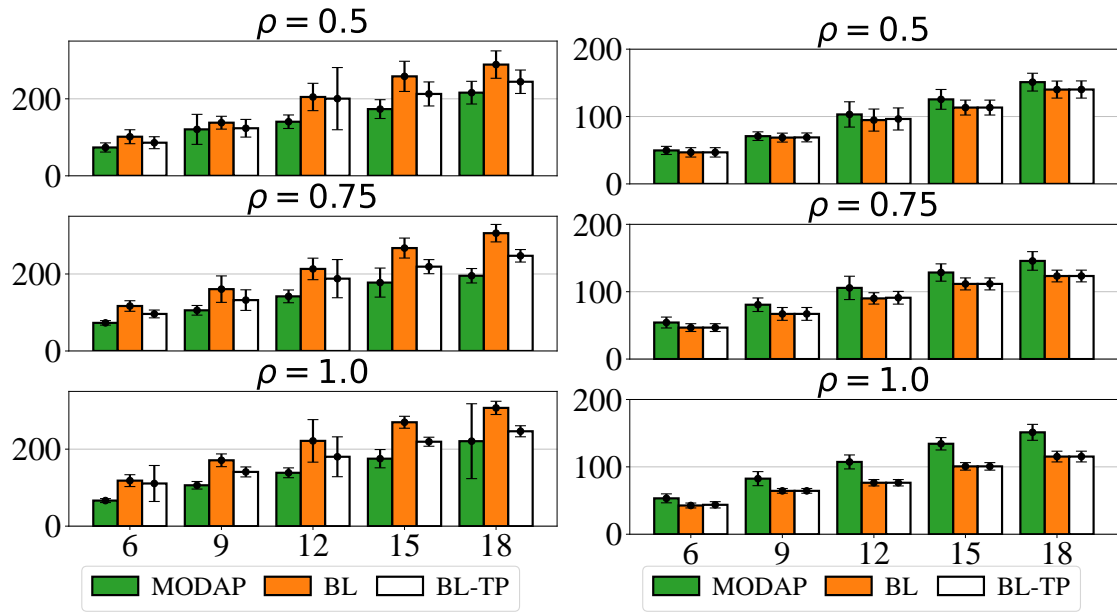


Figure 4.14: Average execution time (left) and trajectory total length (right) computed by compared methods under different overlap ratios ρ and the number of workspace objects.

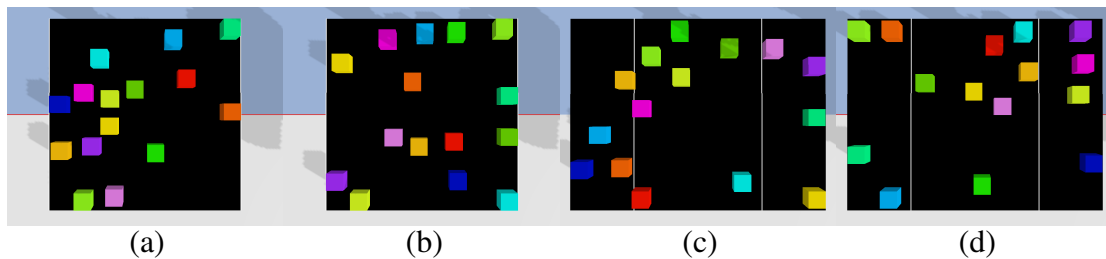


Figure 4.15: Two examples of start and goal configurations with 15 objects at overlap rates $\rho = 1$ (a, b) and $\rho = 0.5$ (c, d). (a) and (c) (resp., (b) and (d)) are starting (resp., goal) configurations.

CHAPTER 5

DISTANCE-OPTIMAL TRLB: OBJECT REARRANGEMENT WITH LAZY A*

5.1 Motivation

Effectively performing object rearrangement is an essential skill for mobile manipulators, e.g., setting up a dinner table. A key challenge in such problems is deciding an appropriate ordering to effectively untangle object-object dependencies while considering the necessary motions for realizing the manipulations (e.g., pick and place). To our knowledge, computing time-optimal multi-object rearrangement solutions for mobile manipulators remains a largely untapped research direction. This study develops effective solutions for mobile manipulators over a larger workspace and jointly considers the arrangement’s stability.

To that end, this chapter proposes ORLA*: *Object Rearrangement with Lazy A** for solving mobile manipulator-based rearrangement tasks. This study carefully investigated factors impacting the optimality of a rearrangement plan for mobile manipulators and provided insightful structural understandings for the same. Among these, a particularly interesting one is that the mobile base travels on S^1 (i.e., a cycle), leading to intricate interactions with other factors in the optimization task. ORLA* designs a suitable cost function that integrates the multiple costs and employs the idea of lazy buffer allocation (buffers are temporary locations for objects that cannot be placed at their goals) into the A* framework to search for rearrangement plans minimizing the cost function. To accomplish this, the f, g, h values in A* are redefined when some states in the search tree are non-deterministic due to the delayed buffer computation. With optimal buffer computation, ORLA* returns globally optimal solutions. A thorough feasibility and optimality study backs our buffer allocation strategies. To estimate the feasibility of a buffer pose, especially when an object

needs to be placed on top of others temporarily, a learning model, StabilNet, is proposed to estimate the stability of the placing pose.

5.2 Related Work

Tabletop Rearrangement In tabletop rearrangement tasks, the primary challenge lies in planning a long sequence of actions in a cluttered environment. Such rearrangement planning can be broadly divided into three primary categories: prehensile[105, 106, 1, 107, 92, 81, 108, 109], non-prehensile[110, 44, 80, 111, 43], and a combination of the two[112]. Compared with non-prehensile operations (e.g., pushing and poking), prehensile manipulations, while demanding more precise grasping poses[105] prior to picking, offer the advantage of placing objects with higher accuracy in desired positions and facilitate planning over longer horizons[49]. In this domain, commonly employed cost functions encompass metrics like the total count of actions[92, 106, 109], execution duration[49], and end-effector travel[1, 111], among others[113]. In this paper, we manipulate objects with overhand pick-n-places. Besides end-effector traveling costs, we also propose a novel cost function considering the traveling cost of a mobile robot.

Buffer Allocation In the realm of rearrangement problems, there are instances where specific objects cannot be moved directly to their intended goal poses. These scenarios compel the temporary movement of objects to collision-free poses. To streamline the rearrangement planning, several rearrangement methodologies exploit external free spaces as buffer zones[106, 109]. One notable concept is the *running buffer size*[106], which quantifies the requisite size of this external buffer zone. In situations devoid of external space for relocation, past research either pre-identifies potential buffer candidates[69, 86] or segments the rearrangement tasks into sequential subproblems[47, 28]. TRLB[92], aiming for an optimized buffer selection, prioritizes task sequencing and subsequently employs the task plan to dictate buffer allocation. However, TRLB doesn't factor in travel costs. Contrarily, in our study, we incorporate lazy buffer allocation within the A* search and

prioritize buffer poses based on various cost function optimizations.

Manipulation Stability Structural stability is pivotal in robot manipulation challenges. Wan et al.[114] assess the stability of Tetris blocks by scrutinizing their supporting boundaries. For truss structures, finite element methods have been employed to assess stability of intermediate stages[115, 116]. Utilizing deep learning, Noseworth et. al.[117] introduce a Graph Neural Network model dedicated to evaluating the stability of stacks of cuboid objects. However, these methodologies often come with shape constraints, requiring objects to be in forms such as cuboid blocks or truss structures. For objects of more general shapes, recent research[109, 118] leverages stability checkers grounded in physics simulators, which are effective but tend to be computationally intensive. In contrast, our study introduces a deep-learning-based prediction model, StabilNet, tailored for the rearrangement of objects with diverse shapes. StabilNet offers a speed advantage over simulation-based checks and demonstrates robust generalization to previously unseen object categories.

5.3 Mobile Robot Tabletop Rearrangement

Consider a 2D tabletop workspace centered at the origin of the world coordinate with z pointing up. A point (x, y, z) is within the tabletop region \mathcal{W} if (x, y) are contained in the workspace and $z \geq 0$. The workspace has n objects \mathcal{O} . The pose of a workspace object $o_i \in \mathcal{O}$ is represented as (x, y, z, θ) . An arrangement of \mathcal{O} is feasible if all objects are contained in the tabletop region and are collision-free. In this paper, we allow objects to be placed on top of others. An object is *graspable* at this arrangement if no other object is on top. A goal pose is *available* if both conditions below are true: (1). There is no obstacle blocking the pose; (2). If other objects have goal poses under the pose, these objects should have been at the goal poses.

On the table’s edge, a mobile robot equipped with an arm moves objects from an initial arrangement \mathcal{A}_I to a desired goal arrangement \mathcal{A}_G with overhand pick and place actions. Each action a is represented by (o_i, p_1, p_2) , which moves object o_i from current pose p_1 to

a collision-free target pose p_2 . A rearrangement plan $\Pi = \{a_1, a_2, a_3, \dots\}$ is a sequence of actions moving objects from \mathcal{A}_I to \mathcal{A}_G .

We evaluate solution quality with a cost function $J(\Pi)$ (Eq. Equation 5.1), which mimics the execution time of the plan. The first term is the total traveling cost, and the second is the manipulation cost associated with pick-n-places, which is linearly correlated with the number of actions.

$$J(\Pi) = dist(\Pi) + mani(\Pi), \quad mani(\Pi) = C|\Pi| \quad (5.1)$$

Based on the description so far, we define the studied problem as follows.

Problem 5 (Mobile Robot Tabletop Rearrangement (MoTaR)). *Given a feasible initial arrangement \mathcal{A}_I and feasible goal arrangement \mathcal{A}_G of an object set \mathcal{O} , find the rearrangement plan Π minimizing the cost $J(\Pi)$.*

We study MoTaR under two scenarios. On the one hand, for a small workspace (Figure 5.1[Left]), where the mobile robot can reach all tabletop poses at a fixed base position. We define $dist()$ as the Euclidean travel distance of the end effector (EE) in the x-y plane. On the other hand, for a large table workspace(Figure 5.1[Right]), where the mobile base needs to travel around to reach the picking/placing poses, we define $dist()$ as the Euclidean distance that the mobile base (MB) travels. As shown in Figure 5.2[Left], we assume the mobile base travels along the boundaries of the table. When the robot attempts to pick/place an object at pose (x, y, z, θ) , it will move to the closest point on the track to (x, y) before executing the pick/place. In the remainder of this paper, we will refer to the scenarios as *EE* and *MB*, respectively.

5.4 ORLA*: A* with Lazy Buffer Allocation

We describe ORLA*, a *lazy* A*-based rearrangement planner that delays buffer computation, specially designed for mobile manipulator-based object rearrangement problems.

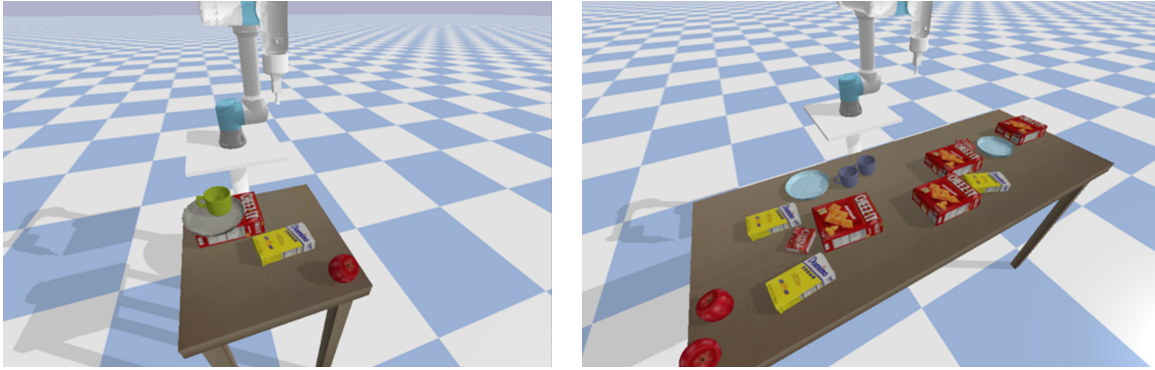


Figure 5.1: [Left] An example of the EE scenario, where the table is small and the robot can reach all poses from a fixed position. We count the traveling cost of the end-effector (EE) in the cost function. [Right] An example of the MB scenario, where the table is large and the robot can only reach a portion of tabletop poses from a fixed position. We count the traveling cost of the mobile base (MB) in the cost function.

As a variant of A*, ORLA* always explores the state s that minimizes the estimated cost $f(s) = g(s) + h(s)$. An action from s to its neighbor moves an object to the goal pose or a buffer. Specifically, actions from s follow the rules below:

1. **R1.** If o_i is graspable and its goal pose is also available at s , move o_i to its goal.
2. **R2.** If o_i is graspable, its goal is unavailable, and it causes another object to violate R1, then move o_i to a buffer.

When ORLA* decides to place an object at a buffer, it does not allocate the buffer pose immediately. Instead, the buffer pose is decided after the object leaves the buffer. In this way, lazy buffer allocation effectively computes high-quality solutions with a low number of actions as shown in Chapter 3. Under the A* framework, ORLA* searches for buffer poses with the minimum additional traveling cost.

5.4.1 Deterministic and Nondeterministic States

To enable lazy buffer allocation, ORLA* categorizes states into deterministic states (DS) and non-deterministic states (NDS). Like traditional A*, a DS represents a feasible object arrangement in the workspace. Each object has a deterministic pose at this state. NDS is a

state where some object is at a buffer pose to be allocated.

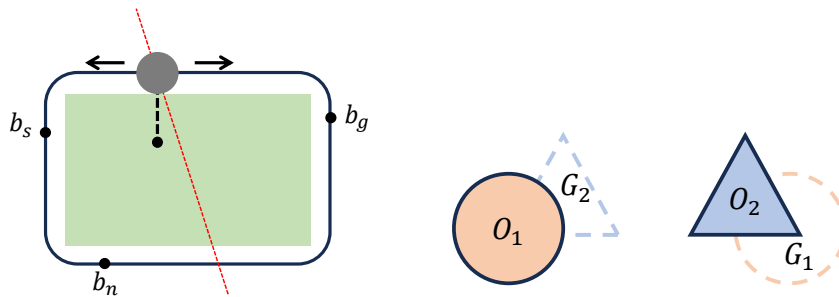


Figure 5.2: [Left] An example of MB scenario, where the robot (gray disc) travels along the green table following the black track along the table boundaries. To pick/place an object on the table, the robot moves to the nearest position before the manipulation. [Right] A working example where o_1 and o_2 block each other's goal pose. One must move to a buffer pose to finish the rearrangement.

In the working example in Figure 5.2[Right], o_1 and o_2 blocks each other from goal poses. The path in the A* search tree from the initial state (p_1^I, p_2^I) to the goal state (p_1^G, p_2^G) may be:

$$S_1 : (p_1^I, p_2^I) \rightarrow S_2 : (B_1, p_2^I) \rightarrow S_3 : (B_1, p_2^G) \rightarrow S_4 : (p_2^G, p_2^G)$$

In this rearrangement plan, the robot moves o_1 to buffer and then moves o_2 and o_1 to goal poses, respectively. In this example, the initial and goal states S_1 and S_4 are DS, and both intermediate states S_2 and S_3 are NDSs since o_1 is at a non-deterministic buffer B_1 in these states.

5.4.2 Cost Estimation

In A*, each state s in the search space is evaluated by $f(s) = g(s) + h(s)$, where $g(s)$ represents the cost from the initial state to s and $h(s)$ represents the estimated cost from s to the goal state. ORLA* defines $g(s)$ and $h(s)$ for DS and define $f(s)$ for NDS. For a DS s_D , $g(s_D)$ is represented by the actual cost measured by $\mathcal{J}(\cdot)$ from the initial state to s_D , which can be computed as follows:

$$g(s_D) = g(s'_D) + \mathcal{J}(s'_D, s_D)$$

where s'_D is the last DS in this path, and $\mathcal{J}(s'_D, s_D)$ is the cost of the path between s'_D and s_D . When there are NDSs between s'_D and s_D , we compute buffer poses minimizing the cost. The details are discussed in Subsection 5.4.3. In $h(s_D)$ computation, we only count the transfer path and manipulation costs of one single pick-n-place for each object away from goal poses. For example, in Figure 5.2, $h(S_1) = \text{dist}(p_1^s, p_1^g) + \text{dist}(p_2^s, p_2^g) + C * |\{o_1, o_2\}|$.

For an NDS s_N , we have

$$f(s_N) = g(s'_D) + \mathcal{J}(s'_D, s_N) + h(s_N) \quad (5.2)$$

Since the $g(x)$ computation of DSs and NDSs only relies on $g(\cdot)$ of S'_D , rather than any NDS, we do not compute $g(s_N)$ explicitly. Instead, we directly compute the lower bound of the actual cost as $f(s_N)$. The general idea of $f(s_N)$ computation is presented in Algorithm 13. In Line 2, we add all manipulation costs in $\mathcal{J}(s'_D, s_N)$ and $h(s_N)$, which are defined in the same spirit as those of s_D . In Lines 3-4, we add the traveling cost along deterministic poses between s'_D and s_N , which is a lower bound of the actual traveling cost as it assumes buffer poses do not induce additional costs. In Lines 5-8, we add traveling cost to $h(s_N)$. If the object is at a buffer, we add traveling distance based on Algorithm 14, which we will mention more details later. If the object is at a deterministic pose, we add the traveling cost of the transfer path between the current pose and its goal pose. In our implementation, we store buffer information in each NDS to avoid repeated computations in Algorithm 13.

Algorithm 14 computes the traveling cost in $f(s_N)$ related to a buffer pose p_b in addition to the straight line path between its neighboring deterministic waypoints (Algorithm 13 Line 3). For an object o_i at a buffer, the related traveling cost involves three deterministic points $\{p_s, p_n, p_g\}$: p_s and p_n are the deterministic poses right before and after visiting the buffer. p_g is the goal pose of o_i . $\text{dist}(p_b, p_s) + \text{dist}(p_b, p_n)$ is in $g(s_N)$ and $\text{dist}(p_b, p_g)$ is

Algorithm 13: $f(s_N)$ Computation

Input : s_N : an NDS state; \mathcal{A}_G : goal arrangement
Output: c : $f(s_N)$

- 1 $c \leftarrow g(s'_D)$
- 2 $c \leftarrow$ Add manipulation costs.
- 3 $P \leftarrow$ All deterministic waypoints from s'_D to s_N .
- 4 $c \leftarrow c + \text{dist}(P)$
- 5 **for** o_i away from goal in s_N **do**
- 6 **if** o_i in buffer **then**
- 7 $c \leftarrow c + \text{distanceRefinement}(s_N, o_i, \mathcal{A}_G)$
- 8 **end**
- 9 **else** $c \leftarrow c + \text{dist}(s_N[o_i], \mathcal{A}_G[o_i])$;
- 10 **end**
- 11 **return** c

in $h(s_N)$. In the EE scenario, if $\{p_s, p_n, p_g\}$ forms a triangle in x-y space, the distance sum is minimized when p_b is the Fermat point of $\Delta p_s p_n p_g$. If $\{p_s, p_n, p_g\}$ forms a line instead, the optimal p_b is at the pose in the middle. In the MB scenario, we minimize the total base travel. Denote the base positions of $\{p_s, p_n, p_g, p_b\}$ as $\{b_s, b_n, b_g, b_b\}$. When b_b is not at the three points or their opposite points, there are two points of $\{b_s, b_n, b_g\}$ on one half of the track and another on the other half of the track. In the example of Figure 5.2[Left], if b_b is at the current position, then b_s and b_n are on the left part of the track, and b_g is on the other side. Moving toward the two-point direction by d , b_b can always reduce the total traveling cost by d . Therefore, the extreme points of total distance are $\{b_s, b_n, b_g\}$ and their opposites on the track, and $\{b_s, b_n, b_g\}$ are the minima. As a result, in MB scenario, the optimal p_b minimizing the total distance to $\{p_s, p_n, p_g\}$ can be chosen among them.

5.4.3 Buffer Allocation

We now discuss ORLA*'s buffer allocation process. Buffer poses are allocated when a new DS is reached, and some object moves to a buffer pose since the last DS node.

Algorithm 14: Distance Refinement

Input : s_N : an NDS state; o_i : object at buffer; \mathcal{A}_G : goal arrangement
Output: c : additional cost

- 1 $p_s \leftarrow$ the pose of o_i before moved to buffer.
- 2 $p_n \leftarrow$ the pose that the robot visit after placing o_i to buffer.
- 3 $p_g \leftarrow \mathcal{A}_G[o_i]$.
- 4 **if** *EE scenario* **then** $p_b \leftarrow$ Fermat point of $\Delta p_s p_n p_g$;
- 5 **else if** *MB scenario* **then**
- 6 | $p_b \leftarrow$ The one in $\{p_s, p_n, p_g\}$ with the shortest total distance to the other two.
- 7 **end**
- 8 **return** $\sum_{p \in \{p_s, p_n, p_g\}} (dist(p_b, p)) - dist(p_s, p_n)$

5.4.3.1 Feasibility of a Buffer Pose

A buffer pose p_b of o_i is feasible if o_i can be stably placed at p_b without collapsing and o_i should not block other object actions during o_i 's stay. To predict the stability of placement of a general-shaped object, we propose a learning model StabilNet based on Resnest[119]. StabilNet consumes two $200 * 200$ depth images of the surrounding workplace from the top and the placed object from the bottom, respectively. It outputs the possibility of a successful placement. The data and labels are generated by PyBullet simulation. The depth images are synthesized in the planning process based on object poses and the stored point clouds to save time. In addition to buffer pose stability, we must avoid blocking actions during the object's stay at the buffer pose. For an action moving an object o_j from p_j^1 to p_j^2 . o_i at the buffer pose needs to avoid o_j at both p_j^1 and p_j^2 . We add these constraints when we allocate buffer poses.

5.4.3.2 Optimality of a Buffer Pose

Given the task plan, a set of buffer poses is optimal if the traveling cost is minimized. For each object needing a buffer pose, we compute P_b^* , the set of buffer poses minimizing the traveling cost. In the traveling cost, the trajectories from the buffer pose p_b to four deterministic poses are involved: the last deterministic pose the robot visits before placing and picking at p_b , and the first pose the robot visits after placing and picking at p_b .

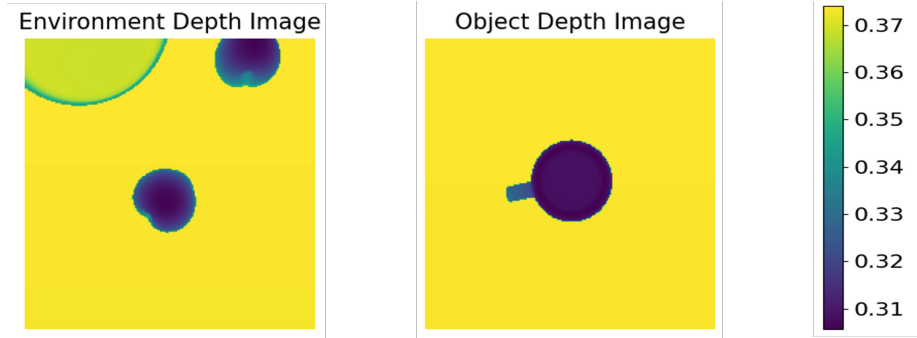


Figure 5.3: An example input of StabilNet when attempting to place a cup right on top of an apple in the environment. The ground truth label given by the simulation is a failure.

In the EE scenario, if the four points form a quadrilateral, the total distance is minimized when p_b is placed at the intersection of the diagonal lines. Otherwise, if two or more points overlap, the optimal p_b is the point among four points minimizing the traveling cost. Therefore, P_b^* in EE scenario is a set of poses with above-computed x, y .

In the MB scenario, let b_b be the mobile base position when visiting p_b . And denote the mobile base positions of the four involved poses as $P = \{b_1, b_2, b_3, b_4\}$. The four points and their opposites $\hat{P} = \{\hat{b}_1, \hat{b}_2, \hat{b}_3, \hat{b}_4\}$ partition the track into up to eight segments. Similar to the case in Algorithm 14, $\hat{P} \cup P$ are extreme points of the distance sum. And the points with the minimum value are optimal b_b solutions. Moreover, for any of the eight segments, if both of its endpoints are with the minimum value, the whole segments are optimal b_b solutions. Therefore, in MB scenario, P_b^* is a set of poses whose corresponding mobile base positions are at the points or segments computed above.

5.4.3.3 Buffer Sampling

Algorithm 15 handles buffer sampling. When multiple objects need buffers since the last DS, we sample buffers for them one after another (Line 1-3). The sampling order is sorted by the time the object is placed in the buffer. In Lines 4-5, we collect information for pose feasibility checks. E is used to predict the stability of a buffer pose. A contains object footprints that o_i must avoid during the buffer stay. We first sample buffer poses in P_b^* (Line 8-12), and gradually expand the sampling region when we fail to find a feasible

buffer (Line 14). If we cannot find a feasible buffer when the sampling region covers the tabletop area, we return the latest P . In the case of a failure, we remove S_D from A* search tree and create another new DS node S''_D at the failing step. S''_D represents the state before the failing o_i is moved to buffer. At S''_D , all objects at buffers have found feasible buffer poses in the returned P . Therefore, all objects in S''_D are at deterministic poses. Note that in our implementation, P_b^* in MB scenario is represented by a segment of the mobile base track. As a result, for Line 9 in MB scenario, we first sample a mobile base position on the track and then sample a pose based on that.

Algorithm 15: Buffer Sampling

Input : s_D : an DS state,
Output: P : buffer poses

- 1 $B \leftarrow$ Objects go to buffers since the last DS.
- 2 $P \leftarrow \{o_i : \emptyset \forall o_i \in B\}$
- 3 **for** $o_i \in B$ **do**
- 4 $E \leftarrow$ The environment when the buffer is placed.
- 5 $A \leftarrow$ A list of poses to avoid based on the task plan.
- 6 $P_b^* \leftarrow$ The placing region minimizing traveling cost.
- 7 **while** o_i 's Buffer Not Found **do**
- 8 **for** $i \leftarrow 0$ **to** $k - 1$ **do**
- 9 $p_b \leftarrow$ Sample a pose in P_b^* .
- 10 **if** $poseFeasible(p_b, o_i, E, A)$ **then**
- 11 Add p_b to P ;
- 12 **go to** Line 3;
- 13 **end**
- 14 **end**
- 15 **if** P_b^* is the whole tabletop region **then return** P ;
- 16 **else** $P_b^* \leftarrow$ expand(P_b^*);
- 17 **end**
- 18 **end**
- 19 **return** P

5.4.4 Optimality of ORLA*

Our ORLA* consists of two main components: high-level A* search and low-level buffer allocation process. In terms of the high-level lazy A*, the $h(s)$ of DS is consistent, and $g(s)$ of DS does not rely on $g(s)$ of NDSs. Therefore, by only considering DSs, lazy A* is a

standard A* with global optimality. Additionally, $f(s)$ values for NDSs underestimate the actual cost. Therefore, high-level lazy A* is globally optimal in its domain. Note that the formulated buffer allocation problem is an established *Constraints Optimization Problem*, which can be solved optimally if we assume StabilNet makes correct stability predictions. By replacing the buffer sampling with an optimal solver, ORLA* is globally optimal.

5.5 Evaluation

We present simulation evaluations on ORLA* and compare them with state-of-the-art rearrangement planners implemented in Python. For each experiment, costs and computation time are averages of test cases finished by all methods. Experiments are executed on an Intel® Xeon® CPU at 3.00GHz. To measure instance difficulty, we define the density level of workspace ρ as $\frac{\sum_{o \in \mathcal{O}} S(o)}{S_T}$, where $S(o)$ is the footprint size of the object o and S_T is the size of the tabletop region. We set $C = 10$ in cost function $\mathcal{J}(\Pi)$.

We first compare ORLA*-Full, ORLA*-Action, Greedy-Sampling, MCTS[81], and TRLB from Chapter 3 in disc instances (Figure 5.4) without StabilNet. ORLA*-Full is our ORLA* minimizing $\mathcal{J}(\Pi)$. ORLA*-Action only considers manipulation costs, i.e. minimizes the number of pick-n-places. Greedy-Sampling maintains an A* search tree with $\mathcal{J}(\Pi)$. Instead of lazy buffer allocation, it samples buffer poses immediately as close to goal poses as possible when objects are moved to buffers. MCTS and TRLB compute rearrangement plans using Monte-Carlo tree search with random buffer sampling and bi-directional tree search with lazy buffer allocation respectively. These two planners only consider buffer poses in the free space. In disc instances, we assume all poses are stable to be placed on but the robot cannot manipulate an object if another object is on top. The table sizes of EE and MB instances are $1m \times 1m$ and $3m \times 1m$, respectively. In disc instances with different numbers of objects, we adjust the disc radius to keep ρ constant. We also test ORLA*-Full and ORLA*-Action in general-shaped object instances (Figure 5.5) with StabilNet for buffer pose sampling.

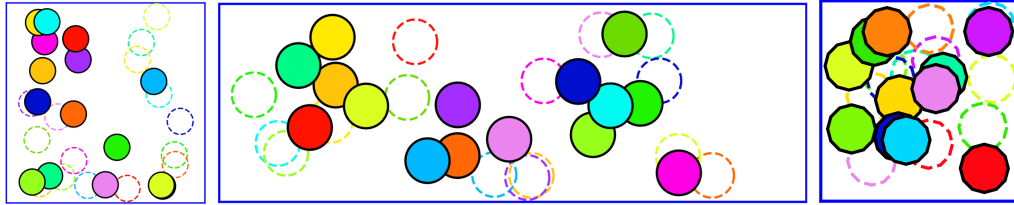


Figure 5.4: Examples of disc instances. [Left] EE scenario with $\rho = 0.2$; [Middle] MB scenario with $\rho = 0.2$; [Right] EE scenario with $\rho = 0.5$. Colored and transparent discs represent the initial and goal arrangements respectively.

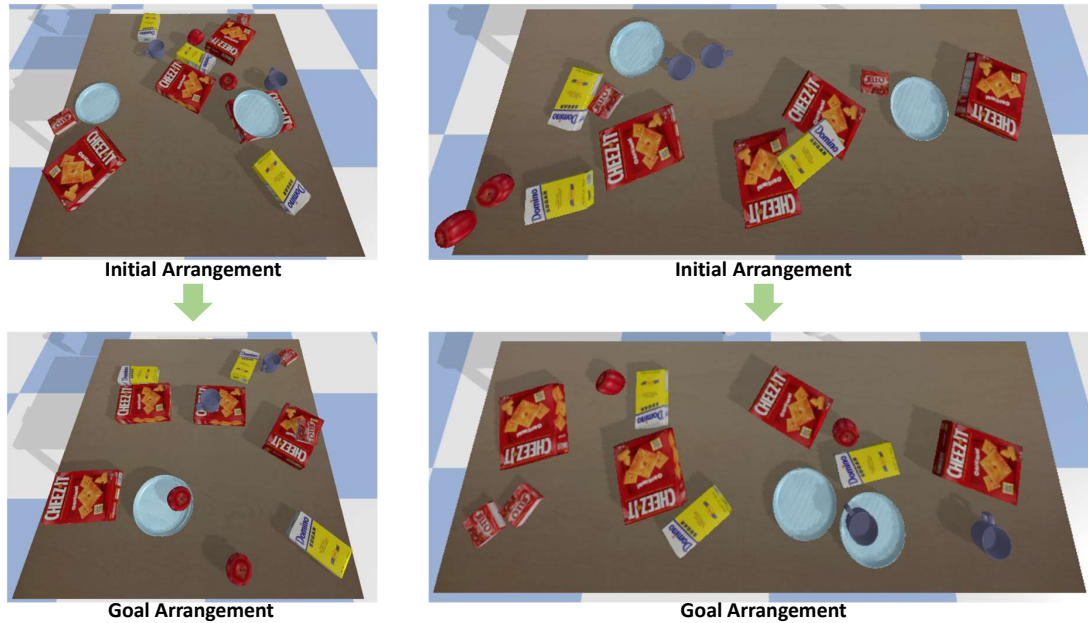


Figure 5.5: Examples of instances with general-shaped objects in [Left] EE and [Right] MB scenarios.

5.5.1 Disc Rearrangement in Simulation

Figure 5.6 shows algorithm performance in EE scenario with $\rho = 0.2$. Comparing ORLA*-Full and ORLA*-Action, ORLA*-Full saves around 15% path length without an increase in the manipulation cost. Without the lazy buffer strategy, Greedy-Sampling spends more time on planning but yields much worse plans in general, e.g., additional 23% actions in 5-discs instances. That is because ORLA*-Full allocates buffer poses avoiding future actions while immediately sampled buffer poses in Greedy-Sampling may block some of these actions. Due to the repeated buffer sampling, Greedy-Sampling can only solve 40% instances in 7-object instances. However, Greedy-Sampling has reasonably good performance in

the total path length despite the large number of actions, so allocating buffers near the goal pose is a good strategy for saving traveling costs. We also note that the number of actions as multiples of $|\mathcal{O}|$ reduces as $|\mathcal{O}|$ increases, which indicates a reducing difficulty in rearrangement. That is because given a fixed density level, as $|\mathcal{O}|$ increases, the relative size of each object to the workspace is smaller, which makes it easier to find valid buffer poses.

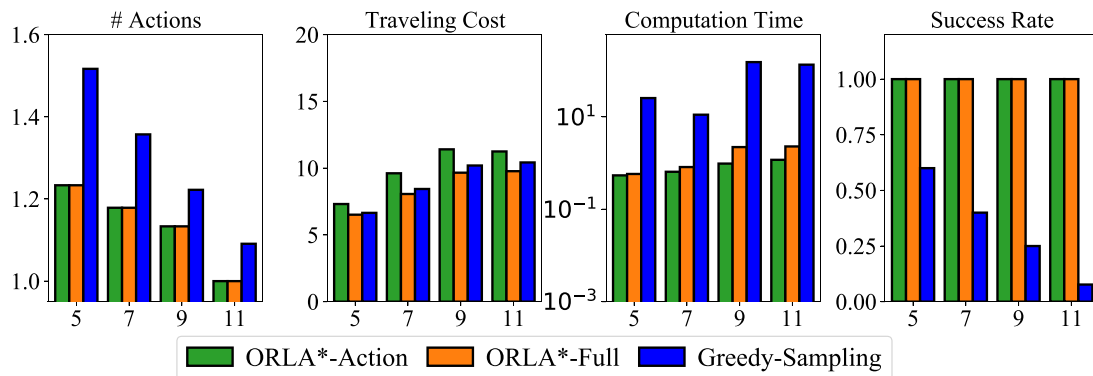


Figure 5.6: Algorithm performance in EE disc instances with $\rho = 0.2$ and 5-11 objects. (a) # pick-n-places in solutions as multiples of $|\mathcal{O}|$. (b) Traveling cost (m). (c) Computation time (secs). (d) Success rate.

We also compare ORLA* variants with TRLB and MCTS in dense disc instances ($\rho = 0.5$) of EE scenario. An example of the dense instance is shown in Figure 5.4[Right]. While MCTS fails in all test cases, the results of other methods are shown in Figure 5.7. Comparing ORLA*-Action and TRLB, the results suggest that considering buffer poses on top of other objects not only effectively increases the success rate, but also provides shorter paths with lower traveling cost and manipulation cost in dense test cases. Comparing ORLA* variants, ORLA*-Full saves 4.2% – 11.7% traveling cost, but ORLA*-Action has a much higher success rate in 5-object instances, which is the hardest for buffer sampling as mentioned previously.

Figure 5.8 shows algorithm performance in MB scenario with $\rho = 0.2$. In this scenario, taking mobile base traveling costs into consideration significantly reduces traveling costs in solutions. ORLA*-Full saves over 20% traveling costs on average in 11-disc instances but spends more time in computation.

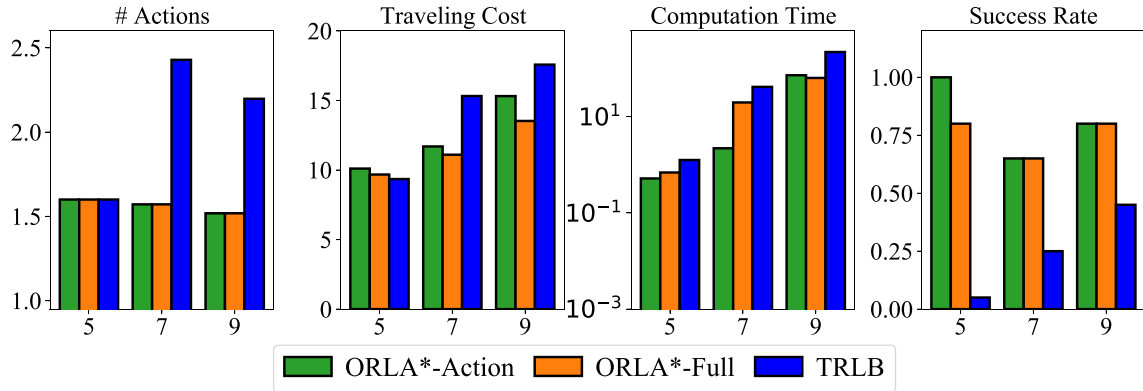


Figure 5.7: Algorithm performance in EE disc instances with $\rho = 0.5$ and 5-11 objects. (a) # pick-n-places in solutions as multiplies of $|\mathcal{O}|$. (b) Traveling cost (m). (c) Computation time (secs). (d) Success rate.

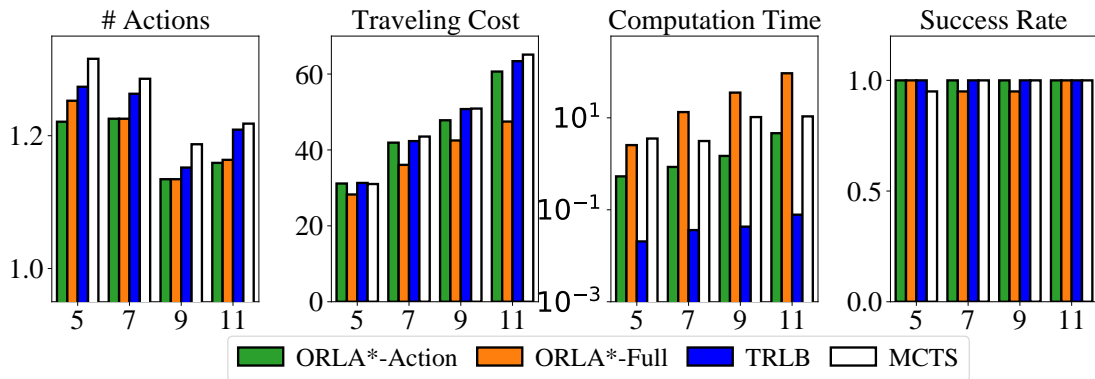


Figure 5.8: Algorithm performance in MB disc instances with $\rho = 0.2$ and 5-11 objects. (a) # pick-n-places in solutions as multiplies of $|\mathcal{O}|$. (b) Traveling cost (m). (c) Computation time (secs). (d) Success rate.

To summarize, in disc rearrangement experiments, we have the following conclusions: First, intelligent temporary object placement on top of other objects with ORLA* computes low-cost plans in dense test cases. Second, considering traveling costs in the ORLA* framework effectively reduces traveling costs without an increase in manipulation costs but induces additional computation time. Finally, the results suggest that lazy buffer allocation improves solution quality and saves computation time.

5.5.2 Qualitative Analysis of StabilNet

Regarding the placement stability prediction model StabilNet, we train it with four types of objects in Pybullet simulator: an apple, a pear, a plate, and a cup. Figure 5.9(a) shows the prediction distribution of a scene with the plate and the apple when placing the cup. We sample 8 poses of the placed object with different orientations for each point in the distribution map. The distribution shows the average of the 8 output probabilities. When the cup pose is sampled far from both objects (the top-right corner and the bottom-left corner) or on the plate, StabilNet supports placements with outputs around 0.999 and 0.90, respectively. When the cup pose is sampled at the rim of the plate and on top of the apple, StabilNet also rejects placements with outputs around 0.02 and 0.005. Due to the existence of the handle, StabilNet is conservative when the cup is placed close to the plate rim.

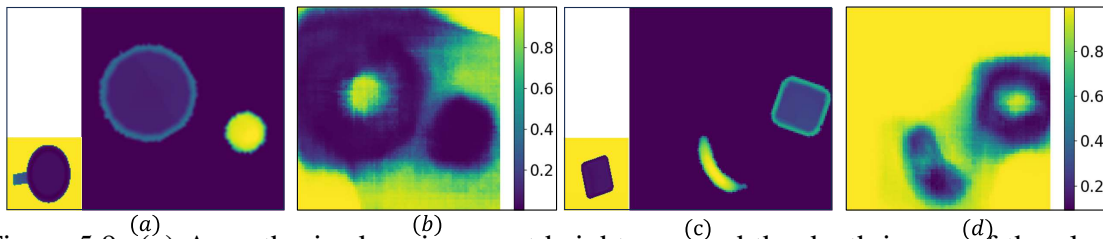


Figure 5.9: **(a)** A synthesized environment height map and the depth image of the placed object from the bottom. All objects are from the training set. **(b)** The corresponding stabil-ity prediction distribution of (a). **(c)** A synthesized environment height map and the depth image of the placed object from the bottom. All objects are outside the training set. **(d)** The corresponding stability prediction distribution of (c).

To show the model’s generalization ability, we present the prediction distribution of a scene with untrained objects in Figure 5.9(c). In this environment, we place a square plate and a banana. The plate’s size and shape differ from those in the training set. And not to say the banana. The placed object is a small tea box while we do not have any cuboid object in the training set. As shown in Figure 5.9(b), StabilNet clearly judges the stability when placing the novel box into the workspace.

5.5.3 General-Shaped Object Rearrangement in Simulation

In general-shaped instances, we equip ORLA* methods with StabilNet. Given a set of objects in the workspace, we compute the total area of object footprints and adjust the size of the tabletop region to keep $\rho = 0.25$. Figure 5.10 presents algorithm performance in EE and MB scenarios, respectively. In this scenario, we use StabilNet to decide whether an object is safe to be temporarily placed on top of another. Due to the inference time for StabilNet in buffer sampling, the computation time of ORLA* methods is longer than that in disc experiments. In 11-object instances, ORLA*-Full saves 16.7% and 13% traveling cost than ORLA*-Action in EE and MB scenarios respectively. However, ORLA*-Action maintains 100% success rate while ORLA*-Full fails in 13.5% MB test cases.

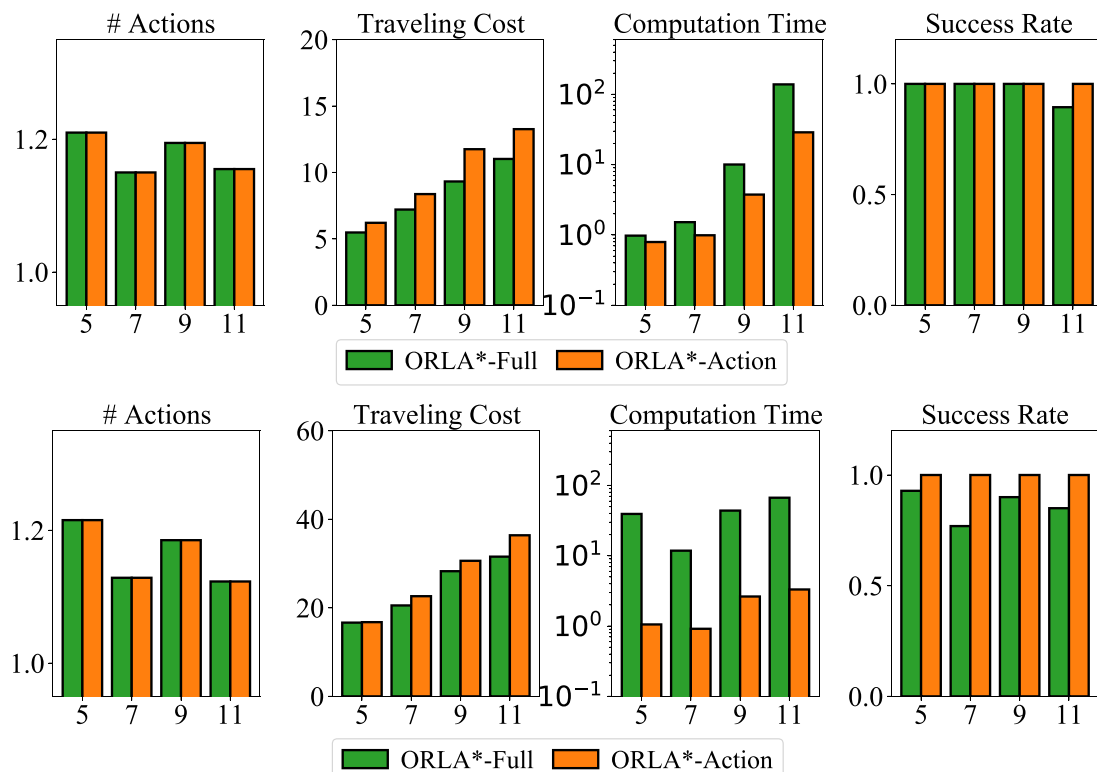


Figure 5.10: Algorithm performance in [Top] EE scenario and [Bottom] MB scenario with general-shaped objects. $\rho = 0.25$ and 5-11 objects. (a) # pick-n-places in solutions as multiples of $|\mathcal{O}|$. (b) Traveling cost (m). (c) Computation time (secs). (d) Success rate.

5.6 Summary

In this chapter, we discuss the cooperative dual-arm rearrangement (CDR) problem in a partially shared workspace.

For task planning, we employ a lazy strategy for buffer allocation in the dual-arm rearrangement system. To coordinate manipulations of the arms, we develop dependency graph guided heuristic search algorithms computing optimal primitive task schedules under two makespan evaluation metrics. The effectiveness of the proposed procedure is demonstrated with extensive simulation studies in the PyBullet environment with two UR-5e robot arms. Specifically, plans computed by our algorithms are up to 35% shorter than greedy ones in execution time in dense rearrangement instances. Moreover, we observe a tradeoff between the number of needed handoffs and the occurrence of path conflicts in CDR problems as the overlap ratio of the workspace varies.

For motion planning, MODAP outputs the planned trajectory while conforming to specified robot dynamics constraints, e.g., velocity, acceleration, and jerk limits. Compared to the previous state of the art, MODAP achieves up to 40% execution time improvement even though the planned trajectories are longer. In particular, MODAP shines in cases where extensive joint dual-arm planning must be carried out to compact the overall task and motion plan.

CHAPTER 6

CONCLUSIONS

This thesis summarizes my efforts in the problem of TORO with external and internal buffers.

For TORO with External buffers (TORE), we study the maximum running buffer size (MRB), which is an important quantity to understand as it determines the problem’s feasibility. Despite the provably high computational complexity that is involved, we provide effective dynamic programming-based algorithms capable of quickly computing MRB for large and dense labeled/unlabeled TORO instances.

Fast optimal algorithms for TORE led to our development of TRLB in the internal buffer setup. The TRLB framework employs the dependency graph representation and a lazy buffer allocation approach for efficiently solving the problem of rearranging many tightly packed objects on a tabletop. Extensive simulation studies show that TRLB computes rearrangement plans of comparable or better quality as the state-of-the-art methods, and does so up to 2 magnitudes faster.

We extend the idea of lazy buffer verification to handle object heterogeneity (HeTORI), dual-arm coordination (CDR), and time-optimal mobile manipulation (MoTaR). Specifically, in HeTORI, we consider object property difference in TRLB with weighting heuristics; in CDR and MoTaR, we integrate TRLB into A* framework for TORI under different objective functions.

Appendices

APPENDIX A
STRUCTURAL PROPERTIES AND PROOFS FOR TORO

Properties of Unlabeled Dependency Graphs for Special TORO Settings

Proof of Proposition 2.3.2. The maximum degree of the dependency graph is equal to the maximum number of disjoint objects that one object can overlap with. In this proof, we evaluate the upper bound of the maximum overlaps with a disc packing problem. We first discuss the range of distance between two overlapping regular polygons when they are overlapping and disjoint. After that, we relate the problem to a disc packing problem and derive the upper bound. Without loss of generality, we assume the radius of the regular polygons to be 1. When two d -sided regular polygons overlap, the distance between the polygon centers is upper bounded by two times the radius of their circumscribed circles, i.e. 2. When two d -sided regular polygons are disjoint, the distance between the polygon centers is lower bounded by two times the radius of their inscribed circles, i.e. $2 \cos(\frac{\pi}{d})$. Due to the mentioned upper bound, the number of disjoint d -sided regular polygons that overlap with one d -sided regular polygon is upper bounded by that whose centers are inside a 2-circle (Figure A.1(a)). Additionally, due to the mentioned distance lower bound, this number is upper bounded by the number of disjoint $\cos(\frac{\pi}{d})$ -circles whose centers are inside a 2-circle (Figure A.1(b)), which is equal to the number of $\cos(\frac{\pi}{d})$ -circles packed inside a $(2 + \cos(\frac{\pi}{d}))$ -circle (Figure A.1(c)). Since the radius ratio of circles $\frac{2 + \cos(\frac{\pi}{d})}{\cos(\frac{\pi}{d})}$ is upper bounded by 5 when $d \geq 3$, there are at most 19 small circles packed in the large circle [120]. Therefore, the maximum degree of the unlabeled dependency graph is upper bounded by 19.

□

Proof of Proposition 2.3.3. Constructing the dependency graph based on the start and goal positions in the workspace, the planarity can be proven if no two edges cross each other. Assuming the contrary, there are two edges crossing each other, e.g. AD and BC in Figure A.2[Left]. Since each edge comes from a pair of intersecting start and goal objects, without loss of generality, we can assume C, D are start positions and A, B are goal positions. Therefore, we have $|AB|, |CD| \geq 2r$, where r is the base radius of the cylinders. Since AD and BC are both connected in the dependency graph, we have $|AD|, |BC| < 2r$, which leads to the conclusion that $|AD| + |BC| < 4r \leq |AB| + |CD|$, and contradicts the triangle inequality. Therefore, the planarity is proven with contradiction.

Since uniform cylinders have uniform disc bases, one cylinder may only touch six non-overlapping cylinders and non-trivially intersect at most five non-overlapping cylinders. Therefore, the maximum degree of the unlabeled dependency graph is upper bounded by 5.

□

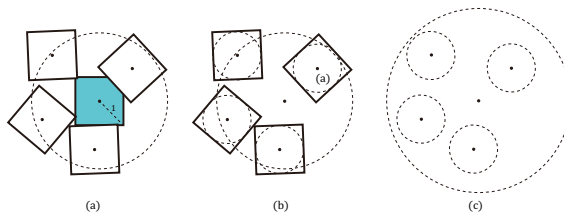


Figure A.1: (a) The number of disjoint d -sided regular polygons that overlap with one d -sided regular polygon is upper bounded by that whose centers are inside a 2-circle. (b) The number of disjoint d -sided regular polygons whose centers are inside a 2-circle is upper bounded by the number of disjoint $\cos(\frac{\pi}{d})$ -circles whose centers are inside a 2-circle. (c) The number of disjoint $\cos(\frac{\pi}{d})$ -circles whose centers are inside a 2-circle is equal to the number of $\cos(\frac{\pi}{d})$ -circles packed inside a $(2 + \cos(\frac{\pi}{d}))$ -circle.

Remark. As shown in Figure A.2[Right], the proof of the planarity in Proposition 2.3.3 does not hold for objects with regular polygon bases.

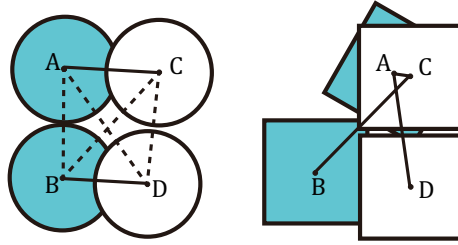


Figure A.2: [Left] A case discussed in Prop. Proposition 2.3.3 [Right] A counterexample of the proof of Prop. Proposition 2.3.3 when the base of workspace objects is square.

$\Omega(\sqrt{n})$ Lower Bound for URBM

Let (x, y) be the coordinate of a vertex $v_{x,y}$ on $\mathcal{D}(w, h)$ with the top left being $(1, 1)$. The parity of $x + y$ determines the partite set of the vertex (recall that unlabeled dependency graph for uniform cylinders is always a planar bipartite graph, by Proposition 2.3.3), which may correspond to a start pose or a goal pose. With this in mind, we simply call vertices of $\mathcal{D}(w, h)$ start and goal vertices; without loss of generality, let $v_{1,1}$ be a start vertex.

We use $\mathcal{D}(m, 2m)$ for establishing the lower bound on MRB. We use a *vertex pair* $p_{i,j}$ to refer to two adjacent vertices $v_{i,2j-1}$ and $v_{i,2j}$ in $\mathcal{D}(m, 2m)$. It is clear that a vertex pair contains a start and a goal vertex. We say that a goal vertex is *filled* if an object is placed at the corresponding goal pose. We say that a start vertex (which belongs to a vertex pair) is *cleared* if the corresponding object at the vertex is picked (either put at a goal or at a buffer) but the corresponding goal in the vertex pair is unfilled. At any moment when the robot is not holding an object, the number of objects in the buffer is the same as the number of cleared vertices. For each column i , $1 \leq i \leq m$, let f_i (resp., c_i) be the number of goals (resp., start) vertices in the column that are filled (resp., cleared). Notice that a goal cannot be filled until the object at the corresponding start vertex is removed.

Lemma A.0.1. *On a dependency grid $\mathcal{D}(m, 2m)$, for two adjacent columns i and $i + 1$, $1 \leq i < m$, if $f_i + f_{i+1} \neq 0$ or $2m$, then $c_i + c_{i+1} \geq 1$. In other words, there is at least one cleared vertex in the two adjacent columns unless $f_i = f_{i+1} = 0$ or $f_i = f_{i+1} = m$.*

Proof. If there is a j , $1 \leq j \leq m$, such that only one of the goal vertices in vertex pairs

$p_{i,j}$ and $p_{i+1,j}$ is filled (Figure A.3(a)), then the start vertex in the other vertex pair must be cleared. Therefore, $c_i + c_{i+1} \geq 1$.

On the other hand, if, for each $j, 1 \leq j \leq m$, both or neither of the goal vertices in $p_{i,j}$ and $p_{i+1,j}$ is filled, then there is a $j, 1 \leq j \leq m - 1$, such that both goal vertices in $p_{i,j}$ and $p_{i+1,j}$ are filled but neither of those in $p_{i,j+1}$ and $p_{i+1,j+1}$ is filled (Figure A.3(b)) or the opposite (Figure A.3(c)). Then, for the vertex pairs whose goal vertices are not filled, say $p_{i,j+1}$ and $p_{i+1,j+1}$, one of their start vertices is a neighbor of the filled goal in $p_{i,j}$ and $p_{i,j+1}$. Therefore, at least one of the start vertices in $p_{i,j+1}$ and $p_{i+1,j+1}$ is a cleared vertex. And thus, $c_i + c_{i+1} \geq 1$.

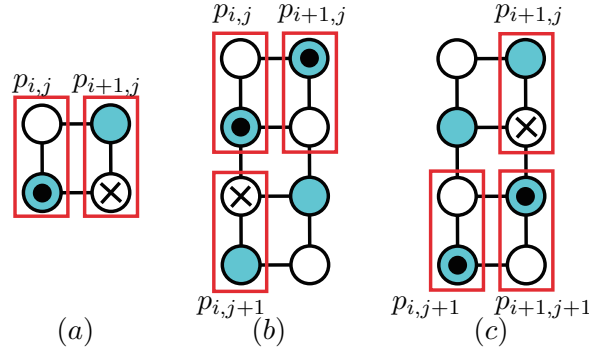


Figure A.3: Some cases discussed in the Lemma A.0.1. The unshaded and shaded nodes represent the start and goal vertices in the dependency graph. Specifically, the shaded nodes with a dot inside represent the filled vertices and the unshaded nodes with a cross inside represent the cleared vertices. (a) When only one goal vertex in $p_{i,j}$ and $p_{i+1,j}$ is filled up, the start vertex in the other vertex pair is a cleared vertex. (b) When both goal vertices in $p_{i,j}$ and $p_{i+1,j}$ are filled but neither of those in $p_{i,j+1}$ and $p_{i+1,j+1}$ is filled, one of the start vertices $p_{i,j+1}$ and $p_{i+1,j+1}$ is a cleared vertex. (c) The opposite case of (b).

□

Proof of Lemma 2.5.1. We show that there are $\Omega(m)$ cleared vertices when $\lfloor n/3 \rfloor$ goal vertices are filled. Suppose there are q columns in \mathcal{D} with $1 \leq f_i \leq m - 1$. According to the definition of f_i , for each of these q columns, there is at least one goal vertex that is filled and at least one goal vertex that is not.

If $q < \frac{\lfloor n/3 \rfloor}{3(m-1)}$, then there are two columns i and j , such that $f_i = m$ and $f_j = 0$. That is because $\sum_{1 \leq i \leq m} f_i = \lfloor n/3 \rfloor$ and $0 \leq f_i \leq m$ for all $1 \leq i \leq m$. Therefore, for the

vertex pairs in each row j , at least one goal vertex is filled but at least one is not. And thus, for each j , there are two adjacent columns $i, i + 1, 1 \leq i < m$, such that in vertex pairs $p_{i,j}$ and $p_{i+1,j}$, one goal vertex is filled while the start vertex in the other vertex pair is cleared (Figure A.3(a)). Therefore, there are at least m cleared vertices in this case.

If $q \geq \frac{\lfloor n/3 \rfloor}{3(m-1)}$, then we partition all the columns in \mathcal{D} into $\lfloor m/2 \rfloor$ disjoint pairs: (1,2), (3,4), ... The q columns belong to at least $\lfloor q/2 \rfloor$ pairs of adjacent columns. Therefore, according to Lemma Lemma A.0.1, we have $\Theta(m)$ cleared vertices.

In conclusion, there are $\Omega(m)$ cleared vertices when there are $\lfloor n/3 \rfloor$ filled goal. Therefore, the minimum MRB of this instance is $\Omega(m)$.

□

$O(\sqrt{n})$ Algorithmic Upper Bound for URBM

To investigate the running buffer size of the plan computed by SEPPLAN, we construct a binary tree T based on SEPPLAN (Figure 2.11(c)). Each node represents a recursive call consuming a subgraph $G_{\mathcal{A}_s, \mathcal{A}_g}^u(V, E)$ and the left and right children of the node are induced from subgraphs $G_{\mathcal{A}_s, \mathcal{A}_g}^u(A', E(A'))$ and $G_{\mathcal{A}_s, \mathcal{A}_g}^u(B', E(B'))$ of $G_{\mathcal{A}_s, \mathcal{A}_g}^u(V, E)$. SEPPLAN computes the plan by visiting the binary tree in a depth-first manner. For each node on T , given the input dependency graph $G_{\mathcal{A}_s, \mathcal{A}_g}^u(V, E)$, denote the sequence before we deal with $G_{\mathcal{A}_s, \mathcal{A}_g}^u(V, E)$ as π_0 . Denote the vertices pruned in $\text{RemovalTrivialGoals}(G_{\mathcal{A}_s, \mathcal{A}_g}^u(V, E))$ as P . Without loss of generality, assume that SEPPLAN recurses into A' before B' . Let π_P , $\pi_{C'}$, $\pi_{A'}$, and $\pi_{B'}$ be the goal removal sequence after we remove vertices in P , C' , A' and B' from $G_{\mathcal{A}_s, \mathcal{A}_g}^u(V, E)$ respectively. We define function $RB(\pi)$ to represent “generalized” current running buffer size of a removal sequence π : When vertices in π are removed from the dependency graph, $RB(\pi)$ equals either the number of running buffers; or the negation of the number of empty goal poses. In the depth-first recursion, each node on the binary tree T is visited at most three times:

1. Before exploring child nodes. The peak may be reached during the removal of C' .

Let π_{C^*} be the sequence when the running buffer size reaches the peak. $RB(\pi_{C^*}) \leq RB(\pi_0) + 10\sqrt{2}\sqrt{|V|}$.

2. After we deal with A' and before we deal with B' . $RB(\pi_{A'}) = RB(\pi_0) - \delta(C') - \delta(A')$.
3. After we deal with B' . $RB(\pi_{B'}) = RB(\pi_0) - \delta(V)$.

Lemma A.0.2. $RB(\pi_{A'}) \leq (RB(\pi_{C^*}) + RB(\pi_{B'}))/2$.

Proof.

$$\begin{aligned}
& RB(\pi_{A'}) \\
&= RB(\pi_0) - \delta P - \delta C' - \delta A' \\
&= RB(\pi_0) - \delta(P) - \delta(C') - \max[\delta(A'), \delta(B')] \\
&\leq RB(\pi_0) - \delta(P) - \delta(C') + \frac{1}{2}[-\delta(V) + \delta(P) + \delta(C')] \\
&= \frac{1}{2}\{[RB(\pi_0) - \delta(V)] + [RB(\pi_0) - \delta(P) - \delta(C')]\} \\
&= \frac{1}{2}[RB(\pi_{B'}) + RB(\pi_{C'})] \\
&\leq \frac{1}{2}[RB(\pi_{B'}) + RB(\pi_{C^*})]
\end{aligned}$$

□

Lemma A.0.2 establishes the relationship among π_{C^*} , $\pi_{A'}$, and $\pi_{B'}$ of a node on T . With this lemma, we obtain an upper bound for each node:

Lemma A.0.3. *Given a node N with depth d in the binary tree T , let $\pi_{C^*}(N)$, $\pi_{A'}(N)$, and $\pi_{B'}(N)$ be π_{C^*} , $\pi_{A'}$, and $\pi_{B'}$ of N respectively. $RB(\pi_{C^*}(N))$, $RB(\pi_{A'}(N))$, and $RB(\pi_{B'}(N))$ are all upper bounded by*

$$\frac{[1 - (\sqrt{\frac{2}{3}})^{d+1}]}{1 - \sqrt{\frac{2}{3}}} 20\sqrt{n} \tag{A.1}$$

where n is the number of objects in the instance.

Proof. The conclusion can be proven by induction.

When $d = 0$, the dependency graph at the root node r has n start vertices and n goal vertices. We have $RB(\pi_{C^*}) \leq 20\sqrt{n}$, $RB(\pi_{B'}) = 0$. According to Lemma Lemma A.0.2, $RB(\pi_{A'}) \leq 10\sqrt{n}$. The conclusion holds.

Assume that the conclusion holds for all the nodes with depth less than or equal to k . Given an arbitrary node N in the depth k , let the left and right children of N be L and R , which are the nodes with depth $k + 1$. The corresponding dependency graphs have at most $(2/3)^{k+1} \cdot 2n$ vertices respectively.

$$RB(\pi_{C^*}(L)) \leq RB(\pi_{C^*}(N)) + \sqrt{(2/3)^{k+1} \cdot 2n} \cdot 10\sqrt{2}$$

$$RB(\pi_{C^*}(R)) \leq RB(\pi_{A'}(N)) + \sqrt{(2/3)^{k+1} \cdot 2n} \cdot 10\sqrt{2}$$

Since $\pi_{B'}(L) = \pi_{A'}(N)$ and $\pi_{B'}(R) = \pi_{B'}(N)$, upper bound for nodes with depth k holds for $\pi_{B'}(L)$ and $\pi_{B'}(R)$. Therefore, the running buffer size for the depth $k + 1$ nodes has an upper bound

$$\begin{aligned} & \frac{[1 - (\sqrt{2/3})^{k+1}]}{1 - \sqrt{2/3}} 20\sqrt{n} + \sqrt{(2/3)^{k+1} \cdot 2n} \cdot 10\sqrt{2} \\ &= \frac{[1 - (\sqrt{2/3})^{k+2}]}{1 - \sqrt{2/3}} 20\sqrt{n} \end{aligned} \tag{A.2}$$

Therefore, the upper bound holds for all the nodes of depth $k + 1$. With induction, the lemma holds. □

With Lemma A.0.3, it is straightforward to establish that MRB is bounded by $\frac{20}{1 - \sqrt{2/3}} \sqrt{n}$, yielding Theorem 2.5.2.

APPENDIX B

INTERVAL STATE SPACE HEURISTIC SEARCH FOR CDR IN FC MAKESPAN (FCHS)

FC metric estimates the total execution time of rearrangement. For each pick-n-place action, the execution time is counted from the moment when the robot leaves for the object to the moment when the robot finishes the placement of the object. Therefore, the cost of a pick-n-place can be expressed by $t_{pp}(p_c, p_g, p_r)$, where p_c is the current end-effector pose. p_g, p_r are the pick and place poses of the object. Similarly, for each handoff operation, the execution time of the delivery (resp. receiving) arm is counted from the moment when the robot leaves for the pick pose (resp. handoff pose), to the moment when the handoff (resp. the placement) is finished. With the same notations of locations, the cost of the delivery arm and the receiving arm in a handoff operation can be expressed as $t_{hd}(p_c, p_g)$ and $t_{hr}(p_c, p_r)$ respectively. Besides object manipulations, robot arms move back to the rest pose when the rearrangement task is complete.

When the FC metric is considered, objects at intermediate states cannot be guaranteed to be at stable poses inside the workspace. Based on the observation, we introduce a state space based on time intervals. Each state can be expressed by two mappings $\mathcal{L} : \mathcal{O} \rightarrow \{S, G, \mathcal{B}(r_1), \mathcal{B}(r_2), T\}$ and $\mathcal{T} : \mathcal{R} \rightarrow (O \times \{G, \mathcal{B}(r_1), \mathcal{B}(r_2)\}) \cup \{E\}$. \mathcal{L} indicates the current object status. $S, G, \mathcal{B}(r_1), \mathcal{B}(r_2), T$ are five kinds of possible status of objects in the state: staying at start pose, goal pose, buffer in $\mathcal{S}(r_1)$, buffer in $\mathcal{S}(r_2)$, or being involved in the current task of a robot arm. Specifically, $\mathcal{L}(o_i) = T$ when either o_i is being manipulated by a robot, or a robot is on the way to pick it. \mathcal{T} indicates the current executing task of robot arms. When $\mathcal{T}(r_i) = (o_j, G)$ (resp. $(o_j, \mathcal{B}(r_i))$), r_i is executing a task moving o_j from the current pose to its goal pose (resp. buffers). When $\mathcal{T}(r_i) = E$, r_i idles or just finishes an execution. Each state except the start/goal state mimics a moment when one

arm just placed an object while the other arm is executing a manipulation task or idling.

A rearrangement plan of the instance in Figure 4.1[Left], as a path in the interval state space, is presented in Figure B.1. The plan starts with the interval state s_1 representing the start arrangement. In s_1 , r_1 and r_2 choose to pick o_2 and o_1 respectively. The second state in the path is the moment when r_1 completes the placement of o_2 while r_2 is still executing the manipulation. When r_2 places o_1 at its goal pose, r_1 is attempting to move o_3 to the handoff pose, which yields to state s_3 in the path. After the handoff, r_2 places o_3 at its goal pose and the plan ends when both arms return to their rest poses.

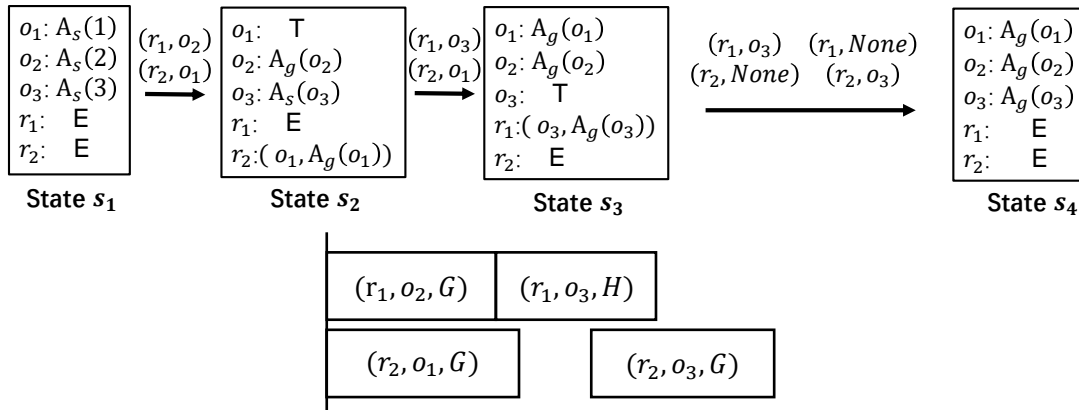


Figure B.1: [Top] A path on the interval state space for the example instance in Figure 4.1[Left]. [Bottom] The corresponding task schedule for the instance.

In either single arm rearrangement or dual-arm rearrangement with MC metric, object poses in arrangement states are determined, and the transition cost between states is the cost of specific manipulations. However, an interval state is more flexible and the transition cost between interval states is non-deterministic either. For example, in s_3 in Figure B.1, without mentioning the path from the start state, r_1 can be on the way to $\mathcal{A}_s(o_3)$ or waiting at the handoff pose (since $\mathcal{A}_g(o_3)$ is out of reach). Moreover, there is no non-trivial lower bound on the transition cost between interval states. For example, from state s_2 to state s_3 , the transition cost may be close to 0 if r_2 finishes the placement right after r_1 does. It may also be close to the cost of the pick-n-place if r_2 just starts to leave for $\mathcal{A}_s(o_1)$ when r_1 finishes the placement.

Given a path on the search tree and an interval state s , the current cost $g(s)$ on the path is defined as the current makespan. In the path presented in Figure B.1[Top], $g(s_2) = t_{pp}(\gamma_1, \mathcal{A}_s(o_2), \mathcal{A}_g(o_2))$, where γ_1 is the projection of the rest pose of r_1 's end-effector to the 2d space embedding \mathcal{W} . It is the pick-n-place cost of r_1 to manipulate o_2 . At this moment, r_1 completes the placement of o_2 . Similarly, $g(s_3) = t_{pp}(\gamma_2, \mathcal{A}_s(o_1), \mathcal{A}_g(o_1))$. At this moment, r_2 completes the placement of o_1 . Note that the buffer locations are treated as variables in this task scheduling phase. When a buffer is involved in a primitive action, e.g. moving an object from/to buffer, the travel distance of the arm is set as the diagonal distance of its reachable region. This setting further penalizes temporary object displacements and ensures the computed schedule is executable no matter where the buffers are allocated in the workspace. Based on the path from state s_1 to s_4 , we obtain a corresponding task schedule.

Similar to the arrangement space heuristic search, for each interval state s , the heuristic function $h(s)$ is defined based on the cost of picking, transferring, placing, and handing off that are needed to rearrange objects which are still away from the goal poses. While the general idea is the same as manipulation cost based heuristic (Algorithm 9), we make some modifications for interval states. The details are presented in Algo.Algorithm 16. In an interval state, the ongoing task can be arbitrarily close to completion. Therefore, besides the objects at the goal poses, we also ignore objects moving to the goal poses (Line 3), When the object needs a handoff to the goal pose (Line 8), the delivering arm bears the delivery cost (Line 9-10), and the receiving arm bears the receiving cost (Line 11-12).

Algorithm 16: Full Cost Search Heuristic

Input : s : current interval state
Output: h : heuristic value of s

- 1 $\text{cost}[r_1], \text{cost}[r_2], \text{sharedCost} \leftarrow 0, 0, 0$
- 2 **for** $o_i \in \mathcal{O}$ **do**
- 3 **if** o_i is at goal or moving to goal **then** continue;
- 4 $\text{armSet} \leftarrow \text{ReachableArms}(s, o_i, \{\mathcal{L}(o_i), G\})$
- 5 **if** armSet is $\{r_1, r_2\}$ **then** $\text{sharedCost} \leftarrow \text{sharedCost} + \text{transfer}(o_i, \mathcal{L}(o_i), G) + t_g + t_r$;
- 6 **else if** armSet is $\{r_1\}$ **then** $\text{cost}[r_1] \leftarrow \text{cost}[r_1] + \text{transfer}(o_i, \mathcal{L}(o_i), G) + t_g + t_r$;
- 7 **else if** armSet is $\{r_2\}$ **then** $\text{cost}[r_2] \leftarrow \text{cost}[r_2] + \text{transfer}(o_i, \mathcal{L}(o_i), G) + t_g + t_r$;
- 8 **else**
- 9 $\text{deliverArm} \leftarrow \text{ReachableArms}(s, o_i, \{\mathcal{L}(o_i)\})$
- 10 $\text{cost}[\text{deliverArm}] \leftarrow \text{cost}[\text{deliverArm}] + \text{transfer}(o_i, \mathcal{L}(o_i), H) + t_g + t_h$
- 11 $\text{receiveArm} \leftarrow \text{ReachableArms}(s, o_i, \{G\})$
- 12 $\text{cost}[\text{receiveArm}] \leftarrow \text{cost}[\text{receiveArm}] + \text{transfer}(o_i, H, G) + t_h + t_r$
- 13 **end**
- 14 **end**
- 15 **if** $\|\text{cost}[r_1] - \text{cost}[r_2]\| \leq \text{sharedCost}$ **then**
- 16 **return** $(\text{cost}[r_1] + \text{cost}[r_2] + \text{sharedCost}) / 2$;
- 17 **else return** $\max(\text{cost}[r_1], \text{cost}[r_2])$;

ACKNOWLEDGMENT OF PREVIOUS PUBLICATIONS

- P1 Kai Gao***, Zihe Ye*, Duo Zhang*, Baichuan Huang, and Jingjin Yu. "Toward Holistic Planning and Control Optimization for Dual-Arm Rearrangement." arXiv preprint arXiv:2404.06758 (2024).
- P2 Kai Gao***, Zhaxizhuoma*, Yan Ding, Shiqi Zhang, and Jingjin Yu. "ORLA*: Mobile Manipulator-Based Object Rearrangement with Lazy A*." arXiv preprint arXiv:2309.13707 (2023).
- P3 Kai Gao**, Justin Yu, Tanay Sandeep Punjabi, and Jingjin Yu. "Effectively rearranging heterogeneous objects on cluttered tabletops." In 2023 IEEE/RSJ International Conference on Intelligent Robots and Systems (IROS), pp. 2057-2064. IEEE, 2023.
- P4 Kai Gao**, Si Wei Feng, Baichuan Huang, and Jingjin Yu. "Minimizing running buffers for tabletop object rearrangement: Complexity, fast algorithms, and applications." The International Journal of Robotics Research 42, no. 10 (2023): 755-776.
- P5 Kai Gao**, and Jingjin Yu. "Toward efficient task planning for dual-arm tabletop object rearrangement." In 2022 IEEE/RSJ International Conference on Intelligent Robots and Systems (IROS), pp. 10425-10431. IEEE, 2022.
- P6 Kai Gao**, Darren Lau, Baichuan Huang, Kostas E. Bekris, and Jingjin Yu. "Fast high-quality tabletop rearrangement in bounded workspace." In 2022 International Conference on Robotics and Automation (ICRA), pp. 1961-1967. IEEE, 2022.
- P7 Kai Gao**, Si Wei Feng, and Jingjin Yu. "On running buffer minimization for tabletop rearrangement." In 17th Robotics: Science and Systems, RSS 2021.

REFERENCES

- [1] S. D. Han, N. M. Stiffler, A. Krontiris, K. E. Bekris, and J. Yu, “Complexity results and fast methods for optimal tabletop rearrangement with overhand grasps,” *The International Journal of Robotics Research*, vol. 37, no. 13-14, pp. 1775–1795, 2018.
- [2] A. Saxena, J. Driemeyer, and A. Y. Ng, “Robotic grasping of novel objects using vision,” *The International Journal of Robotics Research*, vol. 27, no. 2, pp. 157–173, 2008.
- [3] M. Gualtieri, A. ten Pas, K. Saenko, and R. Platt, “High precision grasp pose detection in dense clutter,” in *2016 IEEE/RSJ International Conference on Intelligent Robots and Systems (IROS)*, Daejeon, Korea (South), 2016, pp. 598–605.
- [4] C. Mitash, K. E. Bekris, and A. Boularias, “A self-supervised learning system for object detection using physics simulation and multi-view pose estimation,” in *2017 IEEE/RSJ International Conference on Intelligent Robots and Systems (IROS)*, IEEE, Vancouver, BC, Canada, 2017, pp. 545–551.
- [5] Y. Xiang, T. Schmidt, V. Narayanan, and D. Fox, “Posecnn: A convolutional neural network for 6d object pose estimation in cluttered scenes,” in *Proceedings of Robotics: Science and Systems*, Pittsburgh, Pennsylvania, Jun. 2018.
- [6] M. Stilman and J. J. Kuffner, “Navigation among movable obstacles: Real-time reasoning in complex environments,” *International Journal of Humanoid Robotics*, vol. 2, no. 04, pp. 479–503, 2005.
- [7] K. Treleaven, M. Pavone, and E. Frazzoli, “Asymptotically optimal algorithms for one-to-one pickup and delivery problems with applications to transportation systems,” *IEEE Transactions on Automatic Control*, vol. 58, no. 9, pp. 2261–2276, 2013.
- [8] G. Havur, G. Ozbilgin, E. Erdem, and V. Patoglu, “Geometric rearrangement of multiple movable objects on cluttered surfaces: A hybrid reasoning approach,” in *2014 IEEE International Conference on Robotics and Automation (ICRA)*, IEEE, Hong Kong, China, 2014, pp. 445–452.
- [9] A. Krontiris and K. E. Bekris, “Dealing with difficult instances of object rearrangement,” in *Robotics: Science and Systems*, vol. 1123, 2015.
- [10] J. E. King, M. Cognetti, and S. S. Srinivasa, “Rearrangement planning using object-centric and robot-centric action spaces,” in *2016 IEEE International Conference*

- on Robotics and Automation (ICRA)*, IEEE, Stockholm, Sweden, 2016, pp. 3940–3947.
- [11] J. Lee, Y. Cho, C. Nam, J. Park, and C. Kim, “Efficient obstacle rearrangement for object manipulation tasks in cluttered environments,” in *2019 International Conference on Robotics and Automation (ICRA)*, IEEE, Montreal, QC, Canada, 2019, pp. 183–189.
- [12] R. H. Taylor, M. T. Mason, and K. Y. Goldberg, “Sensor-based manipulation planning as a game with nature,” in *Proceedings of the 4th International Symposium on Robotics Research*, Univ. of California, Santa Clara, California, USA: MIT Press, 1988, pp. 421–429, ISBN: 0262022729.
- [13] K. Y. Goldberg, “Orienting polygonal parts without sensors,” *Algorithmica*, vol. 10, no. 2, pp. 201–225, 1993.
- [14] K. M. Lynch and M. T. Mason, “Dynamic nonprehensile manipulation: Controllability, planning, and experiments,” *The International Journal of Robotics Research*, vol. 18, no. 1, pp. 64–92, 1999.
- [15] M. Dogar and S. Srinivasa, “A framework for push-grasping in clutter,” Jun. 2011.
- [16] J. Bohg, A. Morales, T. Asfour, and D. Kragic, “Data-driven grasp synthesis—a survey,” *IEEE Transactions on Robotics*, vol. 30, no. 2, pp. 289–309, 2013.
- [17] N. C. Dafle *et al.*, “Extrinsic dexterity: In-hand manipulation with external forces,” in *2014 IEEE International Conference on Robotics and Automation (ICRA)*, IEEE, Hong Kong, China, 2014, pp. 1578–1585.
- [18] A. Boularias, J. Bagnell, and A. Stentz, “Learning to manipulate unknown objects in clutter by reinforcement,” 1, vol. 29, Feb. 2015.
- [19] N. Chavan-Dafle and A. Rodriguez, “Prehensile pushing: In-hand manipulation with push-primitives,” in *2015 IEEE/RSJ International Conference on Intelligent Robots and Systems (IROS)*, IEEE, Hamburg, Germany, 2015, pp. 6215–6222.
- [20] L. P. Kaelbling and T. Lozano-Pérez, “Hierarchical task and motion planning in the now,” in *2011 IEEE International Conference on Robotics and Automation*, 2011, pp. 1470–1477.
- [21] S. Levine, C. Finn, T. Darrell, and P. Abbeel, “End-to-end training of deep visuomotor policies,” *The Journal of Machine Learning Research*, vol. 17, no. 1, pp. 1334–1373, 2016.

- [22] J. Mahler *et al.*, “Dex-net 2.0: Deep learning to plan robust grasps with synthetic point clouds and analytic grasp metrics,” in *Proceedings of Robotics: Science and Systems*, Cambridge, Massachusetts, Jul. 2017.
- [23] A. Zeng *et al.*, “Robotic pick-and-place of novel objects in clutter with multi-affordance grasping and cross-domain image matching,” in *2018 IEEE international conference on robotics and automation (ICRA)*, IEEE, Brisbane, QLD, Australia, 2018, pp. 3750–3757.
- [24] A. M. Wells, N. T. Dantam, A. Shrivastava, and L. E. Kavraki, “Learning feasibility for task and motion planning in tabletop environments,” *IEEE robotics and automation letters*, vol. 4, no. 2, pp. 1255–1262, 2019.
- [25] J. E. Hopcroft, J. T. Schwartz, and M. Sharir, “On the complexity of motion planning for multiple independent objects; pspace-hardness of the ‘warehouseman’s problem’,” *The International Journal of Robotics Research*, vol. 3, no. 4, pp. 76–88, 1984.
- [26] G. Wilfong, “Motion planning in the presence of movable obstacles,” *Annals of Mathematics and Artificial Intelligence*, vol. 3, no. 1, pp. 131–150, 1991.
- [27] M. Stilman, J.-U. Schamburek, J. Kuffner, and T. Asfour, “Manipulation planning among movable obstacles,” in *Proceedings 2007 IEEE international conference on robotics and automation*, IEEE, Rome, Italy, 2007, pp. 3327–3332.
- [28] R. Wang, K. Gao, J. Yu, and K. Bekris, “Lazy rearrangement planning in confined spaces,” in *Proceedings of the International Conference on Automated Planning and Scheduling*, vol. 32, 2022, pp. 385–393.
- [29] C. H. Papadimitriou, “The euclidean travelling salesman problem is np-complete,” *Theoretical computer science*, vol. 4, no. 3, pp. 237–244, 1977.
- [30] R. M. Karp, “Reducibility among combinatorial problems,” in *Complexity of computer computations*, Springer, 1972, pp. 85–103.
- [31] S. Bereg and A. Dumitrescu, “The lifting model for reconfiguration,” *Discrete & Computational Geometry*, vol. 35, no. 4, pp. 653–669, 2006.
- [32] C. Nam, J. Lee, Y. Cho, J. Lee, D. H. Kim, and C. Kim, “Planning for target retrieval using a robotic manipulator in cluttered and occluded environments,” *arXiv preprint arXiv:1907.03956*, 2019.
- [33] D. Halperin, M. van Kreveld, G. Miglioli-Levy, and M. Sharir, “Space-aware reconfiguration,” *Discrete & Computational Geometry*, pp. 1–38, 2022.

- [34] O. Ben-Shahar and E. Rivlin, “Practical pushing planning for rearrangement tasks,” *IEEE Transactions on Robotics and Automation*, vol. 14, no. 4, pp. 549–565, 1998.
- [35] E. Huang, Z. Jia, and M. T. Mason, “Large-scale multi-object rearrangement,” in *2019 International Conference on Robotics and Automation (ICRA)*, IEEE, Montreal, QC, Canada, 2019, pp. 211–218.
- [36] L. Chang, J. R. Smith, and D. Fox, “Interactive singulation of objects from a pile,” in *2012 IEEE International Conference on Robotics and Automation*, IEEE, Saint Paul, MN, USA, 2012, pp. 3875–3882.
- [37] M. Laskey *et al.*, “Robot grasping in clutter: Using a hierarchy of supervisors for learning from demonstrations,” in *2016 IEEE International Conference on Automation Science and Engineering (CASE)*, IEEE, Fort Worth, TX, USA, 2016, pp. 827–834.
- [38] A. Eitel, N. Hauff, and W. Burgard, “Learning to singulate objects using a push proposal network,” in *Robotics Research*, N. M. Amato, G. Hager, S. Thomas, and M. Torres-Torriti, Eds., Cham: Springer International Publishing, 2020, pp. 405–419, ISBN: 978-3-030-28619-4.
- [39] H. Song *et al.*, “Multi-object rearrangement with monte carlo tree search: A case study on planar nonprehensile sorting,” pp. 9433–9440, 2020.
- [40] Z. Pan and K. Hauser, “Decision making in joint push-grasp action space for large-scale object sorting,” in *2021 IEEE International Conference on Robotics and Automation (ICRA)*, Xi’an, China, 2021, pp. 6199–6205.
- [41] A. Zeng, S. Song, S. Welker, J. Lee, A. Rodriguez, and T. Funkhouser, “Learning synergies between pushing and grasping with self-supervised deep reinforcement learning,” in *2018 IEEE/RSJ International Conference on Intelligent Robots and Systems (IROS)*, IEEE, Madrid, Spain, 2018, pp. 4238–4245.
- [42] B. Huang, S. D. Han, A. Boularias, and J. Yu, “Dipn: Deep interaction prediction network with application to clutter removal,” in *2021 IEEE International Conference on Robotics and Automation (ICRA)*, Xi’an, China, 2021, pp. 4694–4701.
- [43] B. Huang, S. D. Han, J. Yu, and A. Boularias, “Visual foresight trees for object retrieval from clutter with nonprehensile rearrangement,” *IEEE Robotics and Automation Letters*, vol. 7, no. 1, pp. 231–238, 2021.
- [44] E. R. Vieira, D. Nakhimovich, K. Gao, R. Wang, J. Yu, and K. E. Bekris, “Persistent homology for effective non-prehensile manipulation,” *arXiv preprint arXiv:2202.02937*, 2022.

- [45] S. J. Buckley, *Fast motion planning for multiple moving robots*. IBM Thomas J. Watson Research Division, 1988.
- [46] J. van Den Berg, J. Snoeyink, M. C. Lin, and D. Manocha, “Centralized path planning for multiple robots: Optimal decoupling into sequential plans.,” in *Robotics: Science and systems*, vol. 2, 2009, pp. 2–3.
- [47] A. Krontiris and K. E. Bekris, “Efficiently solving general rearrangement tasks: A fast extension primitive for an incremental sampling-based planner,” in *2016 IEEE International Conference on Robotics and Automation (ICRA)*, IEEE, 2016, pp. 3924–3931.
- [48] F. Wang and K. Hauser, “Robot packing with known items and nondeterministic arrival order,” *IEEE Transactions on Automation Science and Engineering*, 2020.
- [49] K. Gao and J. Yu, “Toward efficient task planning for dual-arm tabletop object rearrangement,” in *2022 IEEE/RSJ International Conference on Intelligent Robots and Systems (IROS)*, 2022, pp. 10 425–10 431.
- [50] J. Díaz, J. Petit, and M. Serna, “A survey of graph layout problems,” *ACM Computing Surveys (CSUR)*, vol. 34, no. 3, pp. 313–356, 2002.
- [51] H. R. Lewis, “Michael r. ngarey and david s. johnson. computers and intractability. a guide to the theory of np-completeness. w. h. freeman and company, san francisco 1979, x 338 pp.,” *The Journal of Symbolic Logic*, vol. 48, no. 2, pp. 498–500, 1983.
- [52] C. H. Papadimitriou, “The np-completeness of the bandwidth minimization problem,” *Computing*, vol. 16, no. 3, pp. 263–270, 1976.
- [53] M. R. Garey, D. S. Johnson, and L. Stockmeyer, “Some simplified np-complete problems,” in *Proceedings of the Sixth Annual ACM Symposium on Theory of Computing*, ser. STOC ’74, Seattle, Washington, USA: Association for Computing Machinery, 1974, pp. 47–63, ISBN: 9781450374231.
- [54] F. Gavril, “Some np-complete problems on graphs,” Computer Science Department, Technion, Tech. Rep., 2011.
- [55] H. L. Bodlaender, J. R. Gilbert, H. Hafsteinsson, and T. Kloks, “Approximating treewidth, pathwidth, frontsize, and shortest elimination tree,” *Journal of Algorithms*, vol. 18, no. 2, pp. 238–255, 1995.
- [56] T.-h. Shin, H. Oh, and S. Ha, “Minimizing buffer requirements for throughput constrained parallel execution of synchronous dataflow graph,” in *16th Asia and South*

Pacific Design Automation Conference (ASP-DAC 2011), Yokohama, Japan, 2011, pp. 165–170.

- [57] R. J. Lipton and R. E. Tarjan, “A separator theorem for planar graphs,” *SIAM Journal on Applied Mathematics*, vol. 36, no. 2, pp. 177–189, 1979.
- [58] J. R. Gilbert, J. P. Hutchinson, and R. E. Tarjan, “A separator theorem for graphs of bounded genus,” *Journal of Algorithms*, vol. 5, no. 3, pp. 391–407, 1984.
- [59] N. Alon, P. Seymour, and R. Thomas, “A separator theorem for graphs with an excluded minor and its applications,” in *Proceedings of the Twenty-Second Annual ACM Symposium on Theory of Computing*, ser. STOC '90, Baltimore, Maryland, USA: Association for Computing Machinery, 1990, pp. 293–299, ISBN: 0897913612.
- [60] U. Elsner, *Graph partitioning-a survey*. Techn. Univ., 1997.
- [61] R. Tarjan, “Depth-first search and linear graph algorithms,” *SIAM journal on computing*, vol. 1, no. 2, pp. 146–160, 1972.
- [62] Y. Shiloach, “A minimum linear arrangement algorithm for undirected trees,” *SIAM Journal on Computing*, vol. 8, no. 1, pp. 15–32, 1979.
- [63] D. Adolphson and T. C. Hu, “Optimal linear ordering,” *SIAM Journal on Applied Mathematics*, vol. 25, no. 3, pp. 403–423, 1973.
- [64] L. M. Kirousis and C. H. Papadimitriou, “Searching and pebbling,” *Theoretical Computer Science*, vol. 47, pp. 205–218, 1986.
- [65] N. G. Kinnersley, “The vertex separation number of a graph equals its path-width,” *Information Processing Letters*, vol. 42, no. 6, pp. 345–350, 1992.
- [66] M. R. Fellows and M. A. Langston, “On search decision and the efficiency of polynomial-time algorithms,” in *Proceedings of the Twenty-First Annual ACM Symposium on Theory of Computing*, ser. STOC '89, Seattle, Washington, USA: Association for Computing Machinery, 1989, pp. 501–512, ISBN: 0897913078.
- [67] B. Monien and I. H. Sudborough, “Min cut is np-complete for edge weighted trees,” *Theoretical Computer Science*, vol. 58, no. 1-3, pp. 209–229, 1988.
- [68] F. István, “On straight-line representation of planar graphs,” *Acta scientiarum mathematicarum*, vol. 11, no. 229-233, p. 2, 1948.
- [69] R. Wang, K. Gao, D. Nakhimovich, J. Yu, and K. E. Bekris, “Uniform object rearrangement: From complete monotone primitives to efficient non-monotone in-

- formed search,” in *IEEE International Conference on Robotics and Automation*, 2021.
- [70] N. Koenig and A. Howard, “Design and use paradigms for gazebo, an open-source multi-robot simulator,” in *2004 IEEE/RSJ International Conference on Intelligent Robots and Systems (IROS)(IEEE Cat. No. 04CH37566)*, IEEE, vol. 3, Sendai, Japan, 2004, pp. 2149–2154.
- [71] L. Gurobi Optimization, *Gurobi optimizer reference manual*, 2021.
- [72] Q. Bonnard *et al.*, *Chilitags 2: Robust fiducial markers for augmented reality and robotics*. 2013.
- [73] A. Cosgun, T. Hermans, V. Emeli, and M. Stilman, “Push planning for object placement on cluttered table surfaces,” in *2011 IEEE/RSJ international conference on intelligent robots and systems*, IEEE, 2011, pp. 4627–4632.
- [74] K. Gao, S. W. Feng, B. Huang, and J. Yu, “Minimizing running buffers for tabletop object rearrangement: Complexity, fast algorithms, and applications,” *The International Journal of Robotics Research*, vol. 42, no. 10, pp. 755–776, 2023. eprint: <https://doi.org/10.1177/02783649231178565>.
- [75] R. Wang, Y. Miao, and K. E. Bekris, “Efficient and high-quality prehensile rearrangement in cluttered and confined spaces,” *arXiv preprint arXiv:2110.02814*, 2021.
- [76] M. Stilman, K. Nishiwaki, S. Kagami, and J. J. Kuffner, “Planning and executing navigation among movable obstacles,” *Advanced Robotics*, vol. 21, no. 14, pp. 1617–1634, 2007.
- [77] M. Stilman and J. Kuffner, “Planning among movable obstacles with artificial constraints,” *The International Journal of Robotics Research*, vol. 27, no. 11-12, pp. 1295–1307, 2008.
- [78] H. Zhang, Y. Lu, C. Yu, D. Hsu, X. Lan, and N. Zheng, “INVIGORATE: Interactive Visual Grounding and Grasping in Clutter,” in *Proceedings of Robotics: Science and Systems*, Virtual, Jul. 2021.
- [79] J. E. King, V. Ranganeni, and S. S. Srinivasa, “Unobservable monte carlo planning for nonprehensile rearrangement tasks,” in *2017 IEEE International Conference on Robotics and Automation (ICRA)*, IEEE, 2017, pp. 4681–4688.
- [80] B. Huang, S. D. Han, A. Boularias, and J. Yu, “Dipn: Deep interaction prediction network with application to clutter removal,” in *IEEE International Conference on Robotics and Automation*, 2021.

- [81] Y. Labbé *et al.*, “Monte-carlo tree search for efficient visually guided rearrangement planning,” *IEEE Robotics and Automation Letters*, vol. 5, no. 2, pp. 3715–3722, 2020.
- [82] A. Morgan, B. Wen, J. Liang, A. Boularias, A. Dollar, and K. Bekris, “Vision-driven compliant manipulation for reliable, high-precision assembly tasks,” *Proceedings of Robotics: Science and Systems (R: SS)*, 2021.
- [83] B. Wen, W. Lian, K. Bekris, and S. Schaal, “Catgrasp: Learning category-level task-relevant grasping in clutter from simulation,” *arXiv preprint arXiv:2109.09163*, 2021.
- [84] K. Okada, A. Haneda, H. Nakai, M. Inaba, and H. Inoue, “Environment manipulation planner for humanoid robots using task graph that generates action sequence,” in *2004 IEEE/RSJ International Conference on Intelligent Robots and Systems (IROS)(IEEE Cat. No. 04CH37566)*, IEEE, vol. 2, 2004, pp. 1174–1179.
- [85] M. Levihn, J. Scholz, and M. Stilman, “Hierarchical decision theoretic planning for navigation among movable obstacles,” in *Algorithmic Foundations of Robotics X*, Springer, 2013, pp. 19–35.
- [86] S. H. Cheong, B. Y. Cho, J. Lee, C. Kim, and C. Nam, “Where to relocate?: Object rearrangement inside cluttered and confined environments for robotic manipulation,” in *2020 IEEE International Conference on Robotics and Automation (ICRA)*, IEEE, 2020, pp. 7791–7797.
- [87] R. Bohlin and L. E. Kavraki, “Path planning using lazy prm,” in *Proceedings 2000 ICRA. Millennium Conference. IEEE International Conference on Robotics and Automation. Symposia Proceedings (Cat. No. 00CH37065)*, IEEE, vol. 1, 2000, pp. 521–528.
- [88] J. Denny, K. Shi, and N. M. Amato, “Lazy toggle prm: A single-query approach to motion planning,” in *2013 IEEE International Conference on Robotics and Automation*, IEEE, 2013, pp. 2407–2414.
- [89] K. Hauser, “Lazy collision checking in asymptotically-optimal motion planning,” in *2015 IEEE international conference on robotics and automation (ICRA)*, IEEE, 2015, pp. 2951–2957.
- [90] N. Chernov, Y. Stoyan, and T. Romanova, “Mathematical model and efficient algorithms for object packing problem,” *Computational Geometry*, vol. 43, no. 5, pp. 535–553, 2010.
- [91] R. Shome, K. Solovey, J. Yu, K. Bekris, and D. Halperin, “Fast, high-quality dual-arm rearrangement in synchronous, monotone tabletop setups,” in *Algorithmic Foun-*

dations of Robotics XIII: Proceedings of the 13th Workshop on the Algorithmic Foundations of Robotics, Springer, 2020, pp. 778–795.

- [92] K. Gao, D. Lau, B. Huang, K. E. Bekris, and J. Yu, “Fast high-quality tabletop rearrangement in bounded workspace,” in *2022 International Conference on Robotics and Automation (ICRA)*, IEEE, 2022, pp. 1961–1967.
- [93] J. Yu, “Rearrangement on lattices with pic-n-swaps: Optimality structures and efficient algorithms,” in *Robotics: Sciences and Systems*, 2021.
- [94] R. Shome and K. E. Bekris, “Synchronized multi-arm rearrangement guided by mode graphs with capacity constraints,” *arXiv preprint arXiv:2005.09127*, 2020.
- [95] R. Shome, K. Solovey, J. Yu, K. Bekris, and D. Halperin, “Fast, high-quality two-arm rearrangement in synchronous, monotone tabletop setups,” *IEEE Transactions on Automation Science and Engineering*, 2021.
- [96] B. Sundaralingam *et al.*, “Curobo: Parallelized collision-free minimum-jerk robot motion generation,” *arXiv preprint arXiv:2310.17274*, 2023.
- [97] K. Gao, D. Lau, B. Huang, K. E. Bekris, and J. Yu, “Fast high-quality tabletop rearrangement in bounded workspace,” *arXiv preprint arXiv:2110.12325*, 2021.
- [98] B. Huang, T. Guo, A. Boularias, and J. Yu, “Self-supervised monte carlo tree search learning for object retrieval in clutter,” *arXiv preprint arXiv:2202.01426*, 2022.
- [99] J. Ahn, C. Kim, and C. Nam, “Coordination of two robotic manipulators for object retrieval in clutter,” *arXiv preprint arXiv:2109.15220*, 2021.
- [100] S. Li, C. Hu, and F. Tian, “Enhancing optimal feeder assignment of the multi-head surface mounting machine using genetic algorithms,” *Applied Soft Computing*, vol. 8, no. 1, pp. 522–529, 2008.
- [101] M. Moghaddam and S. Y. Nof, “Parallelism of pick-and-place operations by multi-gripper robotic arms,” *Robotics and Computer-Integrated Manufacturing*, vol. 42, pp. 135–146, 2016.
- [102] H. Pham and Q.-C. Pham, “A new approach to time-optimal path parameterization based on reachability analysis,” *IEEE Transactions on Robotics*, vol. 34, no. 3, pp. 645–659, 2018.
- [103] S. Garrido-Jurado, R. Muñoz-Salinas, F. J. Madrid-Cuevas, and M. J. Marín-Jiménez, “Automatic generation and detection of highly reliable fiducial markers under occlusion,” *Pattern Recognition*, vol. 47, no. 6, pp. 2280–2292, 2014.

- [104] A. P. Lindvig, *ur_rtde*, https://gitlab.com/sdurobotics/ur_rtde, 2018.
- [105] A. Zeng *et al.*, “Transporter networks: Rearranging the visual world for robotic manipulation,” in *Conference on Robot Learning*, PMLR, 2021, pp. 726–747.
- [106] K. Gao, S. W. Feng, B. Huang, and J. Yu, “Minimizing running buffers for tabletop object rearrangement: Complexity, fast algorithms, and applications,” *The International Journal of Robotics Research*, p. 02 783 649 231 178 565, 2023.
- [107] X. Zhang, Y. Zhu, Y. Ding, Y. Zhu, P. Stone, and S. Zhang, “Visually grounded task and motion planning for mobile manipulation,” in *2022 International Conference on Robotics and Automation (ICRA)*, IEEE, 2022, pp. 1925–1931.
- [108] Y. Ding, X. Zhang, C. Paxton, and S. Zhang, “Task and motion planning with large language models for object rearrangement,” *arXiv preprint arXiv:2303.06247*, 2023.
- [109] A. Xu, K. Gao, S. W. Feng, and J. Yu, *Optimal and stable multi-layer object rearrangement on a tabletop*, 2023. arXiv: 2306.14251 [cs .RO].
- [110] W. Yuan, K. Hang, D. Kragic, M. Y. Wang, and J. A. Stork, “End-to-end nonprehensile rearrangement with deep reinforcement learning and simulation-to-reality transfer,” *Robotics and Autonomous Systems*, vol. 119, pp. 119–134, 2019.
- [111] H. Song *et al.*, “Multi-object rearrangement with monte carlo tree search: A case study on planar nonprehensile sorting,” in *2020 IEEE/RSJ International Conference on Intelligent Robots and Systems (IROS)*, IEEE, 2020, pp. 9433–9440.
- [112] B. Tang and G. S. Sukhatme, “Selective object rearrangement in clutter,” in *Conference on Robot Learning*, PMLR, 2023, pp. 1001–1010.
- [113] K. Gao, J. Yu, T. S. Punjabi, and J. Yu, *Effectively rearranging heterogeneous objects on cluttered tabletops*, 2023. arXiv: 2306.14240 [cs .RO].
- [114] W. Wan, K. Harada, and K. Nagata, “Assembly sequence planning for motion planning,” *Assembly Automation*, vol. 38, no. 2, pp. 195–206, 2018.
- [115] M. McEvoy, E. Komendera, and N. Correll, “Assembly path planning for stable robotic construction,” in *2014 IEEE International Conference on Technologies for Practical Robot Applications (TePRA)*, IEEE, 2014, pp. 1–6.
- [116] C. R. Garrett, Y. Huang, T. Lozano-Pérez, and C. T. Mueller, “Scalable and probabilistically complete planning for robotic spatial extrusion,” *arXiv preprint arXiv:2002.02360*, 2020.

- [117] M. Noseworthy *et al.*, “Active learning of abstract plan feasibility,” *arXiv preprint arXiv:2107.00683*, 2021.
- [118] Y. Lee, W. Thomason, Z. Kingston, and L. E. Kavraki, “Object reconfiguration with simulation-derived feasible actions,” *arXiv preprint arXiv:2302.14161*, 2023.
- [119] H. Zhang *et al.*, “Resnest: Split-attention networks,” in *Proceedings of the IEEE/CVF conference on computer vision and pattern recognition*, 2022, pp. 2736–2746.
- [120] F. Fodor, “The densest packing of 19 congruent circles in a circle,” *Geometriae Dedicata*, vol. 74, no. 2, pp. 139–145, 1999.